Large-eddy simulation of wind farms in clear and cloud-topped boundary layers

by

P. A. van Dorp

to obtain the degree of Master of Science
at the Delft University of Technology,
to be defended publicly on Thursday July 7, 2016 at 10:00 AM.

Student number: 4142195
Project duration: August 20, 2015 – June 2, 2016

Thesis committee:

Dr. S. R. de Roode,	TU Delft (Geoscience and Remote Sensing)
Dr. ir. R. A. Verzijlbergh,	TU Delft (Engineering Systems and Services)
Prof. dr. H. J. J. Jonker,	TU Delft (Geoscience and Remote Sensing)
Dr. ir. M. J. B. M. Pourquie,	TU Delft (Process and Energy)

TU Delft

Preface and acknowledgements

At the end of my first year of the Master's Applied Physics at TU Delft, a decision was required on the topic of my thesis project. Based on my interest in fluid dynamics and renewable energy, along with the increasing significance of wind energy, a project in this field was the obvious choice. However, a large part of the wind energy research is, necessarily, conducted from an engineering point of view, where, after four years of applied physics in Delft, I came to prefer a more physical perspective. Fortunately, around that time I was introduced to the atmospheric sciences by Stephan de Roode, as part of a lecture series on environmental physics. The interesting combination of fluid dynamics, transport phenomena and thermodynamics made me curious about the research of his group. Once I heard Stephan was looking for a student to work on wind energy in relation to the atmosphere, I had found my subject of choice. Looking back, I am certain that I made the right decision. More importantly, I have found the research field in which I gladly continue working after finishing my Master's, and for this I am very grateful to Stephan. Furthermore, I like to thank Stephan for his enthusiasm, the interesting discussions, his elaborate feedback on my work and this report, the coffee breaks, and, of course, his anecdotes on cycling.

From Stephan's cycling stories I learned that the passion for cycling is widely spread in the field of atmospheric research. A passion that is actually also shared by my second supervisor, Remco Verzijlbergh. Equally enthusiastic about the research as Stephan, his input on the relevance of this project to wind energy and commercial applications was very valuable. Further, the link with the company he had just started together with Harm Jonker delivered an useful perspective on the development of our model from a practical point of view.

At the start of the project, I was rather hesitant about programming the wind turbine model in a computer language I was entirely unfamiliar with. Motivated by Stephan, who ensured me that programming basically consists of writing 'if' and 'do' statements, I gradually learned more about the code and, in the end, development of the model turned out to be one of my favorite parts of the project.

Building the wind turbine model would not have been possible without the help of Erwin de Beus. The use of the local computing cluster, managed by Erwin, was crucial to quickly perform numerous test runs. His help with everything related to computers, from compiling the source code to making animations, saved me a lot of time and effort. I am also particularly thankful to him for introducing me to the beauty of UNIX-based operating systems.

Next, I like to acknowledge Pier Siebesma for his ideas with regard to the boundary conditions of the model. Although initially unrelated to the wind turbine model, his suggestion of prescribing the boundaries from a different simulation greatly increased the applicability of the model and the quality of the results.

Finally, I like to thank my fellow students with whom I shared the student's office over the last year. Despite the office reaching tropical temperatures on sunny afternoons, the nice discussions and the view onto the Mekelpark definitely made it a pleasant work environment.

To summarize, it was a great year with a lot of nice experiences. From beating the PhD students in the departmental poster contest, to presenting my work at the BBOS symposium, and from a visit to the KNMI measurement site at Cabauw, to using a proper supercomputer. Furthermore, working on this project gave me the opportunity to meet a range of people from within the research field, who, together with Stephan, eventually convinced me to continue in the atmospheric sciences and wind energy in the future.

P. A. van Dorp
Delft, June 2016

Abstract

A wind turbine parameterization was implemented in the Dutch Atmospheric Large-Eddy Simulation (DALES) model, with the aim of developing a large-eddy simulation-based wind power forecast model. The wind turbine parameterization is based on the non-uniform actuator disk model and formulated in a general way to incorporate dynamic yaw control and allow arbitrary positioning of a large number of wind turbines. The modeling framework was validated against the respective power curves of two types of wind turbines, LiDAR observations of the wake velocity deficit and wind farm production data. Further, the model was used to study the evolution of wind turbine wakes during the diurnal cycle of a stratocumulus-topped boundary layer. At night, convective turbulence generated in the cloud layer leads to enhanced mixing of momentum into the wake, hereby significantly reducing its extent. Consequently, a considerably higher wind farm efficiency was found during the night, as compared to daytime. In case of the same surface buoyancy flux, but without a cloud deck, this effect was not observed. Finally, a different example of the interaction between wind turbines and clouds was considered: the formation of clouds in the wake of wind turbines as observed at the Horns Rev wind farm on February 12, 2008. Based on sparse observational data and a careful consideration of atmospheric thermodynamics and boundary-layer dynamics, we reconstructed the most probable atmospheric state that yields cloud formation only in the presence of wind turbines. A range of experiments was set up to explicitly simulate the formation of wake clouds with our model. A considerable deviation from the reconstructed temperature and humidity profiles was, however, found to be necessary to observe wind turbine-induced cloud formation in the simulations.

Contents

List of symbols and abbreviations

STBL	Stratocumulus-topped boundary layer
CFD	Computational fluid dynamics
NWP	Numerical weather prediction
LES	Large-eddy simulation
DALES	Dutch Atmospheric Large-Eddy Simulation
GPU	Graphic processing unit
UADM	Uniform actuator disk model
NUADM	Non-uniform actuator disk model
ABL	Atmospheric boundary layer
SBL	Stable boundary layer
NBL	Neutral boundary layer
CBL	Convective boundary layer
TKE	Turbulence kinetic energy in resolved scales
SFS TKE	Sub-filter scale turbulence kinetic energy
MKE	Mean kinetic energy
LWP	Cloud liquid water path
SST	Sea surface temperature
x_i	Rotor coordinate frame, $i = 1, 2, 3$ and $(x_1, x_2, x_3) \equiv (x, y, z) \equiv \mathbf{x}$
r	Distance from origin in y, z-plane
θ	Polar angle with respect to y-axis in y, z-plane
x_i^*	LES coordinate frame, $i = 1, 2, 3$ and $(x_1^*, x_2^*, x_3^*) \equiv (x^*, y^*, z^*) \equiv \mathbf{x}^*$
Δx_i^*	LES grid spacing
$x_i^{*\mathrm{hub}}$	Coordinates of wind turbine hub in LES coordinate frame
Q_{ij}	Rotation matrix for rotation around the z^*-axis
Δt	LES time step
u_i	Wind velocity in rotor frame, $i = 1, 2, 3$ and $(u_1, u_2, u_3) \equiv (u, v, w) \equiv \mathbf{u}$
u_i^*	Wind velocity in LES frame, $i = 1, 2, 3$ and $(u_1^*, u_2^*, u_3^*) \equiv (u^*, v^*, w^*) \equiv \mathbf{u}^*$
ϕ	Wind angle with respect to x^*-axis
U	Horizontal wind speed
U_∞	Undisturbed/free-stream horizontal wind speed
U^{geo}	Geostrophic wind speed
VD	Wind speed deficit in the wake of the wind turbine
R	Rotor radius
D	Rotor diameter
A	Rotor area
Ω	Rotational speed of wind turbine rotor
P	Wind turbine power
P_1	Power of upwind wind turbine in wind farm
P_n	Power of wind turbine n in wind farm
η	Wind farm efficiency
η^{geo}	Geostrophic wind farm efficiency
$\mathcal{F}$	Force per unit mass in LES coordinate frame
f	Force per unit mass and per unit area in rotor coordinate frame
ρ	Density of air
c	Chord length of air foil at radius r
C_L	Local lift coefficient of air foil

C_D	Local drag coefficient of air foil
ψ	Yaw angle of wind turbine with respect to x^*-axis
γ	Angle of relative wind on blade
α	Angle of attack
$\beta_{p,0}$	Pitch angle of the blade
β_p	Blade pitch angle at radius r
β_T	Blade twist angle at radius r
$\mathcal{R}$	Rotor geometrical footprint
$\mathcal{R}^N$	Normalized rotor geometrical footprint
G	Gaussian convolution filter
ϵ	Filter width of Gaussian convolution filter

1 Introduction

1.1. The variability of the wind resource

Denmark can be considered as a leading country in the transition towards a society primarily powered by electricity from renewable sources. The total installed capacity of renewable sources, primarily wind turbines, is rapidly closing in on the total capacity of conventional power stations. Over 2014, the wind power share in the total electricity consumption was almost 40 %, as compared to 22 % in 2009 (Energinet.dk, 2014). The annual mean wind power share does however not tell the whole story. In January 2014, on average 62 % of the total Danish electricity consumption was covered by wind power, against only 23 % in July of that same year. On a hourly basis, the wind power share peaked at 132 % on the early morning of January 19, in contrast to no wind power production at the end of the afternoon on September 29.

This is just one example of the inherent fluctuating nature of the availability of wind power. Although seasonal variations are all but insignificant, on hourly time scales they can make the difference between a wind energy surplus and no wind power at all. These variations show strong geographical correlations and pose significant operational challenges to power system operators (Xie et al., 2014). To guarantee the supply of electricity, and maintain a steady grid voltage and frequency, accurate predictions of the available wind power on these relatively small time scales are required. These predictions are crucial in order to maintain a balance between generation and demand, for example by firing up fossil power plants, or storage of electricity in hydropower systems, batteries (Dunn et al., 2011) and even electric vehicles (Kempton and Tomić, 2005). Before we can go into the details of making a wind power forecast, we need to identify the key parameters that determine the power output of a wind farm.

1.2. Basics of wind power

For a single wind turbine, the power, P, that can be extracted from the wind is proportional to the volumetric flow rate and the specific kinetic energy in the wind:

$$P \propto AU_\infty \times \frac{1}{2}\rho U_\infty^2, \tag{1.1}$$

where A is the area of the wind turbine rotor, i.e. $A = \pi D^2/4$ with D the diameter of the rotor blades. Further, U_∞ is the free-stream wind speed and ρ is the density of air. The constant of proportionality is typically referred to as the power coefficient, C_P , and we can write

$$P = \frac{1}{2}\rho C_P A U_\infty^3. \tag{1.2}$$

This simple relation shows that any variations in the wind speed lead to substantial power variations by the dependence of power on the wind speed cubed. Accurate predication of the

wind speed around the hub height of the wind turbine ($\sim 100\,\mathrm{m}$) is hence the most important characteristic of a wind power forecast model.

Where it is already quite a challenge to accurately predict the wind speed in the atmosphere on a local scale, prediction of the wind speed at a given wind turbine inside a wind farm is even more complex. Before, we have seen that wind turbines are driven by the extraction of kinetic energy from the incoming wind. As a consequence, the wind speed in the wake of the turbine is significantly reduced with respect to the free-stream wind speed. A wake that intersects with the swept rotor area of a downwind wind turbine reduces the effective wind speed and consequently the power production (González-Longatt et al., 2012).

The extent to which the power production of a (partly) shadowed wind turbine is reduced depends on the amount of overlap between the wake and the swept area and on the velocity deficit in the wake, i.e. the difference between the reduced wind speed in the wake and the free-stream wind speed. The first contribution is mainly related to the wind direction with respect to the layout of the wind farm. To account for this effect, prediction of the prevailing wind direction around the wind farm is required.

Representation of the second contribution, the velocity deficit in the wake, is the most complex and has been the topic of many observational and modeling studies over the last decades (for an overview see e.g. Crespo et al., 1999, Sanderse et al., 2011, Vermeer et al., 2003). The wind speed in the wake gradually recovers by entrainment of air with a higher momentum from outside the wake. This process is dominated by turbulent transport of momentum into the wake, and hence the rate of wake recovery is directly dependent on the amount of turbulence in the atmosphere. Numerous observational (Barthelmie et al., 2013, Hansen et al., 2012, Iungo and Porté-Agel, 2014, Machefaux et al., 2015, Mirocha et al., 2015) and modeling (Abkar and Porté-Agel, 2015, Abkar et al., 2015, Churchfield et al., 2012a, Machefaux et al., 2015) studies have shown that atmospheric turbulence has indeed a profound effect on the evolution of the wake and consequently on wind farm performance.

To summarize, a wind power forecast requires prediction of the free-stream wind speed and direction, and additionally of the wake reduced wind speed inside the wind farm, i.e. of the rate of wake recovery. Two approaches can be distinguished in trying to build a (short-term) forecast model for the power of a wind farm. Either the power production is predicted directly by statistical models, or a wind speed prediction from a numerical weather prediction (NWP) model is converted to a power prediction by use of the manufacturer's power curve (Zhu and Genton, 2012). As the primary focus of this report is on the second approach, we will not go into details about statistical wind power forecasting. For more details on current wind power forecast models we refer to Costa et al. (2008) and Giebel et al. (2011).

1.3. Why large-eddy simulation?

Although wind speed, wind direction and rate of wake recovery may seem rather unrelated at first glance, on the local scale all three are governed by the turbulence structure of the lowest part of the atmosphere, the atmospheric boundary layer (ABL). In the absence of turbulence, a balance between the large-scale pressure gradient and the Coriolis force at the top of the atmosphere determines the so-called geostrophic wind. Within the ABL, friction at the surface and vertical transport of momentum by turbulence dictates the shape of the wind velocity profile with respect to this geostrophic wind. Accordingly, a precise description of atmospheric turbulence is not only needed for prediction of the rate of wake recovery but also for the wind velocity itself.

Besides observations and measurements, computational fluid dynamics (CFD) is an essential tool in the study of the ABL. The relevant turbulent length scales, however, span an enormous range. From small vortices around the wind turbine blades to eddies with length scales of the order of the ABL height. Consequently, direct numerical simulation (DNS) of the interaction between the atmospheric flow and wind turbines is not an option. A possible solution would be to follow the Reynolds-averaged Navier-Stokes (RANS) approach and only explicitly compute the mean flow, while relying on a parameterization of turbulence to account for the effects of wind velocity fluctuations. As this parameterization is highly dependent on

the characteristics of a particular flow, RANS is not very well suited for general application (Lu and Porté-Agel, 2011). The large-eddy simulation (LES) approach was developed to provide a middle ground between the extremes of explicitly calculating (DNS) and parameterizing (RANS) the entire turbulence spectrum.

Over the last decades LES proved to be an essential tool for high-resolution numerical simulations of the ABL. The main advantage of the LES approach is the ability to perform simulations at high Reynolds numbers, while still explicitly resolving the part of the turbulence spectrum that contains the most turbulence kinetic energy (Moeng and Sullivan, 2002). Since the emergence of the LES technique in the late 1960s, a vast amount of different cases have been studied, covering increasingly large domains on higher and higher resolutions. Nowadays, with the emergence of graphic processing unit-based LES codes, domains up to $400\,\mathrm{km} \times 400\,\mathrm{km}$ have already been simulated at a resolution of 100 m (Schalkwijk et al., 2014).

The growing availability of computational power has also made LES suitable for the study of wind turbine flow dynamics (Mehta et al., 2014). The required resolution of 10 to 20 m (Wu and Porté-Agel, 2011) can nowadays easily be achieved on wind farm-sized domains. Jimenez et al. (2007), Calaf et al. (2010) and Wu and Porté-Agel (2011) were among the first to report on the implementation of a wind turbine model in a LES framework. Since then, LES of wind turbines has been successfully validated against wind tunnel studies (Wu and Porté-Agel, 2013), measured wake velocity deficits of utility-scale wind turbines (Aitken et al., 2014b, Mirocha et al., 2014) and wind farm power production data (Churchfield et al., 2012b, Creech et al., 2015, Nilsson et al., 2015, Wu and Porté-Agel, 2015).

LES of wind turbines has also been used to study the previously mentioned impact of atmospheric turbulence on wind turbine wake dynamics (Abkar and Porté-Agel, 2015, Churchfield et al., 2012a, Machefaux et al., 2015, Mirocha et al., 2015, Wu and Porté-Agel, 2012) and wind farm performance (Abkar et al., 2015, Allaerts and Meyers, 2015).

Apart from considering the effect of atmospheric turbulence on wind turbines and wind farms, LES-wind turbine frameworks can also be used to study the effect of large wind farms on the ABL. Several studies of this type showed that wind farms can significantly alter the vertical structure of the ABL and the fluxes at the surface (Lu and Porté-Agel, 2011, 2015, Porté-Agel et al., 2014).

1.4. Objectives and outline

In this work, we like to extend on the previously mentioned LES studies of wind turbine-ABL interaction, with the aim of developing a wind power forecast model. In a LES-based forecast model, the wind power is calculated from explicitly modeling the turbulent flow through the wind farm. Besides forecasting, such a physical model provides a wide range of additional applications, including resource assessment in complex terrain, detailed wind farm layout studies and analysis of aerodynamic loads. Although this report is mainly focused on the development of a forecast model, the last chapter will extend on this wide range of additional applications.

We will start with a discussion of our wind turbine model and the important design considerations in chapter 2. The wind turbine parameterization was implemented in a comprehensive atmospheric LES code, the Dutch Atmospheric Large-Eddy Simulation (DALES) model. DALES is used and maintained by researchers of several institutes, including Delft University (TUD), Wageningen University (WUR) and the Royal Dutch Meteorological Institute (KNMI) and is still in active development. DALES is one of the most all-round tested available atmospheric LES codes and has been extensively used over the course of more than two decades (Heus et al., 2010). The use of DALES is validated in a wide range of cases, including the stable nocturnal boundary layer (Beare et al., 2006), (shallow) cumulus (Siebesma et al., 2003, Van Zanten et al., 2011), stratocumulus (Duynkerke et al., 1999, 2004, Stevens et al., 2005) and transitions between the two (de Roode et al., 2016).

In chapter 3, we will validate our wind turbine model against observational studies conducted in stable and convective conditions. Together with providing validation of the model, this chapter shows the relevance of boundary-layer turbulence and atmospheric stability to wind energy. Besides individual wind turbines, a comparison is made against production data

of a wind farm in neutral and convective conditions.

In chapter 4 and 5, we address two particular cases in more detail, which fully demonstrate the possibilities of our modeling framework. Since DALES is capable of representing clouds, two cases were selected in which clouds plays a major role.

In the first detailed case study, we investigate the effect of stratocumulus clouds on wake evolution and wind farm performance. Based on their radiative properties, we expect stratocumulus clouds, which frequently occur over offshore wind farm sites, to have a distinct effect on wind farm performance. None of the previously mentioned LES-wind turbine models have been able to include the potentially significant impact of stratocumulus so far.

Finally, we consider probably the most famous example of the interaction between clouds and wind turbines: the observation of wake clouds at the Horns Rev offshore wind farm in February, 2008. First, a detailed reconstruction of the meteorological conditions is performed, by combining observational data with a careful consideration of atmospheric thermodynamics and boundary-layer dynamics. Then, we will try to explicitly simulate the formation of wake clouds with our model. This case provides an excellent test to see if our model is capable of representing the complex interaction between thermodynamics and turbulence in the lowest part of the atmosphere and the effect of wind turbines hereon.

2

The wind turbine model and its implementation in DALES

2.1. Design considerations

The most important characteristics of a wind power forecast model are general applicability and adequate performance in terms of computation time and accuracy. The first requirement, general applicability, is twofold. On the one hand, it refers to the ability to cover a wide range of atmospheric conditions in terms of wind speed, wind direction and stability. On the other hand, we require the model to handle different wind farms of various sizes and containing different types of wind turbines, by just providing different input, i.e. without any adjustments to the model.

The performance requirement with regards to computation time is strict: the model should run significantly faster than real time, otherwise it can, of course, never produce a forecast. As a first step we will investigate the possibility to run the model at least real time for an average-sized wind farm. Considering the computational power available for the current work, this condition directly sets a lower limit on the grid spacing of around 10 to 20 m.

The second performance requirement, sufficient accuracy, is more subtle. The resolution limit set by the previous requirement exclude models that explicitly resolve the flow around the wind turbine blades. Fortunately, actuator disk parameterizations of wind turbines on grid resolutions of 10 to 20 m have been shown to deliver decent results from 2-3 rotor diameters behind the wind turbine (Aitken et al., 2014b, Mirocha et al., 2014, Porté-Agel et al., 2011, Wu and Porté-Agel, 2013, 2015). Depending on the wind direction, wind turbines are typically spaced at least 5 rotor diameters apart in a wind farm. For this reason, an actuator disk approximation is suitable for study of wind farm wake effects. Furthermore, current NWP-based wind power forecast models are far from perfect (Devis et al., 2013, Xie et al., 2014). Combined with the considerable economic value of accurate wind power predictions, a slight performance improvement might already make LES a viable option.

Finally, from a practical perspective, it is preferable to minimize modifications to the core source code of DALES. Keeping the wind turbine-related routines separate from the main code ensures easy integration with future versions of DALES. This includes, as will be discussed in more detail later in this chapter, setting up the parallelization of the wind turbine computation independent from the domain parallelization of DALES.

2.2. Wind turbine parameterization

2.2.1. Rotor

Several (early) wind turbine-LES studies used the uniform actuator disk model (UADM), which only incorporates a uniformly distributed axial force (e.g. Calaf et al., 2010, Jimenez et al., 2007, 2008, Meyers and Meneveau, 2010, 2012). The magnitude of this force can be

straightforwardly obtained from one-dimensional momentum theory (Manwell et al., 2010). However, a constant value for the axial induction factor, i.e. the wind speed at the rotor disk relative to the free-stream wind speed, needs to be prescribed (Calaf et al., 2010).

The force on a real wind turbine is not equally distributed over the swept area of the blades. For example, at the root of the blade the force is relatively small due to non-optimal inflow conditions. Additionally, tangential forces play a non-negligible role in the development of the wake. The torque exerted by the wind on the blades induces a torque in the opposite direction on the flow through Newton's third law. Consequently, the wake starts to show a rotational motion which changes its structure considerably (Magnusson, 1999).

The UADM can be extended to include these effects by parameterization of the wind turbine force by Blade element theory, which incorporates a non-uniform force distribution and tangential forces. Further, within the non-uniform actuator disk model (NUADM), no a priori assumptions about the induction factor are required. The flow field in the LES will notice the presence of the actuator disk and the (local) induction changes automatically. This way, blade tip losses are also implicitly incorporated in the model (Sanderse et al., 2011).

In Blade element theory, the components of the wind turbine-induced force acting on the flow, F_i^{BE}, per unit area, are given by (Wu and Porté-Agel, 2011):

$$\frac{\mathrm{d}F_i^{\mathrm{BE}}}{\mathrm{d}A} = -\frac{1}{2}\rho V_{\mathrm{rel}}^2 \frac{N_B c}{2\pi r}\left(C_L e_{L,i} + C_D e_{D,i}\right). \tag{2.1}$$

In this equation, V_{rel} indicates the wind speed relative to the rotating blade, N_B the number of blades, c the chord length of the blade, r the distance from the hub, C_L (C_D) the lift (drag) coefficient of the airfoil and $e_{L,i}$ ($e_{D,i}$) the direction of the lift (drag) force, as explained in detail below.

The wind turbine force is described in a coordinate frame aligned with the wind turbine rotor, x_i ($i = 1, 2, 3$) with $(x_1, x_2, x_3) \equiv (x, y, z) \equiv \mathbf{x}$. We will refer to this frame as the rotor coordinate frame from hereon. For example Creech et al. (2015) also introduce a rotor coordinate frame, which simplifies the equations describing the wind turbine force considerably.

The rotor coordinate frame is related to the LES coordinate frame, x_i^*, by the following transformation:

$$x_i = Q_{ij}(-\psi)(x_j^* - x_j^{*\mathrm{hub}}), \tag{2.2}$$

where $x_i^{*\mathrm{hub}}$ are the coordinates of the wind turbine hub in the LES coordinate frame. The rotor coordinate frame is rotated over the yaw angle of the wind turbine with respect to the x^*-axis, ψ, by the rotation matrix for rotation around the z^*-axis, Q_{ij}. When the wind turbine is optimally aligned to the prevailing wind direction, the yaw angle is equal to the wind angle.

In the rotor coordinate frame, we can express the radius, r, and polar angle, θ, with respect to the wind turbine hub in a simple way:

$$r = \sqrt{y^2 + z^2} \tag{2.3}$$

$$\theta = \arctan\left(\frac{z}{y}\right). \tag{2.4}$$

See figure 2.1a for a schematic view of the two coordinates frames.

The local chord length, c, of each of the N_B blades, depends on the blade geometry and is provided as input. The lift (C_L) and drag (C_D) coefficients are obtained from tabulated air foil data as a function of the angle of attack, α. More details on the wind turbine characteristics that are required as input are given in section 2.4 and appendices D and E.

The angle of attack is defined as the difference between the angle of relative wind, γ ,

$$\gamma = \arctan\left(\frac{V_{\mathrm{ax}}}{\Omega r + V_{\mathrm{tan}}}\right), \tag{2.5}$$

and the local pitch angle, β_p, i.e.

$$\alpha = \gamma - \beta_p. \tag{2.6}$$

The local pitch angle is again a sum of the pitch angle of the blade, $\beta_{p,0}$, and the local twist angle, β_T. The twist angle depends on the blade geometry and can thus be provided as input. The pitch angle of the blade is actively controlled in modern wind turbines to regulate the torque on the blades. In the current model, this control behavior is parameterized by providing the blade pitch angle as a function of the free-stream wind speed as input.

The wind speed relative to the blade element consists of the local axial (V_{ax}) and tangential (V_{tan}) wind speed, plus the effect of the rotating blade:

$$V_{\text{rel}} = \sqrt{V_{\text{ax}}^2 + (\Omega r + V_{\text{tan}})^2}, \tag{2.7}$$

with

$$V_{\text{ax}} = u_1 \tag{2.8}$$
$$V_{\text{tan}} = -\sin\theta u_2 + \cos\theta u_3 \tag{2.9}$$

and Ω the rotational speed of the rotor. The local, rotated wind velocity components u_i, with $i = 1, 2, 3$ and $(u_1, u_2, u_3) \equiv (u, v, w) \equiv \mathbf{u}$, can be directly obtained from the simulations: $u_i = Q_{ij}(-\psi)u_j^*$, where u_i^* are the LES velocity components. The induced tangential velocity in the rotor plane, V_{tan}, is an effect of the torque exerted by the flow on the rotor and is directed opposite to the rotational direction of the wind turbine. See figure 2.1c for an illustration of the vectors and angles around the air foil.

Finally, the direction of respectively the lift, $e_{L,i}$, and drag, $e_{D,i}$, force are also described in the rotor coordinate frame, i.e. $e_i = Q_{ij}(-\psi)e_j^*$, and can be written as

$$e_{L,i} = (\cos\gamma, -\sin\gamma\sin\theta, \sin\gamma\cos\theta) \tag{2.10}$$
$$e_{D,i} = (\sin\gamma, \cos\gamma\sin\theta, -\cos\gamma\cos\theta)\,. \tag{2.11}$$

2.2.2. Tower and nacelle

Due to their relatively small dimensions compared to the rotor, the forces exerted on the tower and nacelle are typically one to three orders of magnitude smaller than the rotor force. For completeness we have, however, included these forces in the model.

Like Wu and Porté-Agel (2011), we model the nacelle and tower as actuator disks that exert a drag force, F^D, on the flow:

$$\frac{\mathrm{d}F^D}{\mathrm{d}A} = -\frac{1}{2}\rho C_D U^2. \tag{2.12}$$

The drag force is directed opposite to the wind and U represents the magnitude of the horizontal wind velocity, $U = \sqrt{u^{*2} + v^{*2}}$.

In atmospheric flows, the typical Reynolds number is of the order of 10^9 and we can assume the drag coefficient, C_D, to be constant. The nacelle is modeled as a bullet-shaped object, $C_D \approx 0.3$ (Wu and Porté-Agel, 2011). The tower is modeled as a vertical cylinder, $C_D \approx 0.4$ (Roshko, 1961). The tower radius, and hence the frontal area, usually decreases as a function of height. The model therefore linearly interpolates between the radius at ground level and at hub height, which are both provided as input.

2.3. Implementation in DALES

In this section, we will address the numerical implementation of the wind turbine force in DALES. For a general description of DALES see appendix A.

2.3.1. Rotor

The wind turbine model is implemented in DALES by adding a momentum sink, $\mathcal{F}^{\text{wt}}$, to the Navier-Stokes equation:

$$\left[\frac{\partial u_i^*}{\partial t}\right]^{\text{wt}} = \mathcal{F}_i^{\text{wt}}. \tag{2.13}$$

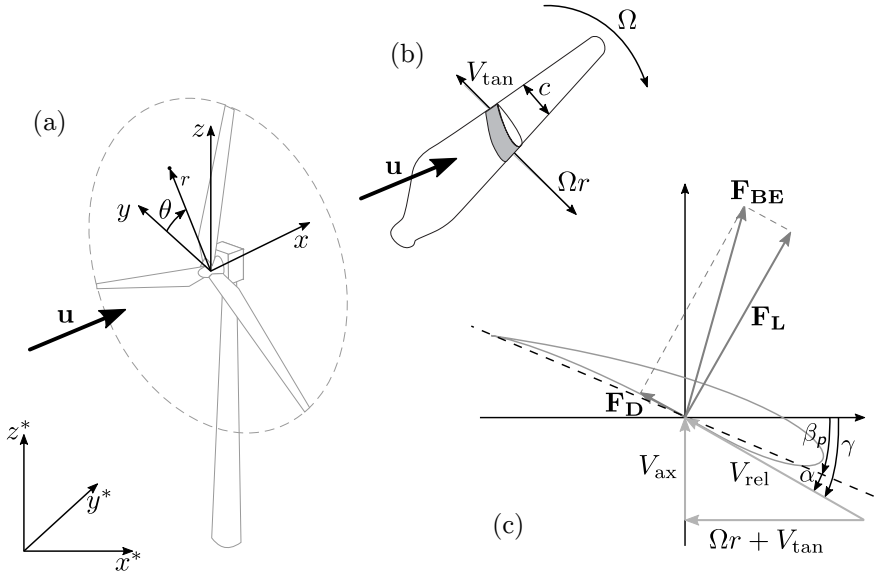

Figure 2.1: In (a), the LES coordinate frame (x^*, y^*, z^*) and the rotor coordinate frame (x, y, z) are depicted. The origin of the rotor coordinate frame is located at the hub of the wind turbine and x_1 is parallel to the rotor axis. The rotor coordinate frame is rotated with respect to the LES coordinate frame over an angle ψ, the yaw angle of the wind turbine. A detailed view of a single blade is given in (b), where the shaded area indicates a blade element. Further, (c) shows the cross section of such a blade element. The force on the blade element, $\mathbf{F}^{\mathrm{BE}}$, consists of a lift, $\mathbf{F_L}$, and drag force, $\mathbf{F_D}$. The angle relative to the wind, γ, is the sum of the angle of attack, α, and the local pitch angle, β_p. The local pitch angle is again the sum of two angles (not depicted in the figure): the blade pitch angle, $\beta_{p,0}$, and the local twist angle, β_T, i.e. $\beta_p = \beta_{p,0} + \beta_T$. Figure adopted from Burton et al. (2001).

Although the magnitude of $\mathcal{F}^{\mathrm{wt}}$ is in general given by equation (2.1), distribution of the momentum sink onto the appropriate LES grid points is not trivial. In the ABL, the wind direction is a function of time and space. The orientation (yaw angle) of the wind turbine needs to be actively controlled during the simulation in order to maintain optimal alignment of the wind turbine with respect to the prevailing wind direction. As a consequence, the rotor disk will in general not be aligned with the computational grid of the model. To overcome this issue we follow an approach similar to Meyers and Meneveau (2010), which has been employed in a range of wind turbine-LES studies (e.g. Allaerts and Meyers, 2015, Calaf et al., 2010, Goit and Meyers, 2014). More specifically, the wind turbine force components, on the LES grid locations $\mathbf{x}^*$, are given by:

$$\mathcal{F}_i^{\mathrm{wt}}(\mathbf{x}^*) = \mathcal{R}^N(\mathbf{x}^*) Q_{ij}(\psi) f_j^{\mathrm{wt}}(\mathbf{x}^*), \tag{2.14}$$

where $\mathcal{R}^N$ is a distribution function and f^{wt} is the wind turbine force per unit mass and per unit area.

The wind turbine force per unit mass and per unit area, f^{wt}, can be obtained by dividing equation (2.1) by the grid box air mass:

$$f_i^{\mathrm{wt}} = \frac{1}{\rho \Delta^3} \frac{\mathrm{d}F_i^{\mathrm{BE}}}{\mathrm{d}A} = -\frac{1}{2\Delta^3} V_{\mathrm{rel}}^2 \frac{N_B c}{2\pi r} \left(C_L e_{L,i} + C_D e_{D,i} \right), \tag{2.15}$$

where $\Delta \equiv \sqrt[3]{\Delta x^* \Delta y^* \Delta z^*}$ and Δx_i^* is the LES grid spacing. All terms in equation (2.15), except N_B and Δ, are a function of the grid coordinate and local wind velocity. Hence, (2.15) is evaluated at every grid point in the rotor disk. Furthermore, to ensure a realistic response to small-scale turbulent fluctuations, the LES velocity components are averaged in time first (see appendix B.3 for more details). The rotation matrix Q_{ij} rotates f_i^{wt} from the rotor coordinate frame back to the LES coordinate frame.

Throughout this work, the force per unit mass, i.e. the acceleration, in the LES coordinate frame is written as $\mathcal{F}$. Further, we denote the force per unit mass and per unit area in the rotor coordinate frame as f.

The first term on the right hand side of equation (2.14), $\mathcal{R}^N$, is a distribution function which we will refer to as the normalized geometrical footprint of the rotor. For convenience, we describe the geometrical footprint in the rotor coordinate frame. Then, $\mathcal{R}^N$ can be written as

$$\mathcal{R}^N(\mathbf{x}) = \pi R^2 \frac{\mathcal{R}(\mathbf{x})}{\sum\limits_{\mathbf{x}} \mathcal{R}(\mathbf{x})}, \tag{2.16}$$

where R is the radius of the rotor blades. In this equation, $\mathcal{R}$ is the rotor geometrical footprint as given in the work of Meyers and Meneveau (2010):

$$\mathcal{R}(\mathbf{x}) = \iiint G(\mathbf{x} - \mathbf{x}'') \delta(x'') H\left(R - r''\right) \mathrm{d}^3\mathbf{x}'', \tag{2.17}$$

where $\mathbf{x}''$ is an auxiliary integration coordinate. The rotor geometrical footprint is normalized in order to ensure its integrated value is conserved in the transformation to the discrete domain (Meyers, 2016). The area of the rotor disk is represented by the Dirac delta function, δ, which is only non-zero in the rotor plane ($x = 0$). The rotor disk itself is described by the Heaviside step function, H, that selects a circle of radius R around the hub. The rotor disk is distributed onto the grid points by convolution with a Gaussian filter of the form:

$$G(\mathbf{x}) = \left(\frac{6}{\pi \epsilon^2} \right)^{3/2} \exp\left(\frac{-6\|\mathbf{x}\|^2}{\epsilon^2} \right). \tag{2.18}$$

In line with Meyers and Meneveau, the filter width, ϵ, is set at 1.5 times the grid size to avoid numerical errors. The Gaussian filter is considered in more detail in appendix B.1. Further, the numerical computation of $\mathcal{R}$ is treated in appendix B.2.

The rotor geometrical footprint can be viewed as a distribution function that determines the fraction of the total rotor area that is distributed onto the area corresponding to a certain grid point. Figure 2.2a shows a plot of $\mathcal{R}^N$. Around the hub, all grid boxes are fully covered by the rotor and $\mathcal{R}^N$ has a constant, maximum value. We expect this value to be of the order

$$\frac{\pi R^2}{(2R/\Delta y^*)\,(2R/\Delta z^*)} = \frac{\pi}{4}\Delta y^* \Delta z^*, \tag{2.19}$$

which is indeed the case. Outside the rotor area the geometrical footprint is, of course, zero. Near the edge of the rotor disk, a transition region exists where $\mathcal{R}^N$ is in between its maximum value and zero. Besides representing the circular shape of the rotor on the rectangular grid, this region also provides spatial smoothing of the wind turbine force. The spatial smoothing in the axial direction is visible in figure 2.2b.

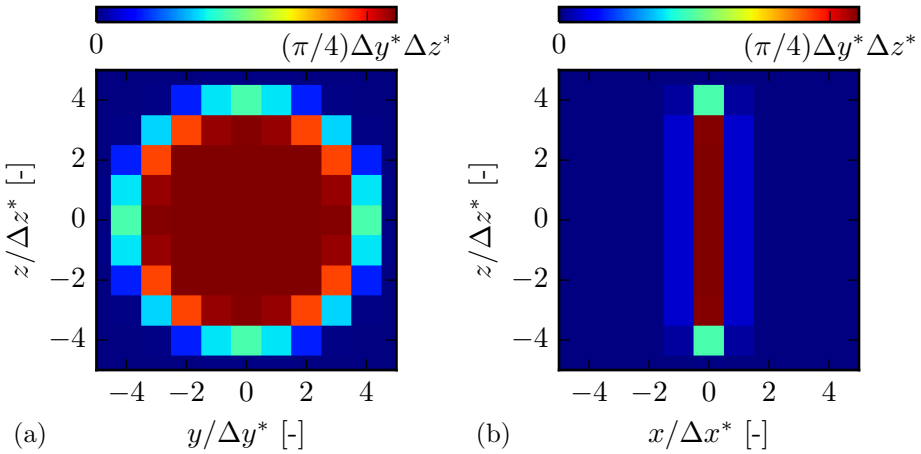

Figure 2.2: View of the rotor geometrical footprint, $\mathcal{R}^N$, looking into the (negative) x-direction (a) and (negative) y-direction (b). The hub is located at $x = y = z = 0$. The red areas indicate a high value of $\mathcal{R}^N$, i.e. the grid box area is fully covered by the rotor. Outside the rotor area $\mathcal{R}^N$ is zero. Each square represents the area of a grid box centered around the corresponding grid point.

2.3.2. Tower and nacelle

Like the rotor forces, the nacelle and tower force introduce a sink term in the momentum equation:

$$\left[\frac{\partial u_i^*}{\partial t}\right]^{\text{nac}} = \mathcal{F}_i^{\text{nac}} \tag{2.20}$$

$$\left[\frac{\partial u_i^*}{\partial t}\right]^{\text{tower}} = \mathcal{F}_i^{\text{tower}}. \tag{2.21}$$

We can write the force components of the nacelle and tower, on grid point $\mathbf{x}^*$, in a similar form as the expression for the rotor force in equation (2.14):

$$\mathcal{F}_i^{\text{nac}}(\mathbf{x}^*) = \mathcal{N}(\mathbf{x}^*) Q_{ij}(\phi) f_j^{\text{nac}}(\mathbf{x}^*) \tag{2.22}$$

$$\mathcal{F}_i^{\text{tower}}(\mathbf{x}^*) = \mathcal{T}(\mathbf{x}^*) Q_{ij}(\phi) f_j^{\text{tower}}(\mathbf{x}^*). \tag{2.23}$$

The force magnitude per unit mass and unit area, f_i^{nac} and f_i^{tower}, can be calculated from

equation (2.12):

$$f_i^{\text{nac}}(\mathbf{x}^*) = -\frac{1}{2\Delta^3} C_D^{\text{nac}} U^2 \delta_{i1} \tag{2.24}$$

$$f_i^{\text{tower}}(\mathbf{x}^*) = -\frac{1}{2\Delta^3} C_D^{\text{tower}} U^2 \delta_{i1}. \tag{2.25}$$

In contrast to the rotor force, the drag forces are always directed opposite to the wind. The nacelle and tower forces are therefore rotated over the local wind angle, ϕ, instead of over the yaw angle, ψ. The wind angle is given by $\phi = \arctan(v^*/u^*)$.

Finally, $\mathcal{N}$ and $\mathcal{T}$ are the distribution functions of the nacelle and tower. Since the span-wise frontal area of the tower and nacelle are typically smaller than the grid spacing, we choose to apply the associated forces on a single grid point. In the rotor coordinate frame, the following straightforward expressions then describe the nacelle and tower:

$$\mathcal{N}(\mathbf{x}) = A^{\text{nac}} \delta(\mathbf{x}) \tag{2.26}$$

$$\mathcal{T}(\mathbf{x}) = 2R^{\text{tower}}(z) \Delta z^* \delta(x) \delta(y) H(-z). \tag{2.27}$$

In the equations above, A^{nac} is the frontal area of the nacelle and R^{tower} is the radius of the tower, which is usually a function of height.

2.3.3. Example of the wind turbine force distribution

A typical distribution of the wind turbine force (per unit mass) is shown in figure 2.3. The lift force is maximized at the mid-sections of the blades where the inflow angle is optimal (Magnusson, 1999). Figure 2.3b shows that indeed the largest axial force is found in this region. From the same figure we can also conclude that the contribution of the nacelle and tower are relatively small, as expected. The effect of the rotating blades is clearly visible in figures 2.3c and 2.3d. For example, above the hub the blade moves primarily in the horizontal direction and the y-component is maximized. Finally, the axial smoothing of the rotor force can be identified in figure 2.3a by the non-zero forces before and behind the rotor.

2.3.4. Extracted power

In the model, the power extracted from the atmosphere is calculated from the torque, τ, that is exerted on every grid point within the actuator disk:

$$\tau(\mathbf{x}) = r f_i^{\text{wt}}(\mathbf{x}) \hat{\theta}_i \rho \Delta^3 \mathcal{R}^N(\mathbf{x}). \tag{2.28}$$

The magnitude of the wind turbine force per unit mass and per unit area, f^{wt}, is multiplied by the grid box air mass and the fraction of the wind turbine rotor area that is located on grid point $\mathbf{x}$, $\mathcal{R}^N(\mathbf{x})$. From this, the tangential component is calculated by taking the dot product with the unit vector in the tangential direction, $\hat{\theta}_i$. Finally, by multiplication by the radial distance from the hub, r, we arrive at the torque. The total extracted power, P, can then be obtained by summing the torque over all grid points and multiplying by the rotational speed of the wind turbine:

$$P = \Omega \sum_{\mathbf{x}} \tau(\mathbf{x}). \tag{2.29}$$

2.4. Wind turbine characteristics

A wind turbine parameterization based on Blade element theory, like implemented in our model, is sensitive to the blade geometry (c and β_T) and air foil data (C_L and C_D) that is provided as input. Furthermore, in the current implementation, information on the rotational speed, Ω, and pitch angle of the blade, $\beta_{p,0}$, as a function of free-stream wind speed is required as well. In modern wind turbines, however, the rotational speed and blade pitch angle are actively controlled. Implementation of a model to mimic this control behavior is one of the priorities for further development of our model.

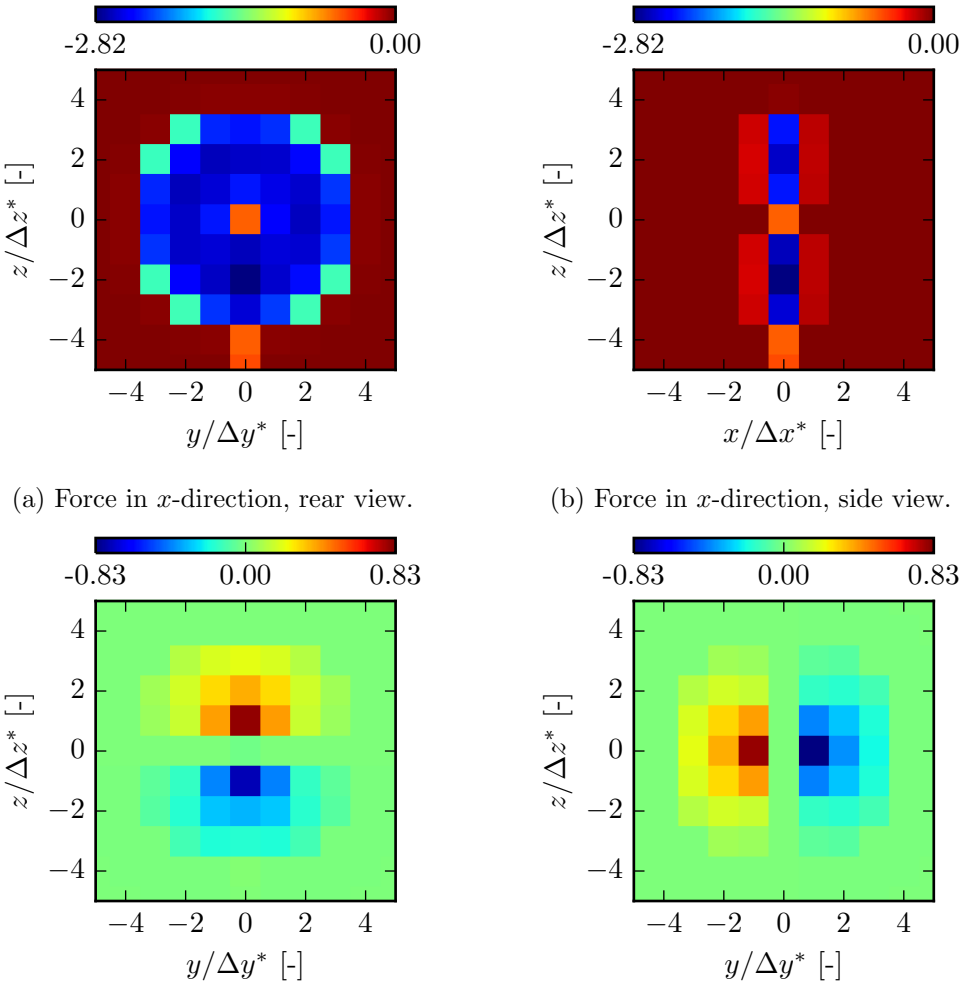

(a) Force in x-direction, rear view.

(b) Force in x-direction, side view.

(c) Force in y-direction, rear view.

(d) Force in z-direction, rear view.

Figure 2.3: Components of the wind turbine-induced force per unit mass [m/s^2] in a plane at $x = 0$. The axial force is also plotted in a plane at $y = 0$ to demonstrate the axial smoothing of the force. Each square represents the area of a grid box centered around the corresponding grid point. The hub height wind speed was about 8 m/s, and typical values of $\Delta x^* = \Delta y^* = \Delta z^* = 10$ m and $R = 40$ m were used.

Detailed data on the characteristics of commercial wind turbines is generally not available. The most important characteristics can in some cases be reconstructed or approximated for a certain wind speed range. Lu and Porté-Agel (2011) represented a Vestas V112 3 MW wind turbine by using linear approximations for the chord and twist distribution, plus data of an air foil that resembled the one used for this particular turbine. Porté-Agel et al. (2011) implemented a Siemens SWT-2.3-93 2.3 MW turbine, based on a rather sparse description of its characteristics by Laursen et al. (2007) and Leloudas (2006). A more detailed description of this particular wind turbine was later given by Creech et al. (2015). Similarly, Wu and Porté-Agel (2015) reconstructed the important parameters of the Vestas V80 2 MW wind turbine for their study of the Horns Rev wind farm. Besides these commercial wind turbines, complete design data is available for the NREL 5 MW reference turbine (Jonkman et al., 2009). More details on the required input data are given in appendix D. Additionally, example input files for the Vestas V80 can be found in appendix E.

To test the validity of the representation of the wind turbines in DALES, the calculated wind turbine power can be compared with the power curve of the wind turbine. The power curve shows the wind turbine power as a function of hub height wind speed and is one of the most important characteristic of a wind turbine. Currently, the model only computes the extracted power (equation 2.29). In a real wind turbine, e.g. mechanical and electrical losses also play a role. Still, comparison with the power curve can give an indication if, and in which wind speed range, our model for the wind turbine force is valid.

The manufacturer's power curve shows an expected relationship between the hub height wind speed and the power production in standard conditions. As Gill et al. (2012) point out, comparing operational data, or LES results for that matter, to this curve is difficult for several reasons. For example, it is not trivial to relate the measurements of e.g. a nacelle mounted anemometer to the 'real' free-stream wind speed. Moreover, the free-stream wind speed is not unambiguously defined itself. As will be treated in detail in chapter 3, the vertical wind speed profile that corresponds to a certain hub height wind speed strongly depends on the turbulence structure of the ABL. The total power in the wind, integrated over the rotor area, again depends on the vertical wind speed profile. So, for a given hub height wind speed, the power that the wind turbine can extract from the atmosphere varies from case to case. This effect can be included by e.g. defining a rotor-equivalent wind speed (Wagner et al., 2009). However, for now we will only consider the power as a function of the average hub height wind speed upstream of the wind turbine.

With the above in mind, we choose to study the power production in neutral conditions and focus on a qualitative comparison. The REF case from the study of Allaerts and Meyers (2015) was selected to represented a neutral boundary layer (NBL). The geostrophic wind speed was increased over the course of several hours from 6 to 15 m/s. We considered both wind turbines of which all required data was available: the Vestas V80 2 MW and the NREL 5 MW reference turbine. The results are shown in figure 2.4.

The power as calculated by DALES shows good correspondence with the power curve of the Vestas V80 (figure 2.4a). This could be expected, as Wu and Porté-Agel (2015) essentially reverse engineered the wind turbine characteristics from the power and thrust curves. However, DALES calculates the power that the rotor extracts from the atmosphere, which does not include mechanical and electrical losses. Therefore DALES might actually slightly underestimate the real extracted power in this case.

Jonkman et al. (2009) provided both the rotor power and generator power of the NREL 5 MW reference turbine. As DALES only calculates the extracted wind power, we choose to compare our model with the rotor power curve. The slope of the power curve is represented quite accurately, but DALES clearly overestimates the extracted power over the whole wind speed range.

The current model can certainly reproduce the general power curve characteristics correctly in a qualitative way but further development is necessary. Particularly the addition of active rotational speed and blade pitch control is a priority. For example Creech et al. (2015) already implemented more realistic control behavior. Additionally, a model for the conversion of ex-

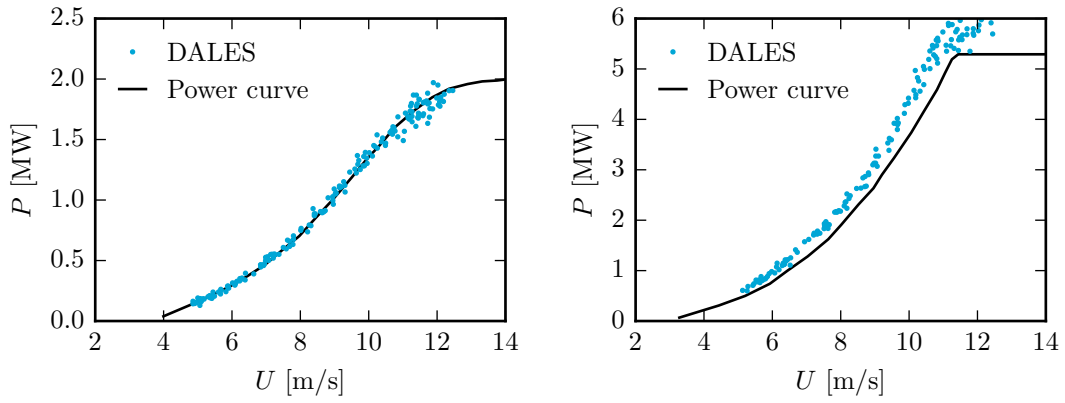

(a) Vestas V80 2 MW.

(b) NREL 5 MW reference turbine.

Figure 2.4: 2 min-average power production of two different wind turbines as calculated by DALES, compared with the power curve of the manufacturer (a) and with the design power curve (b).

tracted power to electrical power needs to be implemented. See section 6.2 for more details on possible improvements of the wind turbine model.

2.5. Yaw control and misalignment

The necessity of dynamic yaw control was already briefly mentioned at the start of section 2.3. In the current model, a simple yaw control system is used where each wind turbine is aligned to the local 1 min-average wind direction at hub height.

Whenever the wind direction is not optimally aligned (perpendicular) with respect to the rotor plane, so-called yaw misalignment occurs. In chapter 3 we will see that, depending on the turbulence in the ABL, the wind direction can be a distinct function of height. Thus, even when the rotor is aligned perfectly to the wind at hub height, parts of the rotor plane above and below hub height will experience a yaw error. As a result of the suboptimal inflow angle of the wind, less torque is exerted on the blade and the contribution of these parts of the rotor to the power production decreases (Burton et al., 2001).

In the previous section we noted that the total power that can be extracted from the wind, given a certain hub height wind speed, depends on the wind speed profile and thus the particular atmospheric conditions. Similarly, the change of the power as a function of the hub height yaw error depends on the profile of the wind direction, which again depends on the atmospheric conditions. In theory, the power deficit could under some conditions be an asymmetric function of the yaw error, and the power could even increase if a slight misalignment occurs at the hub. Although a detailed study into yaw optimization is beyond the scope of this report, it can certainly be part of future research (section 6.3).

In our model, the wind turbine force is based on the local wind velocity at each grid point (equation 2.15), and hence the effect of yaw misalignment is implicitly incorporated. To test how well yaw misalignment is represented, we deliberately put an offset to the yaw angle with respect to the mean (hub height) wind direction. By comparing the extracted power for a range of different offsets with the aligned case, we can identify the power deficit due to yaw misalignment. From one-dimensional momentum theory, one would expect the power to drop as $\cos^3(\psi - \phi)$, where ψ is the yaw angle and ϕ is the wind direction. Empirical data, however, suggests that the relation could be cosine squared instead of cubed (Madsen et al., 2003).

The same NBL case as in section 2.4 was selected for the LES. The results of DALES are shown together with the empirical curve in figure 2.5. The relative power is close to the empirical curve in the relevant range. Indeed, we find that the power relative to the aligned

case is an asymmetric function of the yaw error. More specifically, the power deficit is slightly higher in case of a negative yaw error.

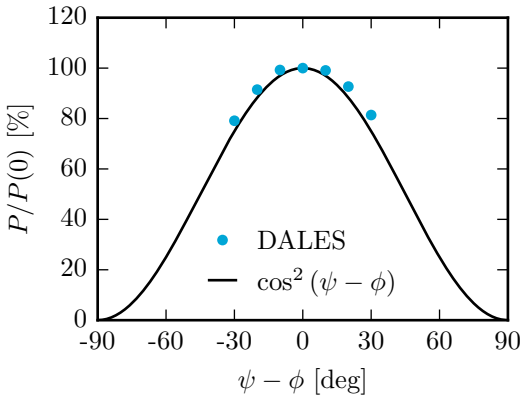

Figure 2.5: The 30 min-average power of the wind turbine as a function of the yaw error. The power is normalized by the power in case the rotor is aligned at hub height. The black line shows the effect of yaw misalignment on power production based on empirical data (Madsen et al., 2003).

2.6. Boundary conditions

In all atmospheric LES models, including DALES, periodic boundary conditions are applied in the horizontal direction. Due to the induced wake region, a simulation is no longer homogeneous when a wind turbine is immersed in the flow. This can become problematic since the wind turbine under consideration can be located within its own wake region, as illustrated in figure 2.6a. Consequently, the wind turbine can reduce the (slab-averaged) wind speed over the entire domain if the wake keeps propagating through the domain several times. Furthermore, strong turbulence is associated with the wake region. Periodic boundary conditions will thus increase the ambient turbulence levels considerably, which can have a distinct impact on the evolution of the wake.

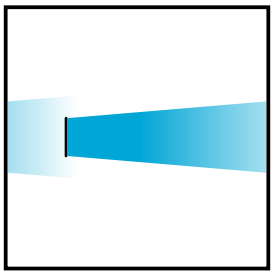

(a) A wind turbine (black line) located in its own wake region (blue), as would occur when periodic boundary conditions are applied.

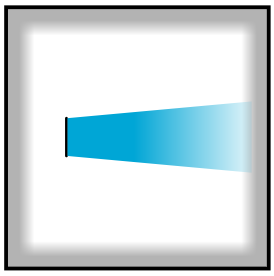

(b) Prescribing values from a reference simulation without a wind turbine to the boundaries of the wind turbine simulation (grey region) prevents the wake from re-entering the domain.

The most straightforward solution would be to enlarge the horizontal domain up to a point where the wake region has completely disappeared due to entrainment of momentum by turbulence. Especially in case of wind farms, this would lead to impractically large simulation domains. Several observational studies have actually shown that wakes can extent up to

distances of 10 to 20 km downstream of the wind farm (Christiansen and Hasager, 2005, 2006, Li and Lehner, 2013).

To overcome this issue, a fully turbulent inflow boundary condition can be prescribed. Turbulent inflow conditions can be generated synthetically or by precursor methods, see Munters et al. (2015) for more details. When simulating real atmospheric conditions, a precursor method is the only option. The precursor simulation, without wind turbines, generates fully developed turbulent fields, which are then prescribed to the boundaries of the wind turbine simulation (Churchfield et al., 2012a, Munters et al., 2015, Stevens et al., 2014, Wu and Porté-Agel, 2011).

One option is to save a plane of the turbulent fields at every time step for a certain period, once a quasi-equilibrium state has been reached in the precursor simulation (Churchfield et al., 2012a). A major advantage of this approach is the option to run numerous different wind turbine simulations from a single precursor simulation. However, for a simulation where an equilibrium state is not achieved, like during a diurnal cycle, this method implies storage of turbulent fields (u^*, v^*, w^* and θ_l, but also q_t when moist is included) at every time step for a runtime up to 24 h.

Therefore, we choose a solution similar to Stevens et al. (2014), that introduces the advantages of inflow-outflow boundary conditions, while keeping the periodic boundary conditions of the model. The formulation of Stevens et al. is, however, restricted to a static inflow direction, along the positive x-axis. Munters et al. (2015) extended on this work to allow for variable inflow directions. Our implementation is again slightly different but also has no limitations with regard to wind direction and time evolution of the ABL.

First, a spin-up simulation is performed without wind turbines to allow development of the flow. Then, two concurrent (simultaneous) simulations, from now on referred to as the reference and the wind turbine simulation, are initialized with the results of the spin-up simulation. At every time step, the values of the prognostic variables of the reference simulation, χ_{ref}, where $\chi \in \{u_i^*, q_t, \theta_l, e\}$, are prescribed to the boundaries of the wind turbine simulation.

A smooth transition at the boundary is required to minimize potential numerical errors. Inspired by how the boundaries are handled in limited-area atmospheric models (e.g. Schalkwijk et al., 2014, van Lipzig, 1999), the boundaries are prescribed in the following manner:

$$\left.\frac{\partial \chi}{\partial t}\right|^{\mathrm{bc}^+} = (1-a)\left.\frac{\partial \chi}{\partial t}\right|^{\mathrm{bc}^-} + a\,\frac{\chi_{\mathrm{ref}} - \chi}{\Delta t}, \tag{2.30}$$

where the superscripts bc^- and bc^+ indicate, respectively, the tendency of χ before and after prescribing the boundaries and Δt is the time step of the model. The weighting function a ensures a smooth transition between the boundary region and the inner domain. At the boundary $a = 1$, and a gradually decreases to zero over the course of ~ 10 grid points when moving away from the boundary.

At the cost of increased computational effort, this approach allows for the simulation of wind turbines in essentially all regular LES cases, without issues related to the boundary conditions.

Finally, instead of running an identical precursor simulation, the boundaries can be provided by a large-scale turbulent-resolving simulation on a lower resolution (Aitken et al., 2014b, Mirocha et al., 2014). This so-called nesting approach can be extended to provide mesoscale inflow to the LES, which can deliver realistic, time-varying boundary conditions for the wind turbine simulation. As this could be a promising addition to our modeling framework, we will come back to it in more detail in section 6.2.

2.7. Parallelization

The wind turbine model requires computation of the wind turbine forces at every time step. Additionally, the geometrical footprint needs to be recalculated every time the rotor orientation, i.e. the yaw angle, changes. These computation can be handled efficiently for many wind turbines by parallel computation.

The location and characteristics of each wind turbine are distributed to a different processing unit, which will perform all calculations concerning one particular wind turbine. Of

course, this does require that the number of available processing units is larger than or equal to the total number of wind turbines in the wind farm under consideration. Large wind farms typically consist of 50 to 150 wind turbines. Generally, a high resolution ($< 20\,\mathrm{m}$) LES of the area covered by a large wind farm ($\sim 5\,\mathrm{km} \times 5\,\mathrm{km}$) already requires about the same amount of processing units. The lower limit on the required number of processing units is therefore fulfilled by default.

Every wind turbine process requires knowledge of the (simulated) wind velocity components in a square area centered around the x^*, y^*-location of the wind turbine. The size of this area is determined by the turbine radius plus 2-3 extra grid points on each side depending on the amount of spatial smoothing that is applied. In DALES, the computational domain is divided into rectangular subdomains which are distributed over the available processing units. The subdomains of DALES will in general not coincide with the subdomains of the wind turbine processes. Especially when the wind farm layout is not rectangular, it may not be possible to match these subdomains all together. Figure 2.7 shows an illustration of this problem.

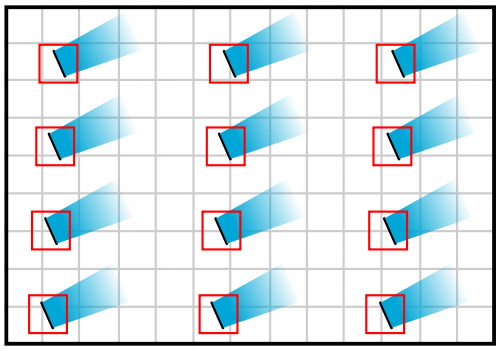

Figure 2.7: The relative locations of the wind turbines (black lines) are determined by the wind farm layout. The subdomains of DALES (grey squares) will therefore in general not coincide with the wind turbine subdomains (red squares). The parallelization of DALES is therefore decoupled from the parallelization of the wind turbine calculation.

To resolve this mismatch in a general way, we decouple the parallelization of DALES from the parallel computation of the wind turbine forces. In each iteration, before the wind turbine calculation, the wind velocity components of each subdomain of DALES are communicated to all processing units. Every unit then extracts the values of the subdomain corresponding to the wind turbine allocated to this unit and the wind turbine forces are calculated. The results are then communicated back to the respective subdomains of DALES, and the calculated forces are applied on the proper grid points.

3

Atmospheric stability and its relevance to wind energy

3.1. Introduction

In this chapter we will take a detailed look at the important role of atmospheric turbulence with regard to wind farm performance. While particularly the first part will also provide a general introduction to boundary-layer turbulence and atmospheric stability, the primary focus of this chapter is to test our model in several conditions and validate against real world observations.

We will start by considering the primary physical mechanisms that dictate the turbulence structure of the ABL. First of all, frictional drag at the surface induces wind shear which lead to the production of turbulent motions. Secondly, thermal effects also play a major role in the development of turbulence. Where wind shear always lead to the production of turbulence, buoyancy effects can cause both the production and destruction of turbulent motions according to the temperature stratification. An air parcel that is warm relative to its environment has a lower density and tends to rise. For example, during a sunny day over land, when the ground is heated by solar radiation (blue line in figure 3.1a), thermals of warm air will start to rise from the surface (blue line in figure 3.1b). These large convective motions drastically increase turbulent mixing in the boundary layer and we speak of convective or unstable conditions. In contrast, during a clear night, the land surface cools and the situation is entirely different (black line in figure 3.1a). A layer of relatively cold air forms at the surface and the development of turbulent motions is suppressed by buoyancy effects (black line in figure 3.1b). These are just two straightforward examples of how thermal effects play a role in the development of boundary-layer turbulence during the diurnal cycle.

In reality the interaction between a wide range of variables establishes the structure of the turbulent boundary layer. Nonetheless, a specific distinction can be made between the boundary-layer structure over land and over sea (Garratt, 1994). Due to its large heat capacity, water can absorb a considerable amount of heat with little temperature change. Consequently, the diurnal cycle of solar radiation that is so apparent over land is much less profound over the sea (Stull, 1988). Secondly, clouds often form within or immediately above the marine ABL. Boundary-layer clouds like stratocumulus are in fact that common over the oceans that we will consider their effect on wake dynamics separately (see chapter 4). Finally, the relatively low roughness length of the sea surface leads to less mechanical production of turbulence.

Turbulence has a significant effect on the vertical wind velocity profile. In general, the well known Log profile for the wind speed (grey line in figure 3.2a) is only valid in neutral conditions (Stull, 1988). In the convective boundary layer (CBL), turbulence efficiently mixes momentum in the vertical direction, leading to a situation where the wind speed and wind direction are more or less constant with height through most of the boundary layer (blue lines in figure 3.2a and 3.2b). Close to the surface the wind speed is higher as compared to neutral conditions, in contrast to relatively low wind speeds higher up in the boundary layer.

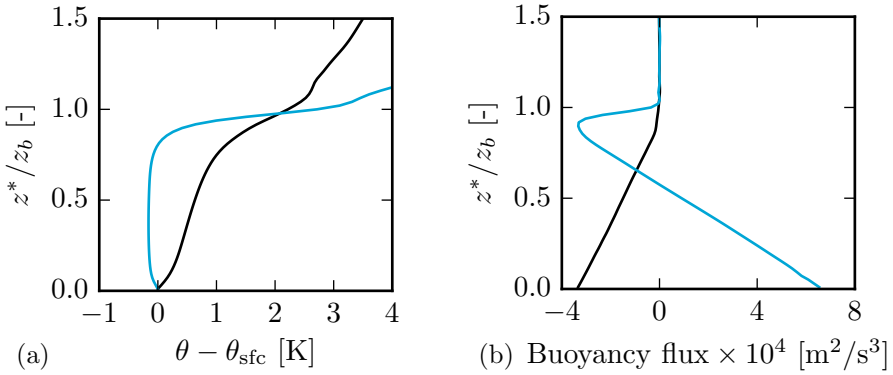

Figure 3.1: Potential temperature (a) and buoyancy flux (b) in stable (black) and convective (blue) conditions. The potential temperature is taken relative to the surface (θ_{sfc}) and the buoyancy flux is defined as $g\overline{w'\theta_v'}/\theta_v$. The height is normalized by the boundary layer height, z_b, to allow comparison between the two boundary layers. The profiles are taken from two of the case studies (Aitken et al., 2014b, Mirocha et al., 2014) that will be considered in more detail later.

The opposite occurs in stable conditions, where vertical mixing of momentum by turbulence is much less profound. In the stable boundary layer (SBL) the wind speed can even become supergeostrophic at some height through the formation of a low-level or nocturnal jet (black line in figure 3.2a). Typically located at a height of 100 to 300 m above the surface, this phenomenon definitely affects present-day wind turbines whose tip heights can already exceed 150 m. At the cost of increased mechanical strain on the blades due to strong wind shear, the high wind speed in a low-level jet may significantly increase power production (figure 3.2c, Sisterson and Frenzen, 1978, Storm et al., 2009). Additionally, the wind direction can vary as much as 30° from the surface to the top of the ABL in stable conditions (black line in figure 3.2b). This so-called Ekman spiral is an effect of the balance between turbulent friction, the pressure gradient and the Coriolis force.

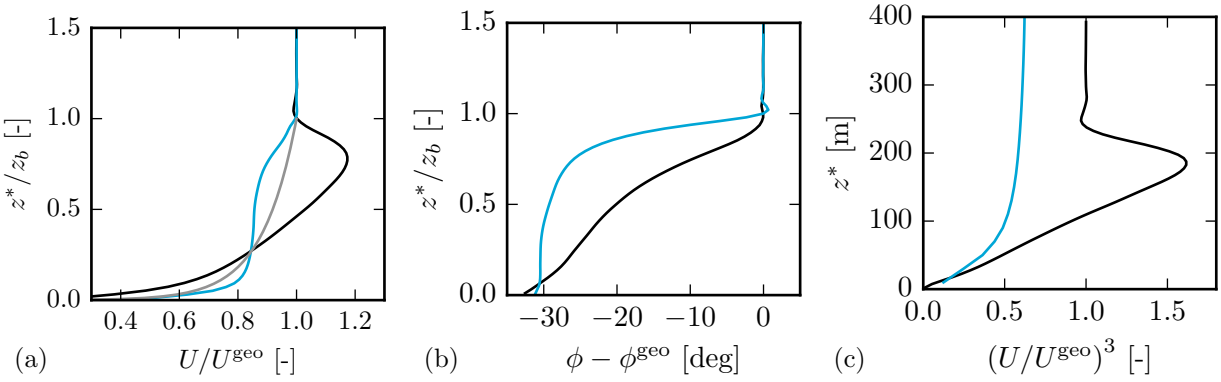

Figure 3.2: Wind speed (a), wind direction (b) and specific power in the wind (c) in stable (black) and convective (blue) conditions. The Log law for the wind speed that is valid in neutral conditions is shown in grey in (a). In (a) and (b) the height is normalized by the height of the boundary layer, z_b. The profiles are taken from two of the case studies (Aitken et al., 2014b, Mirocha et al., 2014) that will be considered in more detail later.

Besides its considerable effect on the wind velocity, atmospheric stability has a distinct influence on wake evolution too. The rest of this chapter is primarily dedicated to this effect. First, we will conduct a study similar to Abkar and Porté-Agel (2015), who performed a LES study of wake evolution in a SBL, NBL and CBL. In contrast to the work of Abkar and Porté-Agel, the cases we will consider are based on real world conditions to allow for comparison with observations. In the second part of this chapter, we will compare simulated power deficits in an operational wind farm with production data of this particular wind farm in convective and neutral conditions.

3.2. Wake evolution behind a single wind turbine

The first two studies we will consider are described by Mirocha et al. (2014) and Aitken et al. (2014b), who compared their LES model with measurements behind a 2.3 MW wind turbine in convective and stable conditions. The third observational study was conducted by Käsler et al. (2010), who performed LiDAR measurements in the wake of an Areva Multibrid M5000 5 MW wind turbine in stable conditions.

3.2.1. Case description

The setup of the simulations is based on on-site meteorological measurements. Mirocha et al. prescribed a geostrophic wind forcing of 14.5 m/s orientated from 292.5° which resulted in an average hub height wind speed close to the measured value. A surface heat flux of 20 $\mathrm{W/m^2}$ was set to simulate weakly convective conditions.

For their SBL simulation, Aitken et al. specified a geostrophic wind of 7.5 m/s orientated from 295°, again resulting in an average hub height wind speed in line with the observations. Based on temperature measurements at 2 m height, a surface cooling rate of 0.2 K/h was applied to simulate stable conditions. For a full description of the simulation setup we refer to the original articles.

Specifics about the wind turbines under investigation were not disclosed, apart from the hub height (80 m) and blade diameter ($D = 100$ m). Mirocha et al. mentioned a rated power of 2.3 MW. Our force parameterization does, however, require detailed information about the wind turbine under consideration. Considering the wind turbine data that is available, we choose to use the Vestas V80 2 MW wind turbine. Although this turbine has a smaller diameter (80 m), we expect similar wake behavior when the downstream distance is normalized by the rotor diameter (Bastankhah and Porté-Agel, 2014).

In the SBL case the grid resolution was set to 5 m to ensure a sufficient part of the turbulence spectrum is resolved. A domain size of 1 km × 0.5 km × 0.4 km was used to have at least $10D$ of domain in the stream-wise direction that is not affected by prescribed boundaries. Large-scale turbulent motions in convective conditions allow a much coarser resolution, making the wind turbine model the limiting factor. Wu and Porté-Agel (2013) found that for a proper representation of the wind turbine in the non-uniform actuator disk model, at least 5 (7) grid points are required along the diameter of the rotor in the span-wise (vertical) direction. Accordingly, the grid spacing was set to 12.5 m in the horizontal direction and 10 m in the vertical direction. The vertical grid spacing was gradually increased to 20 m above 200 m. The domain size was taken to be 2.5 km × 2.5 km × 2 km (de Roode et al., 2004).

During the measurements of Käsler et al., the wind was blowing from a north-eastern direction at about 7.5 m/s at hub height (102 m). The atmospheric conditions were reported to be stable, with a hub height turbulence intensity of 2.8 %. For the LES we selected the GABLS1 case described by Beare et al. (2006), a case which shows a hub height wind speed and turbulence intensity similar to the on-site conditions reported by Käsler et al. Although our wind turbine implementation incorporates yaw control, the geostrophic wind of 8 m/s was rotated over an angle of −20° with respect to the x-axis to limit the required span-wise domain size.

Since detailed information about the Areva Multibrid M5000 was not available, the NREL 5 MW reference wind turbine was used instead. Both turbines have the same rated power and a similar rotor diameter (116 m vs. 126 m). Furthermore, Jonkman et al. (2009) mention that

the NREL 5 MW reference wind turbine is based to some degree on a prototype of the Areva Multibrid M5000.

The domain size was set similar to the SBL case of Aitken et al. (2014b) described above. The resolution was set to 3.125 m in all directions to prevent the LES from becoming dominated by the sub-filter scales.

We will first study the structure and characteristics of the wakes in a qualitative manner. Then, a model from literature is fit to the simulation results in order to perform a quantitative comparison with measurement data.

3.2.2. Wake structure and characteristics

In this section we will focus on the wake of the Vestas V80 wind turbine in the stable and convective cases described above.

Wind speed

Contour plots of the instantaneous and 10 min-average wind speed in stable and convective conditions are shown in figure 3.3 and 3.4. The wind speed has been normalized to facilitate comparison between the figures. The vertical wind velocity in a horizontal plane at hub height is given in figure 3.5. Finally, vertical and span-wise profiles of the (time-average) wind speed in front of the turbine and in the wake can be found in figure 3.6.

From only looking at the wind speed distribution around the wind turbine, we can already identify several distinct wake characteristics. The instantaneous wind speed contours show that the wake structure is highly transient. Properties of the wake can essentially only be considered in a statistical sense, as the 10 min-average wind speed shows.

Especially in stable conditions it is evident that the near wake consists of two separate regions of maximum velocity deficit at the mid-sections of the blades (grey lines in figure 3.6a and 3.6b). In this section the inflow conditions are optimal and the blades produce maximum lift. Consequently, the amount of kinetic energy that is extracted from the wind is also maximized. Suboptimal inflow conditions at blade root and tip losses at the tip of the blades lead to relatively small velocity deficits (Magnusson, 1999). The two wakes merge farther downstream by turbulent mixing (blue lines in figure 3.6a and 3.6b). In convective conditions this feature is much less distinct due to stronger turbulent mixing (grey lines in figure 3.6c and 3.6d).

In stable conditions the wake is also not symmetric around its centerline in the horizontal direction (grey line in figure 3.6b). The rotational motion of the blades induces wake rotation in the opposite direction (figure 3.5a). The strong wind shear over the wind turbine in stable conditions (black line in figure 3.6a) leads to the upward transport of relatively low momentum air on the updraft side of the rotational motion in the wake. In contrast, higher momentum air is transported downward on the other side of the wake centerline. Consequently, the velocity deficit is larger on the updraft side (Magnusson, 1999). Indeed, the updraft side of the wake rotation in figure 3.5a corresponds with the region in the wake where the lowest wind speed is observed in figure 3.3b. The asymmetric wake structure in stable conditions can also be observed in the LES study of Abkar and Porté-Agel (2015).

Finally, the velocity fields as calculated by DALES show a good agreement with the results of Aitken et al. (2014b) and Mirocha et al. (2014).

Turbulence

The relatively low wind velocity in the wake leads to the formation of a shear layer at the interface between the wake and the undisturbed flow. Further, the suboptimal inflow conditions around the hub of the wind turbine lead to a relatively low velocity deficit around the wake centerline in the near wake. In both regions we expect to find a large amount of turbulence produced by shear. To quantify the total turbulence levels in the wake, we calculate the turbulence kinetic energy (TKE).

First, we decompose the wind velocity in a time average part, $\langle u_i \rangle$, and a fluctuating part, u_i', i.e.

$$u_i = \langle u_i \rangle + u_i'. \tag{3.1}$$

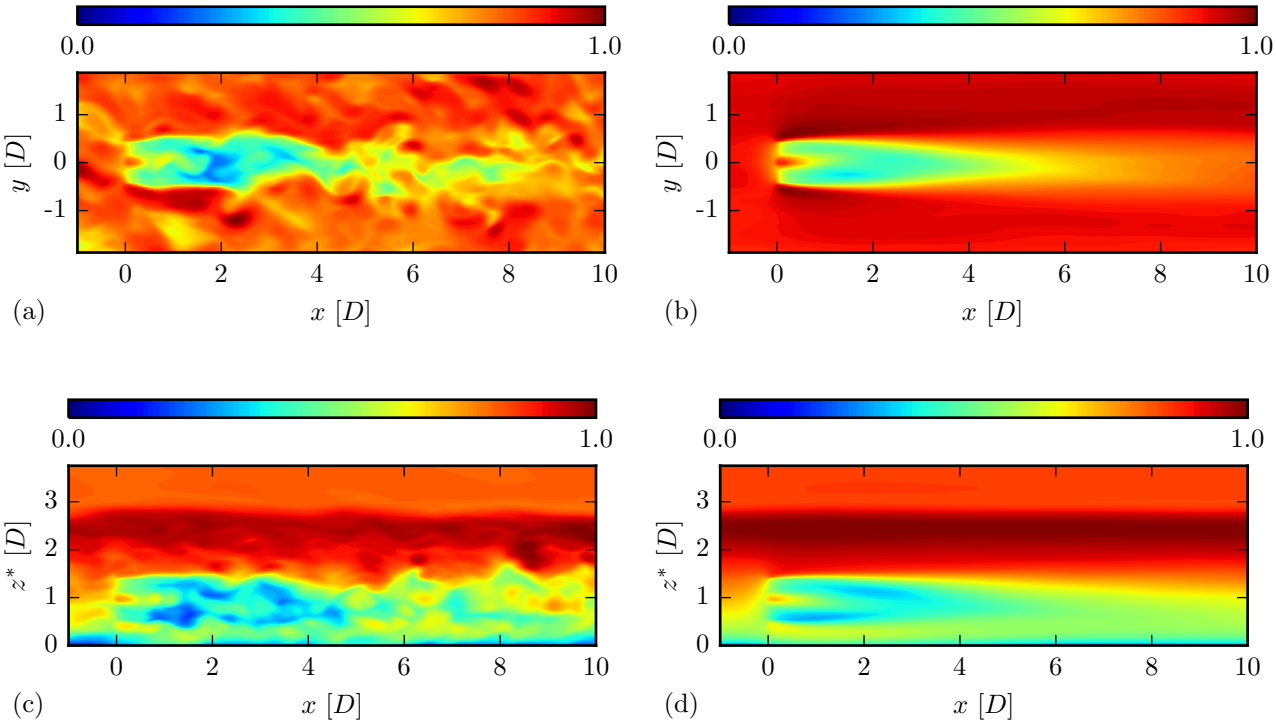

Figure 3.3: Instantaneous (a and c) and 10 min-average (b and d) normalized wind speed in the SBL case of Aitken et al. (2014b). The top two figures show a horizontal plane at hub height, where the lower two figures show a vertical plane at $y = 0$.

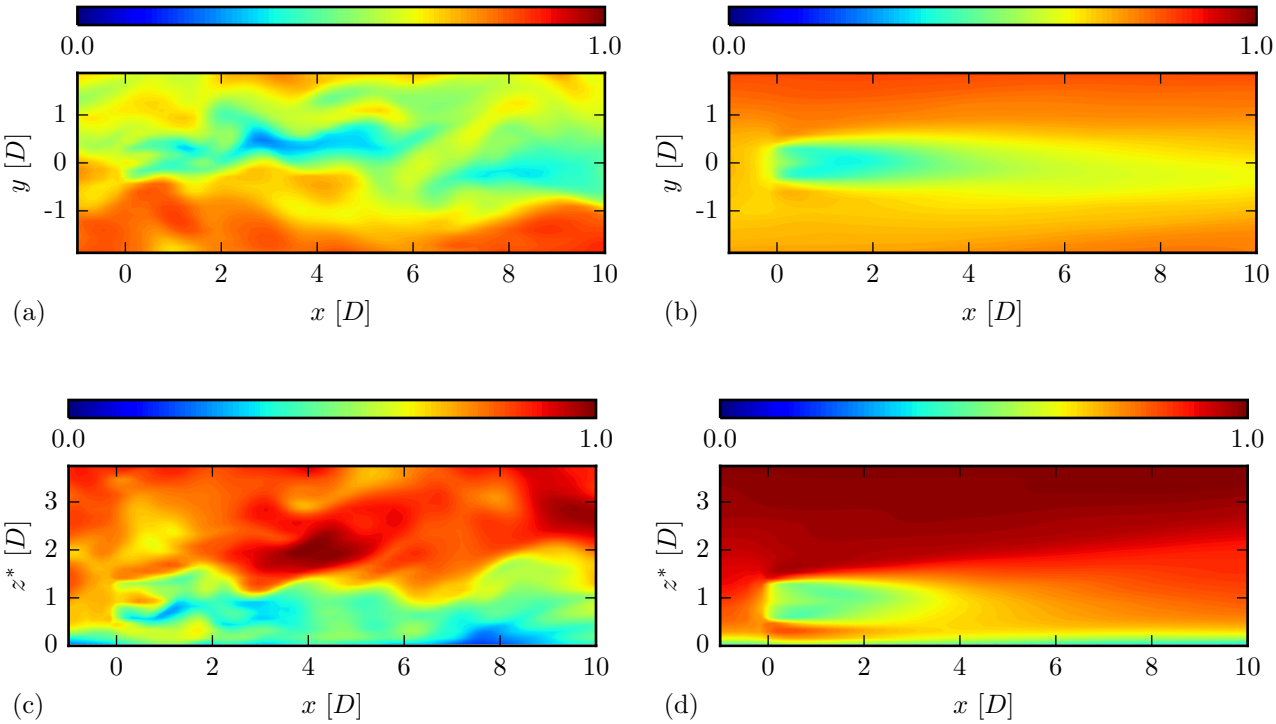

Figure 3.4: Instantaneous (a and c) and 10 min-average (b and d) normalized wind speed in the CBL case of Mirocha et al. (2014). The top two figures show a horizontal plane at hub height, where the lower two figures show a vertical plane at $y = 0$.

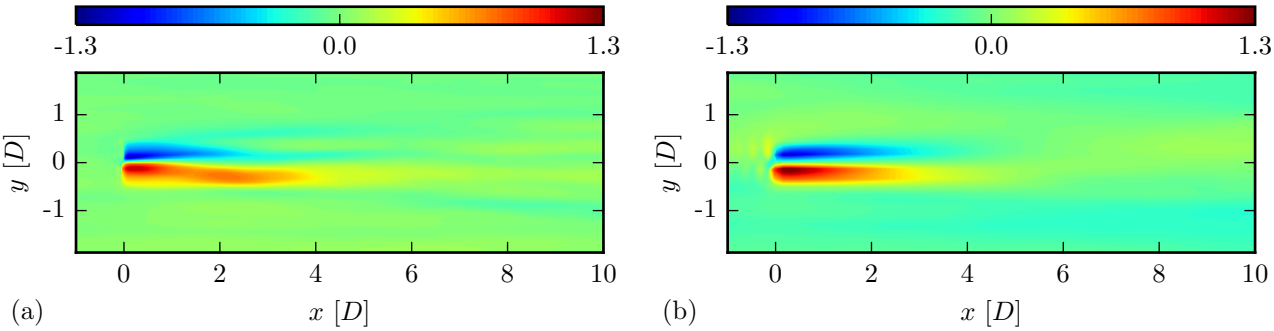

Figure 3.5: 10 min-average vertical wind velocity [m/s] in a horizontal plane at hub height in stable (a) and convective (b) conditions. The torque exerted by the flow on the wind turbine blades leads to a torque in the opposite direction on the flow. As a consequence, a rotational motion is induced in the wake, which causes an updraft of air on one side of the wake centerline and a downdraft on the other side.

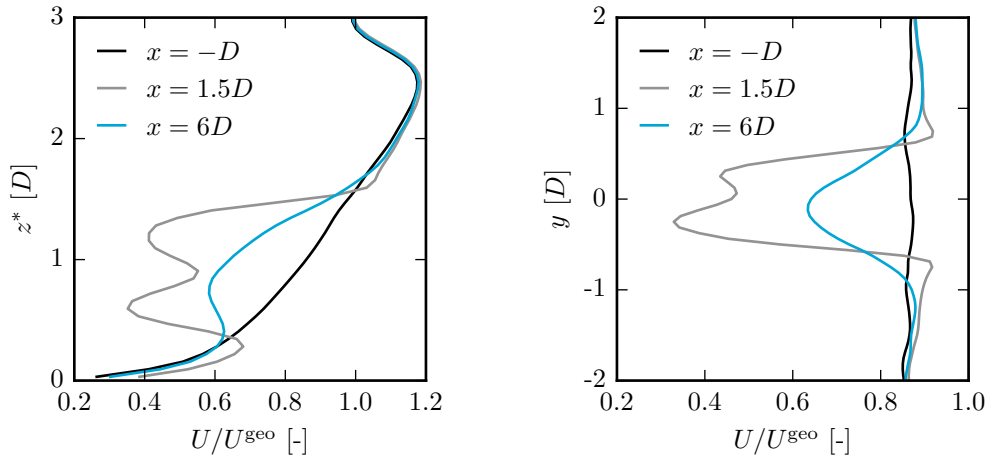

(a) Stable conditions.

(b) Stable conditions.

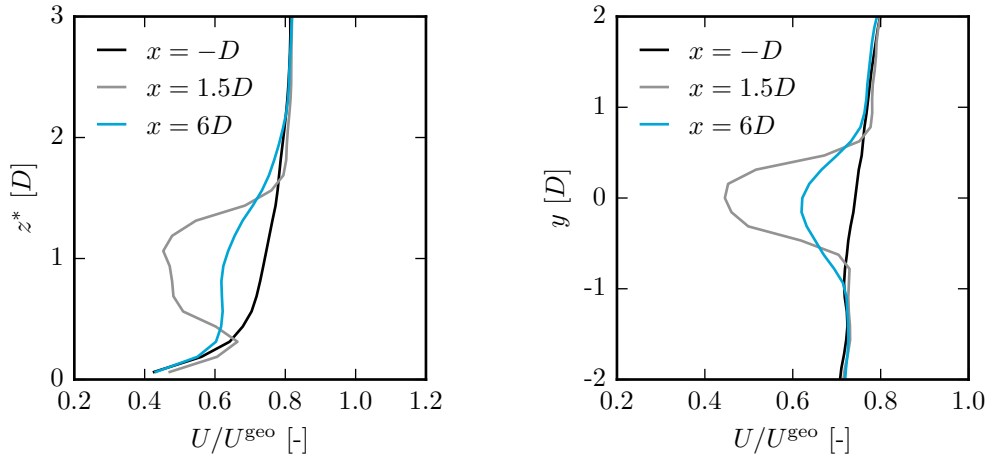

(c) Convective conditions.

(d) Convective conditions.

Figure 3.6: Vertical (a and c) and horizontal (b and d) wind speed profiles upstream of the wind turbine ($x = -D$) and at two locations downstream of the wind turbine ($x = 1.5D$ and $x = 6D$) in stable and convective conditions. In stable conditions, the two separate wakes right behind the turbine merge to form a single wake further downstream. Due to strong turbulent mixing the two separate wakes have already merged at $x = 1.5D$ in convective conditions.

The TKE is then given by (Stull, 1988):

$$\text{TKE} = \tfrac{1}{2}\left(\langle u'u'\rangle + \langle v'v'\rangle + \langle w'w'\rangle\right) \tag{3.2}$$

The TKE in the wake in stable and convective conditions is shown in figure 3.7.

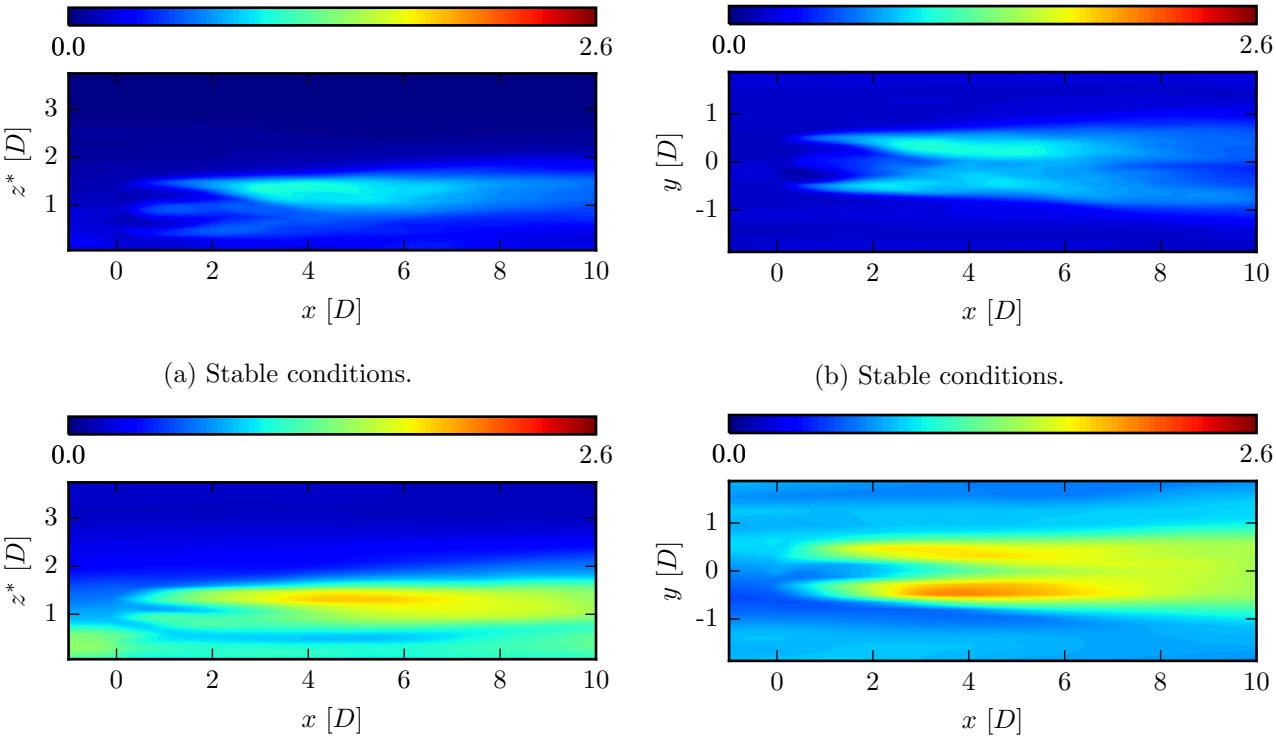

(a) Stable conditions.

(b) Stable conditions.

(c) Convective conditions.

(d) Convective conditions.

Figure 3.7: 10 min-average TKE [m^2/s^2] in a vertical plane at $y = 0$ (a and c) and a horizontal plane at hub height (b and d).

The highest TKE is found at the interface between the undisturbed wind and the wake. Strong velocity gradients in this region lead to considerable production of turbulence by shear. In the vertical direction the TKE shows a clear asymmetry around the wake centerline. At the top of the wake the TKE is significantly higher. As the ambient wind speed is increasing with height, the velocity deficit in the wake is relatively small at lower heights, which leads to less turbulence produced by shear.

The TKE in the wake is about three times higher in convective conditions as compared to stable conditions. Further, comparing figure 3.7b and 3.7d shows that, as expected, the ambient turbulence levels in convective conditions are also considerably higher.

As the TKE is a measure for the energy in the turbulent motions, high values indicate a substantial amount of momentum transport by turbulence. Accordingly, we can confirm the findings of Abkar and Porté-Agel (2015) that convective conditions significantly increase the transport of momentum into to wake, hereby reducing the length of the wake significantly. In contrast, in stable conditions turbulent motions are damped by negative buoyancy, which reduces the turbulent mixing between the high and low momentum flow outside and inside the wake. As a consequence, the wake extends over a large distance.

A more detailed study into the turbulence structure of the wake and the momentum fluxes in the vertical and horizontal direction is part of ongoing research. The contribution of the sub-filter scale TKE is discussed in appendix A.2.

3.2.3. Quantification of wake parameters

In order to make a quantitative comparison to measurements, we need to obtain a measure for the velocity deficit in the wake as a function of distance from the wind turbine. The velocity deficit, VD, is defined as (Vermeer et al., 2003)

$$\mathrm{VD}(x) = \frac{U_\infty - U(x)}{U_\infty}, \tag{3.3}$$

where U_∞ is the free-stream wind speed and $U(x)$ is the wind speed in the wake. Note that the definition of the x_i coordinate frame is still the same as in chapter 2, i.e. the x-direction is perpendicular to the rotor plane, with $x = 0$ located at the hub. Both U_∞ and $U(x)$ in equation (3.3) are not well defined in a (highly) turbulent velocity field. Accordingly, the wake needs to be described in a statistical manner.

Aitken et al. (2014a) developed a framework to estimate statistical properties of wind turbine wakes from scanning LiDAR measurements. They modeled the wake as a Gaussian function subtracted from the ambient flow. Although the wind turbine wake is only approximately axisymmetric in the far wake, the self-similar Gaussian shape of the velocity deficit has been observed in wind tunnel measurements and numerical simulations (Bastankhah and Porté-Agel, 2014). Like Aitken et al. (2014b) and Mirocha et al. (2014) we will use the method of Aitken et al. (2014a) to obtain wake characteristics from LES velocity fields. This method is discussed in detail below.

Near wake

As we have seen in section 3.2.2, the near wake essentially consists of two separated wakes at the mid-section of the blades (grey lines in figure 3.6a and 3.6b). Therefore, Aitken et al. assumed the wake to have a symmetric double Gaussian shape in this region, i.e. the two wind velocity minima are assumed to be equal. This model can, however, not account for the asymmetric wake shape observed before (figure 3.6b). For this reason, we choose to use an asymmetric double Gaussian model instead:

$$\frac{U_\infty - U(x;y)}{U_\infty} = a_l(x) \exp\left[\frac{-(y-y_l)^2}{2\sigma_w^2(x)}\right] + a_r(x) \exp\left[\frac{-(y-y_r)^2}{2\sigma_w^2(x)}\right]. \tag{3.4}$$

In the equation above $U(x;y)$ is the wind speed in the wake at location (x, y). The amplitude of the Gaussian centered at y_l (y_r) is given by a_l (a_r). Both Gaussians are assumed to have the same standard deviation, σ_w. The subscripts l and r refer, respectively, to the wake left and right of the wake centerline.

The wind speed in the wake, U, is obtained directly from the simulations. The free-stream wind speed, U_∞, is taken as the wind speed entering the domain, averaged in the y-direction. Now, y is the only independent parameter in (3.4) and we can obtain the optimal values of a_l, a_r, y_l, y_r and σ_w at each distance x by non-linear regression. Like Aitken et al., the velocity deficit at a distance x is then taken to be equal to the maximum of the fitted function along the y-direction.

Far wake

When moving downstream the two wakes gradually merge to form a single wake that has an approximately Gaussian shape (blue lines in figure 3.6). Like Aitken et al. we therefore assume a single Gaussian model:

$$\frac{U_\infty - U(x;y)}{U_\infty} = a(x) \exp\left[\frac{-y^2}{2\sigma_w^2(x)}\right]. \tag{3.5}$$

This model has two parameters, the amplitude a and the standard deviation σ_w. In the single Gaussian model the velocity deficit can be directly obtained from the amplitude of the Gaussian fit: $\mathrm{VD}(x) = a(x)$.

Time averaging of the LES fields

In a LES, the idealized setup in terms of a uniform geostrophic and surface forcing may lead to more robust correlations in the velocity fields as would occur in nature. Consequently, the estimated wake parameters may be biased (Aitken et al., 2014b). Therefore, the LES velocity fields are averaged in time first. However, in convective conditions even the 10 min-average ambient wind speed shows strong variations over the horizontal domain (black line in figure 3.6d). In order to properly identify the wake and the free-stream wind velocity, we could extend the averaging time. The boundary layer is, however, not in a steady state and long averaging times might influence the results. Hence, we follow Mirocha et al. (2014) and perform the analysis of Aitken et al. (2014a) in a vertical plane instead of a horizontal plane in case of convective conditions. In equation (3.4) and (3.5) every instance of y is now replaced by z. The free-stream velocity, U_∞, becomes a function of height and is taken as the average inflow velocity at each level.

In stable conditions the 10 min-average wind speed is more or less homogeneous in the horizontal direction and performing the wake characterization either in a vertical or a horizontal plane does not significantly affect the results.

Transition region

The point of transition between the near and far wake regions is rather arbitrary and depends on the ambient turbulence level (Sanderse, 2009). Aitken et al. determined the simplest model to fit the data by a sum of squares F-test. In case of a p value below 0.05 the single Gaussian model was rejected and instead the double Gaussian model was fitted.

Unlike Aitken et al., who considered numerous LiDAR scans, we only have one sample, i.e. the time-averaged LES fields. Hence, we can easily identify the transition region and choose where to fit the single and the double Gaussian model. In the transition region itself both models deliver a rather poor fit and we choose to linearly interpolate the velocity deficit between the last data point of the near wake and the first data point of the far wake. In case of stable conditions this resulted in interpolation from $2D$ to $3D$. In convective conditions the double wake structure dissipates rapidly and thus we directly fit the single Gaussian model.

Results

Figure 3.8 shows a comparison between the measurements reported by Aitken et al. (2014b) and Mirocha et al. (2014) and simulation results of DALES. In both cases the LES results fall within the uncertainty of the measurements. The results confirm the conclusions drawn at the end of section 3.2.2 in a quantitative way. Convective conditions clearly show a decrease in the extent of the wake. It must be noted that we considered weakly stable and convective cases in this study. The differences in the rate of wake recovery can be expected to be even more profound in moderately or strongly convective/stable conditions.

Next, we will consider the third observational study. Käsler et al. (2010) did not present a detailed analysis of their LiDAR measurement data. We believe the velocity deficit in their analysis is obtained by looking at the measured wind speed on a line parallel to the wind direction behind the wind turbine. Of course, the method of Aitken et al. (2014a) does essentially the same, i.e. estimating the velocity deficit in the wake, but in a more generic and systematic manner. In absence of further details given by Käsler et al., we therefore choose to again fit either a double or a single Gaussian model, given by equation (3.4) and (3.5), to the time-averaged LES fields. From this, the velocity deficit was determined as a function of the downstream distance from the turbine, which could then be compared to the measurement data, see figure 3.9. The LES results show a good agreement with the observations over the whole measurement range.

In figure 3.8 and 3.9, the maximum velocity deficit in the wake is located at around $1D$ behind the wind turbine in convective conditions and at about $2D$ in stable conditions. Instead, one might expect to find the maximum deficit in the rotor plane ($x = 0$) where the kinetic energy is extracted. Ainslie (1988) attribute this effect to the complex flow structure in the near wake region, which is dominated by the relaxation of pressure gradients in the axial and radial direction. Further, Ainslie estimate the maximum deficit to occur at 1 to $2D$. In case of

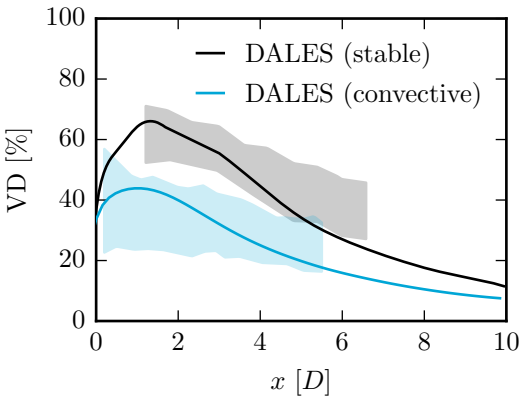

Figure 3.8: Velocity deficit in the wake of a 2 MW wind turbine as simulated by DALES, in stable (black) and convective (blue) conditions. The shaded areas indicate one standard deviation around the mean of the LiDAR measurements of Mirocha et al. (2014) and Aitken et al. (2014b).

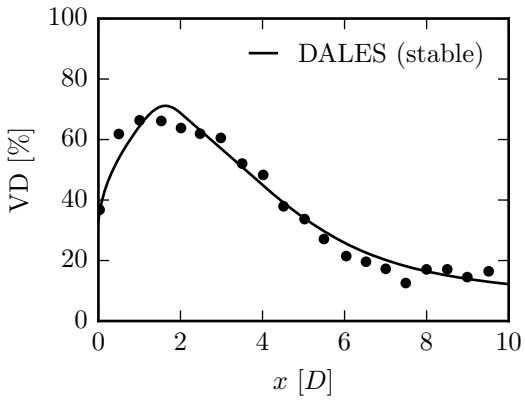

Figure 3.9: Simulated velocity deficit in the wake of a 5 MW wind turbine in stable conditions. The dots indicate the velocity deficit as measured by Käsler et al. (2010).

low ambient turbulence levels, e.g. in stable conditions, the near wake structure is maintained over a longer distance and thus the maximum wind speed deficit is attained farther downstream of the rotor (Sanderse, 2009).

Also, the TKE in the wake is strongly increasing over the first 1 to $3D$ behind the wind turbine (figure 3.7). Consequently, the fact that the maximum velocity deficit is found behind the wind turbine might also be related to the production of TKE, which comes at the cost of the kinetic energy in the mean wind (MKE). Ongoing research on the budgets of both the TKE and the MKE might reveal the dominant mechanisms that establish the velocity deficit in the near wake.

3.3. Wind farm wake effects

The results of the previous section show that our model can correctly represent the wake of a single wind turbine. The most important application of our model is, however, the simulation of wind farms. In order to get an idea of how well DALES can represent wind farm wake losses, we studied the North Hoyle offshore wind farm. This particular wind farm was select for two reasons. First, the characteristics of the installed wind turbines (Vestas V80) are available (Wu and Porté-Agel, 2015). Secondly, wake-related power deficits in this wind farm were already analyzed in detail by Alblas (2012).

3.3.1. Case description

Atmospheric stability

The large impact of atmospheric stability on wake evolution requires a classification of the stability conditions before we can compare the results of measurements and simulations. In the relevant literature (see Alblas (2012) for an overview), this stability classification is often based on the Obukhov length. The Obukhov length, L, can be interpreted as proportional to the height above the surface where buoyancy effects are first dominant over mechanical production of turbulence and is defined as (Stull, 1988)

$$L = -\frac{\overline{\theta_v} u_*^3}{\kappa g \overline{w'\theta_v'}}. \tag{3.6}$$

In the expression above θ_v is the virtual potential temperature, u_* the friction velocity, κ the von Karmann constant, g the gravitational acceleration and $\overline{w'\theta'_v}$ the vertical heat flux. All quantities in (3.6) are evaluated at the surface.

Alblas sampled the available data in several stability classes, of which we will consider convective ($-200\,\mathrm{m} < L < 0\,\mathrm{m}$) and neutral ($|L| > 1000\,\mathrm{m}$) conditions. Unfortunately, the computational resources were not available at the time to simulate the wind farm on a sufficiently high resolution in stable conditions.

Of course, we cannot reproduce the ensemble of conditions thats is contained within each stability class. Therefore, we choose to only run a single case for each stability condition, that falls approximately in the center of the bin. This way we can at least make a qualitative comparison between DALES and the production data.

The convective LES case was based on the W06 case of Sullivan et al. (1998), where a surface heat flux of $100\,\mathrm{W/m^2}$ was prescribed. Neutral conditions were again represented by the REF case of Allaerts and Meyers (2015), which was also used in section 2.4 and 2.5. In both cases a typical offshore roughness length of $2 \times 10^{-4}\,\mathrm{m}$ was set.

Wind speed and direction

Besides stability, Alblas sampled the data in terms of wind speed and wind direction. A geostrophic wind speed of 8.5 m/s in neutral conditions, and 9.5 m/s in convective conditions, was prescribed to arrive at a hub height wind speed within the range ($8 \pm 0.5\,\mathrm{m/s}$) that was selected by Alblas.

Located only about 7.5 km from the coast in the Liverpool Bay, the conditions at the North Hoyle offshore wind farm are certainly affected by the land in a range of wind directions. Taking this into account is beyond the scope of the current work. Still, we will consider two different wind direction to study the effect of the layout (relative to the wind direction) on the power deficits in the wind farm. More specifically, we look at the northern ($348.9 \pm 2.5°$) and western wind direction ($258.8 \pm 2.5°$) in the study of Alblas. Figure 3.10b shows the layout of the North Hoyle offshore wind farm with respect to these wind directions.

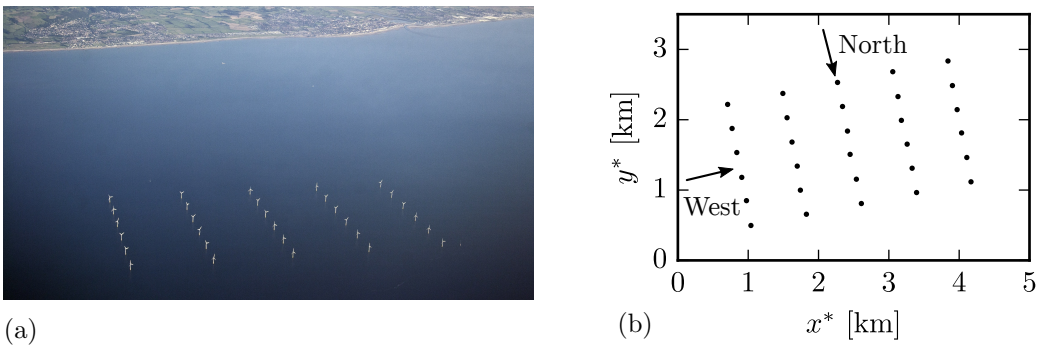

(a) (b)

Figure 3.10: Aerial photograph (a) and schematic layout (b) of the North Hoyle wind farm off the coast of Wales, consisting of thirty Vestas V80 2 MW wind turbines. The downstream spacing between the wind turbines is $4.4D$ ($10D$) in case of a northern (western) wind direction. Photograph by Tom Jeffs.

Domain and grid size

The North Hoyle wind farm covers an area of about $10\,\mathrm{km^2}$. Additionally, a region around the wind farm is required to prescribe the boundary conditions. Therefore, a horizontal domain of $5\,\mathrm{km} \times 3.5\,\mathrm{km}$ was specified, with a grid spacing of 12.5 m. The domain height was set to 1 km in neutral conditions and 2 km in convective condition. A vertical grid spacing of 10 m was selected to cover the rotor disks by a sufficient amount of grid points. To reduce computational costs, the vertical grid size above the wind farm was gradually increased to 20 m in the convective case.

3.3.2. Wake characteristics

Again we will first consider the results in a qualitative manner. Figure 3.11 shows the 1 min-average wind speed at hub height for a west wind in neutral and convective conditions. As expected we find a shorter wake extent in convective conditions. Furthermore, turbulence in the ambient wind field leads to short time-scale wind direction variations around and behind the wind turbines. As the wake follows the local wind direction, for a stationary observer it seems as if the wake meanders around the centerline (Ainslie, 1988). Consequently, the average centerline velocity deficit is smaller as one would expect for a stationary wake. The wake can even move as far in the transversal direction that it does not interfere with the downstream wind turbine at all (figure 3.11, Larsen et al., 2008). Stronger turbulence in convective conditions leads to increased wake meandering (figure 3.11b) and we can expect a smaller power deficit due to wake effects.

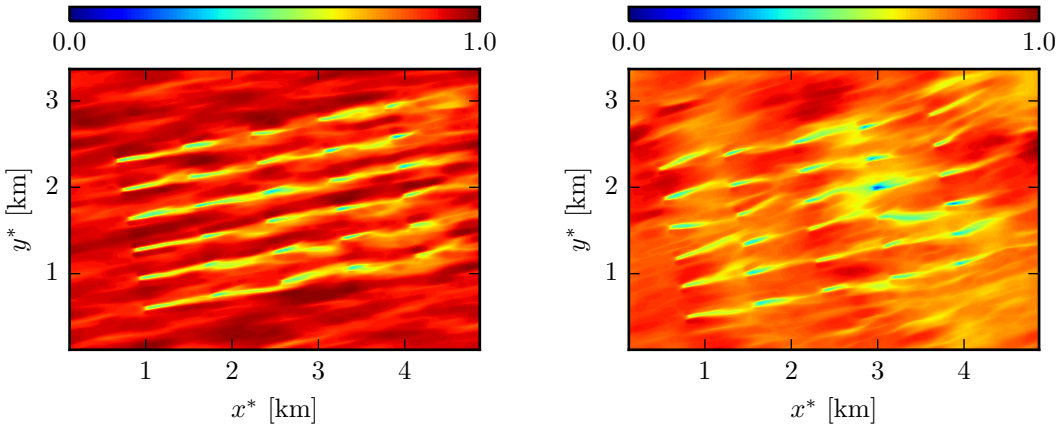

(a) Neutral conditions.

(b) Convective conditions.

Figure 3.11: Normalized wind speed at hub height in the North Hoyle offshore wind farm in case of a west wind. The wind speed is averaged in time over one minute.

3.3.3. Quantification of wind farm wake effects

Power deficit along a row

Wake effects in wind farms are often quantified by studying the power along a row of wind turbines parallel to a certain wind direction, relative to the power of the upstream wind turbine (Alblas, 2012, Barthelmie et al., 2013, 2010, Méchali et al., 2006). We indicate the row numbers by n, where $n \in \{1, 2, \ldots, N_{\text{row}}\}$. In our definition, $n = 1$ is taken to be the most upwind turbine along the wind direction under consideration. The total number of turbines in a row, N_{row}, depends on the wind direction and the layout of the wind farm.

The simulated power relative to the upwind row, for both wind directions and stability conditions, is shown in figure 3.12. Production data of the North Hoyle wind farm is also plotted.

The main characteristics of the power deficit are well represented by our model. In general, a large power drop is observed from the first to the second turbine. While moving further downstream, the power decreases only slightly and eventually becomes constant.As the wakes behind the first row of turbines expand, they first hit the ground surface. Typically after three or four rows the wakes merge with neighboring wakes in the lateral direction (Barthelmie et al., 2010). From hereon, the wakes can only recover by mixing with higher momentum air from above the wind farm. At this point, a balance is established between extraction of momentum by the wind turbines and entrainment of momentum from above (Méchali et al., 2006). Consequently, the wind turbine power does not further decrease while moving downstream.

The production data for the northern wind direction, as well as the simulation results for the

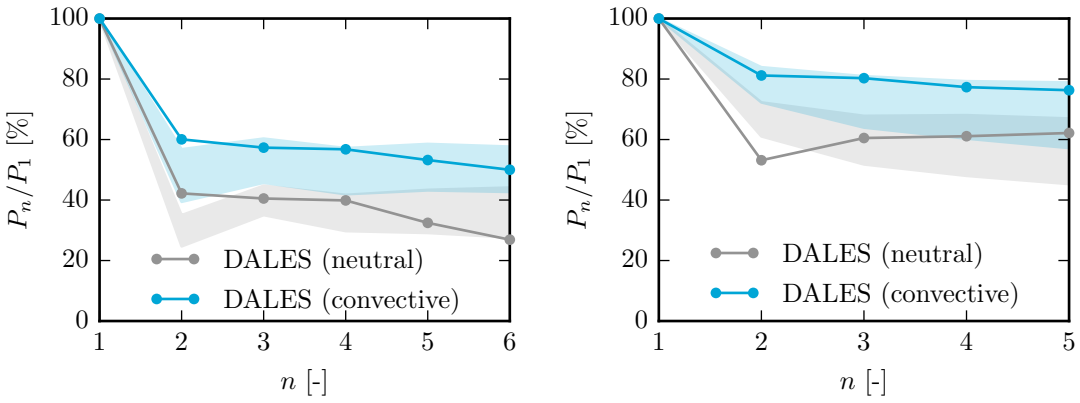

(a) North wind.

(b) West wind.

Figure 3.12: Average wind turbine power relative to the most upwind row in convective (blue) and neutral (grey) conditions. DALES (points) is compared with wind farm power production data of the North Hoyle wind farm (shaded areas). The shaded areas indicate one standard deviation around the mean, i.e. half a standard deviation above and below the mean. The production data was analyzed by Alblas (2012).

western wind direction in neutral conditions, deviate from this trend. The power clearly shows a minimum at the second row of turbines. This phenomenon was also observed in production data (Méchali et al., 2006) and simulations (Wu and Porté-Agel, 2015) of the Horns Rev wind farm when a narrow (± 1 to $3°$) wind sector was considered. Wu and Porté-Agel indicate that this effect may be caused by the turbulence generated by the first row of wind turbines, which enhances the recovery of the wakes behind the second row of wind turbines.

Moreover, the simulated power for the western wind direction in neutral conditions increases towards the end of the row. This was also observed by Méchali et al. (2006) in the Horns Rev wind farm in certain conditions.

As expected, the power deficit is smaller in convective conditions. Secondly, due to the smaller spacing of the wind turbines in the northern direction ($4.4D$ instead of $10D$), a significantly higher power deficit is observed.

We can conclude from a range of observational studies of wind farms (Alblas, 2012, Barthelmie et al., 2013, 2010, Hansen et al., 2012, Méchali et al., 2006) that the quantification of wake effects is strongly dependent on the conditional sampling that is applied in terms of the wind direction (sector) and stability conditions. Additionally, the large number of atmospheric conditions that is contained in a sample leads to large standard deviations. Reproduction of this wide range of conditions with LES is difficult, if not impossible. For further validation of our model it might therefore be better to take a different approach. Based on meteorological and reanalysis data, a case can be setup which represents the atmospheric conditions around a wind farm to a good degree for a time period of several hours. The simulated power over this period can then be compared with production data. By performing this analysis for several different cases, we can test the validity of our modeling framework in a more direct and potentially better way.

Wind farm efficiency

Even though a lot of valuable information is contained in the structure of the wakes inside a wind farm, in the end the accumulated power production is the most important quantity. To remove a potential bias due to differences in the average free-stream wind speed, we first compare the performance of the wind farm as a whole in terms of the wind farm efficiency, η.

Like Barthelmie et al. (2013), we define the wind farm efficiency as

$$\eta = \frac{1}{N} \sum_{n=1}^{N} \frac{P_n}{P_1}, \tag{3.7}$$

where P_n $(n = 1, 2, \ldots, N)$ is the power production of wind turbine n in the wind farm. The wind farm efficiency gives a measure of the average power output of the N turbines in a wind farm, compared with the power output of a free-stream wind turbine, P_1. For this reason Creech et al. (2015) refer to the same quantity as the relative wind farm performance. In this definition $\eta = 100\,\%$ in case wake effects do not play a role, and it decreases when the wake effects become stronger.

Figure 3.13a shows the efficiency of the North Hoyle wind farm over the course of about 3 h for both wind directions and stability conditions. Apart from the differences in average efficiency that could be expected from the results in the previous section, convective conditions show large fluctuations due to strong turbulence in the ambient flow.

At first glance, the high wind farm efficiency in figure 3.13a suggests that convective conditions can be related to higher than average wind farm power. Indeed, this would be the case if convective turbulence would only affect wake recovery. However, in the first part of this chapter we have seen that, for a given geostrophic wind, the mean power in the wind is also significantly lower in convective conditions. To include this effect in our analysis, we can consider the geostrophic efficiency, η^{geo}, of the wind farm:

$$\eta^{\mathrm{geo}} = \frac{1}{N} \sum_{n=1}^{N} \frac{P_n}{\frac{1}{2}\rho A {U^{\mathrm{geo}}}^3}. \tag{3.8}$$

The geostrophic efficiency gives a measure for average wind turbine power in the farm, relative to the power in the geostrophic wind.

In figure 3.13b, η^{geo} is plotted over the same time period as η in figure 3.13a. Note that the scale of the η-axis is different in the second figure. The difference between convective and neutral conditions for a given wind direction is significantly smaller. Increased wake recovery in convective conditions still leads to a higher power output, but the lower power in the wind at hub height counteracts this effect to a considerable degree. As η^{geo} keeps increasing over the course of the simulation, the boundary layers are also clearly not in a steady state.

In conclusion, convective turbulence essentially triggers two competing mechanisms: the extent of the wakes is decreased, but at the same time the power in the wind is too. Ultimately, the dominant mechanism will depend on the exact stability conditions, the wind speed and the wind direction relative to the wind farm. Currently, LES is the only tool that can come close to accurate representation of all these contributions given a large-scale weather forecast. Although further validation of our model is still a priority, the results shown in this chapter give confidence to use our model for the study of a new case: wake evolution in the stratocumulus-topped boundary layer.

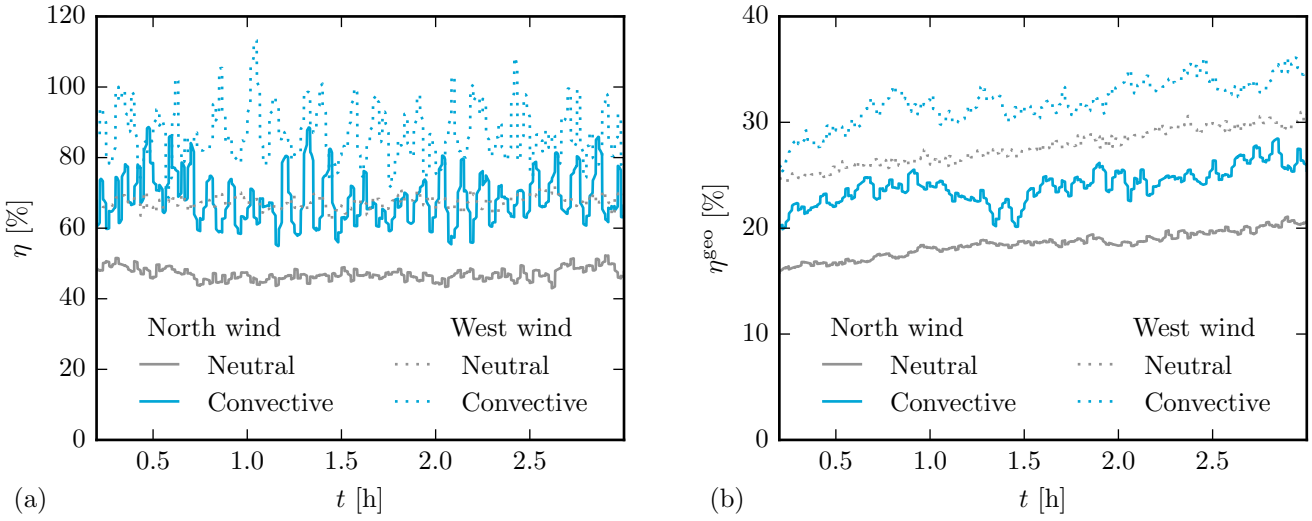

Figure 3.13: Time evolution of the efficiency (a) and geostrophic efficiency (b) of the North Hoyle offshore wind farm for two different wind directions and stability conditions as simulated by DALES.

4

The impact of stratocumulus on wind farm performance

4.1. Introduction

While the annual average stratocumulus cloud cover over the North Sea is already about 20 to 30 %, it exceeds 40 % and can be as high as 60 % over the subtropical eastern oceans (Wood, 2012). Stratocumulus clouds reflect a large part of the down-welling solar radiation. Also, they are often sufficiently thick ($\gtrsim 100$ m) that long-wave (LW) radiation is emitted as a black body just like the underlying ocean surface (Duynkerke et al., 2004). Due to their radiative properties, stratocumulus clouds have a distinct effect on the turbulence structure of the ABL, that shows a marked diurnal cycle. For this reason, we can expect stratocumulus to have a considerable effect on wake evolution. Nonetheless, their impact on offshore wind farm performance has not been studied up to now.

At night, when the cloud is not warmed by solar radiation, LW radiative cooling from the top of the cloud generates convective turbulence and a positive buoyancy flux throughout the ABL (Driedonks and Duynkerke, 1989). In contrast to the dry ABL, turbulence in the sub-cloud layer of a stratocumulus-topped boundary layer (STBL) is also driven from above. Accordingly, turbulent mixing by convective motions is enhanced compared to what could be expected from considering only the surface buoyancy flux. In the previous chapter we found that convective turbulence can strongly reduce the extent of wind turbine wakes and thus increase wind farm efficiency.

During the day absorption of solar radiation compensates the effect of LW radiative cooling and the cloud layer starts to warm. This can cause the cloud layer to become stably stratified with respect to the sub-cloud layer and more or less neutral stability conditions are observed. The wake extent is thus expected to be significantly longer than during the night, leading to a lower efficiency of the wind farm.

The effect of stratocumulus on turbulence in the ABL, along with the fact that DALES has been shown to accurately represent the turbulence structure of the STBL (Duynkerke et al., 1999, 2004, Stevens et al., 2005), make it an excellent test case to fully demonstrate the capabilities of our model.

4.2. Case description

For the study of the effect of stratocumulus on wind farm performance we selected the European Cloud Systems (EUROCS) stratocumulus case, described in full detail by Duynkerke et al. (2004). This particular case was part of an intercomparison study of LES codes in which DALES was also a participating model. It provides a well-defined modeling scenario based on observations, that has been used in other studies as well (Ackerman et al., 2004, de Roode and Los, 2008).

Since the EUROCS case considers a full diurnal cycle, we can conduct a similar study as Abkar et al. (2015) performed for the diurnal cycle of a clear boundary layer. By looking at the wake evolution and wind power production as a function of time, we can learn if, and to what extent, the diurnal cycle of a STBL is of importance for wind power forecasts.

In addition, a second, reference case was set up which was initialized with a lower amount of moist to prevent cloud formation. By comparison of this case and the EUROCS case, we can explicitly study the effect of turbulence induced by stratocumulus. In the EUROCS case a fixed sea surface temperature (SST) is set, and the surface buoyancy flux, $\overline{w'\theta_v'}\big|_{\text{sfc}}$, is calculated by DALES from Monin-Obukhov similarity theory. The time series of the simulated surface buoyancy flux is then used as a surface boundary condition in the case without cloud formation to prevent a bias related to the surface forcing.

Once more, the Vestas V80 2 MW wind turbine (D = 80 m, 70 m hub height) was implemented based on the description of Wu and Porté-Agel (2015). To ensure that the wind turbines operate above cut-in wind speed even in full-wake conditions, the geostrophic wind speed of the original EUROCS case was increased from 6 m/s to 8 m/s.

Due to limited computational resources at that time, Duynkerke et al. used a grid size of 50 m × 50 m × 10 m on a domain of 2.5 km × 2.5 km × 1.2 km. For the simulations with a single turbine (section 4.3.2) the same domain size was set, but with a resolution of 12.5 m × 12.5 m × 10 m to meet the criterion of Wu and Porté-Agel (2013) mentioned in section 3.2.1. For the multiple turbine simulation (section 4.3.3) the stream-wise domain size was increased to 4 km. Furthermore, to reduce computational cost, the horizontal resolution was reduced to 15 m. This is, again according to the criterion of Wu and Porté-Agel, still enough for proper representation of the wind turbine.

4.3. Simulation results and discussion

Before looking in detail at the wind turbine-related results, we will consider the time evolution of several key variables.

4.3.1. Time evolution of the boundary layer

The distinct diurnal cycle of the turbulence structure of the STBL is best represented by the buoyancy flux, see figure 4.1a. At night, radiative cooling at the cloud top leads to turbulent mixing throughout the boundary layer. Further, latent heat release supports a positive buoyancy flux in the cloud layer. The buoyancy flux profile of the case without cloud formation resembles a shallow mixed layer, which could be expected from the positive surface buoyancy flux at this time (figure 4.2b). However, the conditions are only weakly convective and turbulence production in the cloud layer is far dominant. Consequently, significantly higher turbulence levels in the vertical direction are observed at night in case of stratocumulus, as compared to the clear case (figure 4.1b).

During the day, absorption of solar radiation leads to warming of the cloud and a significant reduction of the buoyancy flux. The slightly negative buoyancy flux in the middle of the boundary layer strongly damps vertical turbulent motions. Moreover, turbulence generated at the surface cannot reach the cloud layer and the sub-cloud layer becomes decoupled from the cloud layer. Accordingly, the buoyancy flux (figure 4.1a) and vertical velocity variance (figure 4.1b) in the sub-cloud layer are about the same during the day whether stratocumulus clouds are present or not.

Additionally, stable stratification of the cloud layer with respect to the sub-cloud layer strongly reduces the transport of heat and moisture from the surface into the cloud. Together with the entrainment of warm and dry air from above the cloud layer, this causes the cloud layer to thin (Van der Dussen et al., 2014), as indicated by a decreasing liquid water path (LWP) in figure 4.2a. The LWP gives a measure for the total amount of liquid water in a vertical column,

$$\text{LWP} = \int_0^{z_{\max}} \rho q_l \, \mathrm{d}z, \tag{4.1}$$

with q_l the liquid water specific humidity, and is a key quantity for radiative transfer in the

ABL. The thinning of the cloud is, however, not sufficient to break up the cloud and a 100 % cloud cover is maintained over the entire diurnal cycle.

It is interesting to note that in the STBL, the intensity of the vertical turbulent motions shows a minimum during the day (figure 4.1b). The opposite is true in the diurnal cycle of a clear boundary layer (Abkar et al., 2015). Heating of the ground surface by solar radiation during the day causes the rise of convective thermals. Consequently, the turbulence intensity starts to increase at sun rise and has its maximum in the afternoon.

As turbulence transports momentum in the vertical direction, the wind velocity profile is affected by turbulence too. Accordingly, the wind speed and direction also show a diurnal cycle. In a clear ABL, the wind speed at and above hub height is typically lower in convective conditions (daytime) than in stable conditions (night-time). Stratocumulus changes the time evolution of the wind speed, as shown in figure 4.1c. While the hub height wind speed (figure 4.2c) is around 90 % of the geostrophic value during most of the diurnal cycle, the wind speed starts to increase around 14:00 to show a supergeostrophic maximum at the end of the afternoon. In analogy with the low-level jet in the nocturnal boundary layer over land, the occurrence of supergeostrophic wind speeds in the STBL is most likely related to the collapse of turbulence during the day. The supergeostrophic wind speeds were also found in the results of other LES models submitted for the EUROCS intercomparison study.

Finally, in contrast to the clear CBL, strong convective turbulence in the STBL at night does not lead to relatively low (hub height) wind speeds in the boundary layer. Where turbulence in a dry CBL is driven by a buoyancy flux from the surface, turbulence in the STBL is mainly generated in the cloud layer. Consequently, momentum that is entrained from above the STBL is mixed throughout the boundary layer, leading to higher wind speeds as one would normally expect in convective conditions.

4.3.2. Wake evolution behind a single wind turbine

Like in chapter 3, we first examine wake evolution behind a single wind turbine, after which we continue with the wake effects in a wind farm.

For analysis of the wake structure, two periods of one hour in the diurnal cycle were selected in which we expect the most significant differences: 11:00-12:00 (daytime) and 23:00-24:00 (night-time). Evolution of the wake is again quantified by fitting a Gaussian model to the velocity deficit, as described in section 3.2.3. The average velocity deficit as a function of distance from the wind turbine, for the two one-hour periods that were selected, is given in figure 4.3.

In case of stratocumulus, the difference between day and night is striking. At night, convective turbulence generated by LW radiative cooling from the cloud top significantly decreases the velocity deficit in the wake. During the day the sub-cloud layer is decoupled from the cloud layer and turbulence is mainly produced at the surface. As the surface forcing is the same in both cases, the velocity deficit in the wake follows almost exactly the same profile. Even though a strong radiative forcing is absent, the clear case does show slightly increased wake recovery at night as a result of the positive surface buoyancy flux.

4.3.3. Wind farm performance

The analysis in the previous sections shows that the velocity deficit in the wake varies in time and between the cloudy and clear case. The wake-related power deficit is proportional to the wind velocity deficit to the power three, so any variations in wind speed are expected to result in strong power variations. For this reason, we will also consider a multiple wind turbine simulation in full-wake conditions.

Setup of the simulation

To eliminate the effect of wind direction changes ($\sim 10^\circ$ over the diurnal cycle, figure 4.2d) from the analysis, we continuously align the wind farm to the prevailing mean wind direction. See appendix C for details about this procedure. First, the impact of enhanced wake recovery is isolated by considering the wind farm efficiency, as defined in section 3.3.3. Then, the

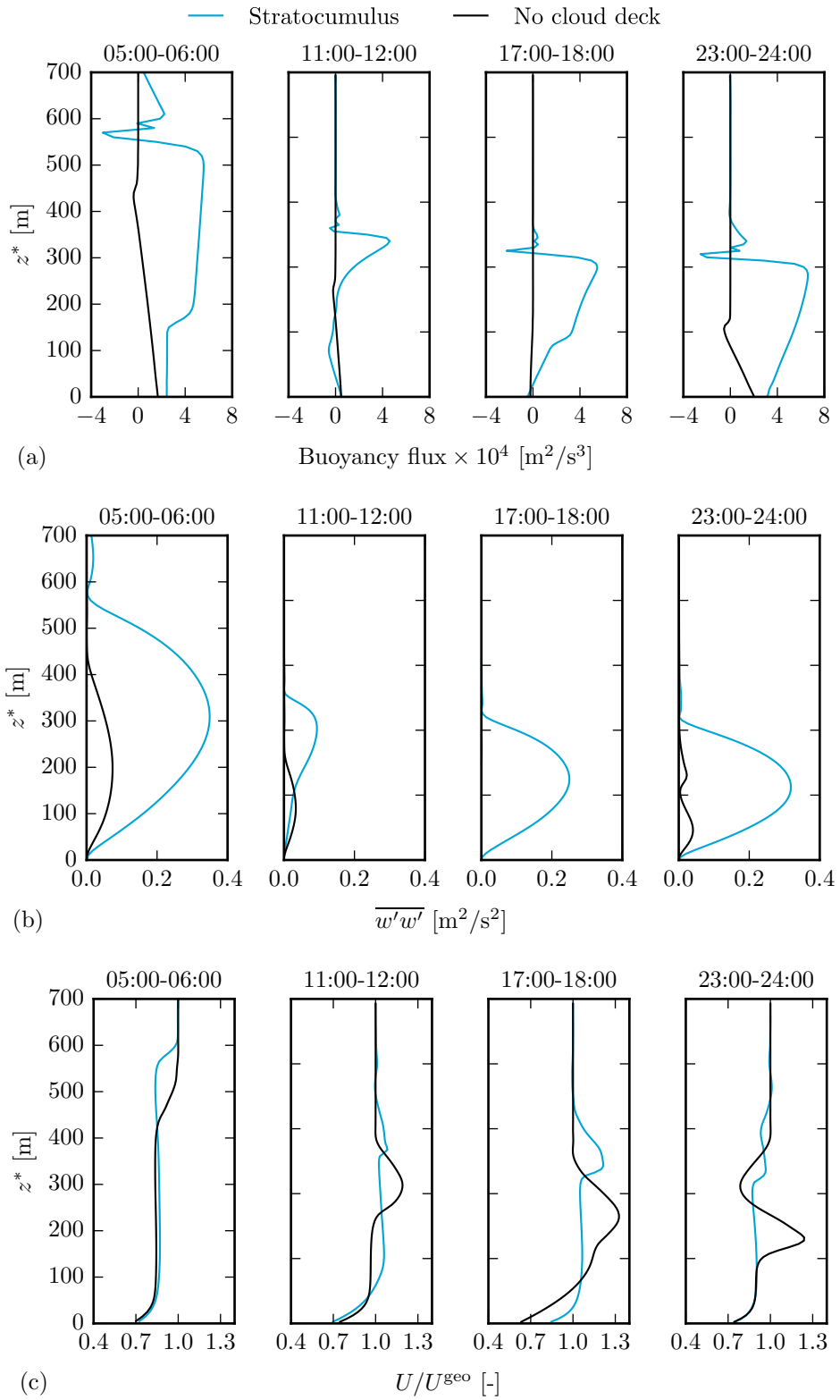

Figure 4.1: Vertical profile of the buoyancy flux (a), vertical velocity variance (b) and wind speed (c), averaged over four one-hour time periods during the diurnal cycle of the EUROCS stratocumulus case (blue) and a case with the same surface buoyancy flux but without clouds (black).

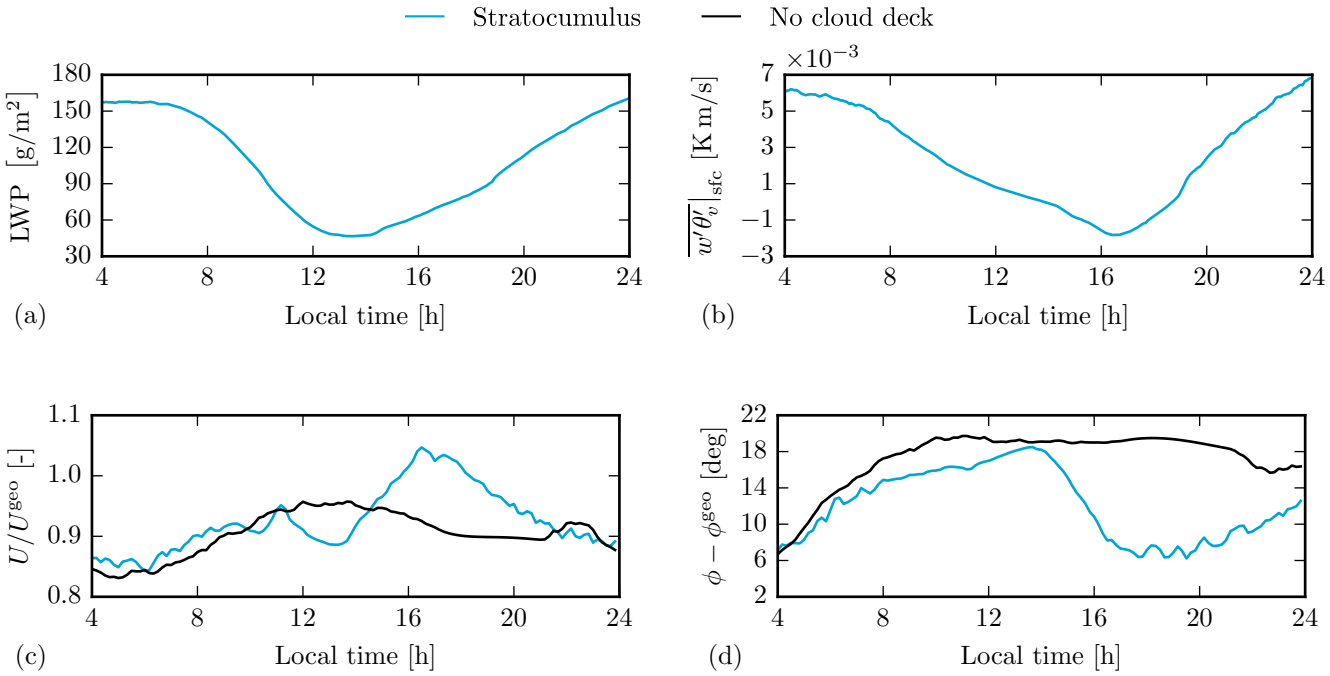

Figure 4.2: Time evolution of the liquid water path (a), surface buoyancy flux (b) and the wind speed (c) and wind direction (d) at hub height in the EUROCS stratocumulus case (blue) and a similar case without cloud formation (black).

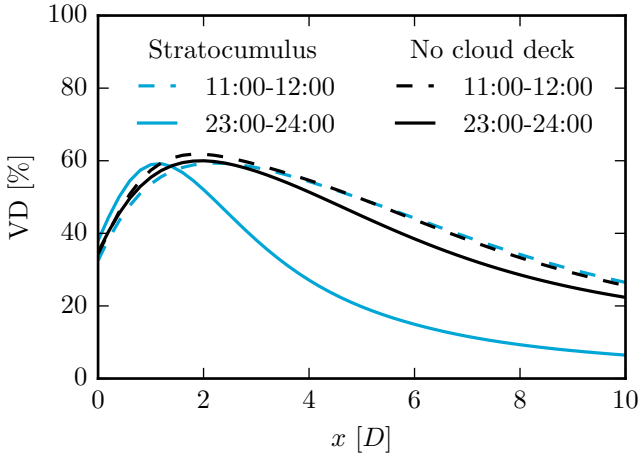

Figure 4.3: Velocity deficit in the wake as a function of distance from the wind turbine. At night the wind speed in the wake recovers significantly faster under a stratocumulus cloud deck (solid blue line) than during the day (dashed blue line) or in case there is no cloud deck (black lines).

combined effect of turbulence generated in the cloud layer on wind speed and wake recovery will be studied by again considering the geostrophic wind farm efficiency.

Due to limited computational resources, we will only consider a single row of wind turbines, spaced $7D$ apart in the stream-wise direction. The error associated with neglecting the interaction between wind turbines in the span-wise direction is small if the wind sector around the row of wind turbines is smaller than about $\pm 15°$ (Ivanell, 2009). Since we actively control the wind direction relative to the wind turbine row, the wind sector is much smaller than $15°$ during the entire simulation.

Results

The power of each wind turbine in the row, relative to the most upwind wind turbine, is given in figure 4.4.

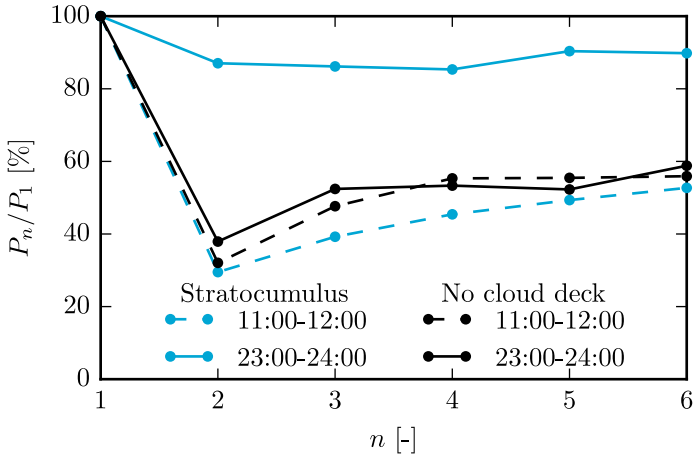

Figure 4.4: Power relative to the most upwind wind turbine for a single row of wind turbines. Two one-hour periods in the diurnal cycle are compared for which the differences are most significant.

Again, the difference between the stratocumulus case at night and during the day is profound. Where at night the power deficit is only around 10 %, during the day it is as high as 40 to 60 %. The previously mentioned study of Abkar et al. (2015) considered a wind farm consisting of the same wind turbines, also with a stream-wise spacing of $7D$. Relating the power deficits in figure 4.4 to their results, we find that the results in case of stratocumulus are almost exactly opposite. In the clear boundary layer of Abkar et al., the power deficit along a row of wind turbines is 20 to 30 % at midday (12:00-13:00) and about 50 % in the early morning (04:00-05:00).

Since we continuously align the row of wind turbines to the prevailing mean wind direction, we essentially consider a narrow wind sector. As discussed in section 3.3.3, in this case it is often found that the second wind turbine has the largest power deficit, and the power increases while moving down the row (Méchali et al., 2006, Wu and Porté-Agel, 2015).

The overall efficiency of the row of wind turbines is shown in figure 4.5a, along with the geostrophic efficiency in figure 4.5b.

In the STBL, both the efficiency and the geostrophic efficiency are significantly higher at night. In contrast to clear convective conditions, increased mixing by convective turbulence generated in the cloud layer does not come at the cost of a lower hub height wind speed (section 4.3.1). Only during the afternoon, the slightly lower wind speed in the STBL leads to a lower geostrophic efficiency at approximately the same wind farm efficiency.

Again we can make a comparison to the clear boundary layer study of Abkar et al. (2015). In that case, the wind farm efficiency peaks at midday and has a minimum around 21:00.

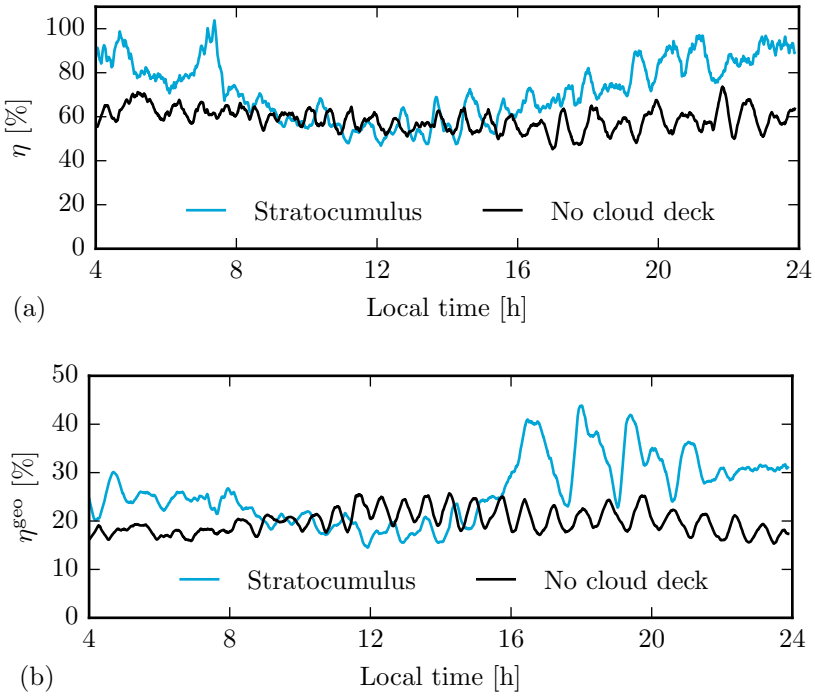

Figure 4.5: Efficiency (a) and geostrophic efficiency (b) of a row of 6 wind turbines in full-wake conditions, during the diurnal cycle of a stratocumulus-topped boundary layer and for a case with the same surface forcing but without clouds.

Oppositely, in the STBL the minimum efficiency is observed at midday and the maximum efficiency during the night.

Further, large fluctuations in the geostrophic wind farm efficiency are observed from about 16:00 to 20:00. The fluctuations around this time are much less profound for the wind farm efficiency, where the effect of changes in the hub height wind speed are filtered out. This is an indication that the fluctuations are, at least partly, caused by changes in the (hub height) wind velocity. At hub height, the mean wind speed shows an increase from about 90 % to 105 % of the geostrophic wind between 14:00 and 17:00 (figure 4.2c). Additionally, the mean wind direction changes by 10° over the same 3 h period (figure 4.2d). Near the surface, turbulence in the horizontal direction is enhanced, leading to variations in the wind speed over the domain. As the wind power scales with the wind speed cubed, these variations can possibly have a significant effect on the geostrophic wind farm efficiency.

To conclude, we find that wake evolution is strongly influenced by convective turbulence that is produced as a result of the radiative properties of stratocumulus clouds. The fact that decreased wake extent due to strong convective turbulence at night does not coincide with lower hub height wind speeds leads to a significant increase in the geostrophic wind farm efficiency as compared to clear conditions. The distinct impact of stratocumulus we find in this idealized case study gives confidence that a similar effect will be observed in real world wind farms. Further research with our model and analysis of production data should prove if this is indeed the case.

5

The Horns Rev photo case

5.1. Introduction

Apart from being a beautiful sight and a rare phenomenon, the wind turbine-induced cloud formation observed at the Horns Rev wind farm on February 12, 2008 (figure 5.1), has led to quite some debate on the nature of its occurrence in (popular) scientific publications (Emeis, 2010, Hasager et al., 2013, Stevens, 2012). This rather unique interaction between wind turbine dynamics, boundary-layer turbulence and cloud thermodynamics makes the cloud formation at Horns Rev an interesting test case to further explore the capabilities of our modeling framework.

Figure 5.1: Photograph of the Horns Rev 1 offshore wind farm on February 12, 2008, taken from the south around 10:10 UTC. Photograph by Christian Steiness.

Based on a detailed study of the meteorological conditions around the time of the photograph, Hasager et al. (2013) came to the conclusion that the wake clouds are formed as a consequence of cooling of air parcels in updrafts in the wake. In reaction to the torque exerted by the flow on the wind turbine blades, the wake starts rotating in the opposite direction as the rotor. The updraft on one side of the wind turbine can lift an air parcel several tens of meters. As the pressure decreases with height, the air parcel expands and its temperature decreases. Since the saturation specific humidity is proportional to the temperature, the relative humidity of the lifted parcel increases. At some point, the parcel can become saturated and subsequent condensation of water vapor will lead to the formation of clouds. See figure 5.2 for a graphical explanation of this phenomenon, where for simplicity it was assumed that the lifted air parcels do not mix with the environment. In reality, some mixing between the lifted air parcels and their environment, of course, occurs. However, the physical mechanism of cooling and subsequent saturation with water vapor that leads to cloud formation is similar.

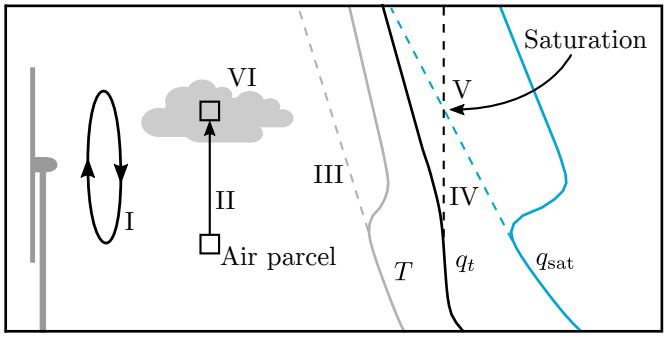

Figure 5.2: The torque exerted by the flow on the wind turbine blades induces flow rotation in the wake (I), opposite to the rotational direction of the rotor. The rotor-induced updraft causes air parcels to rise (II). The dashed lines represent vertical profiles of adiabatic parcels that are lifted in the upward moving branch of the wake. In this case, the temperature, T, of the air parcel follows the dry adiabate (grey dashed line, III). Being a function of temperature, the saturation specific humidity, q_{sat}, in the parcel decreases (blue dashed line, IV) but the total specific humidity, q_t, is conserved (black dashed line, IV). At some point q_t exceeds q_{sat} (V), the air parcel is saturated and condensation of water vapor will lead to cloud formation (VI).

In the first part of this chapter, we will extend on the work of Hasager et al. to determine the conditions, particularly in terms of temperature and humidity, that made cloud formation in the wake of the wind turbines possible. In the second part we will make a first attempt on simulating this complex case with our wind turbine-LES framework.

5.2. Case description

Although Hasager et al. collected a considerable amount of observational data from a range of sources, their study is only a starting point for the setup of a LES case. For example, the on-site meteorological (met.) mast provided no measurements of humidity, and of temperature only at $-3\,\mathrm{m}$, $16\,\mathrm{m}$ and $64\,\mathrm{m}$. However, due to prevailing winds from the south/south-east, Hasager et al. argue that the radio-sounding taken the night before (February 12, 00:00 UTC) in Schleswig (Germany), $150\,\mathrm{km}$ south-east of Horns Rev, is fairly representative for the air mass over Horns Rev. By combining the met. mast and radiosonde measurements with physical arguments, we can reconstruct the vertical profiles of temperature and humidity at the time of the photograph.

5.2.1. Vertical profile of temperature and humidity

The temperature and total specific humidity, q_t, profiles are directly coupled through the saturation specific humidity, q_{sat}, which is a function of temperature. Accordingly, the choice of the temperature profile affects the profile of q_t and vice versa. The saturation specific humidity can be calculated from the saturation water vapor pressure, e_{sat}, as

$$q_{\mathrm{sat}}(T,P) = \frac{(R_d/R_v)e_{\mathrm{sat}}(T)}{P-(1-R_d/R_v)e_{\mathrm{sat}}(T)}, \tag{5.1}$$

with $R_d = 287.0\,\mathrm{J\,K/kg}$ and $R_v = 461.5\,\mathrm{J\,K/kg}$, respectively, the gas constant of dry air and water vapor. To a good approximation, e_{sat} is given by (Murray, 1967)

$$e_{\mathrm{sat}}(T) = 610.78\exp\left[\frac{17.27\,(T-273.16)}{T-35.86}\right]. \tag{5.2}$$

As the surface pressure is known ($P_{\mathrm{sfc}} = 1037\,\mathrm{hPa}$), we can use the hydrostatic assumption for the pressure,

$$P(z^*) = P_{\mathrm{sfc}} - \rho g z^*, \tag{5.3}$$

to obtain the vertical pressure profile. Then, the vertical profile of q_{sat} is only determined by the choice of the vertical profile of temperature.

For clarity, we will discuss the important considerations concerning the temperature and humidity profiles in a systematic manner, where the Roman numerals in the text correspond with the relevant parts of figure 5.3.

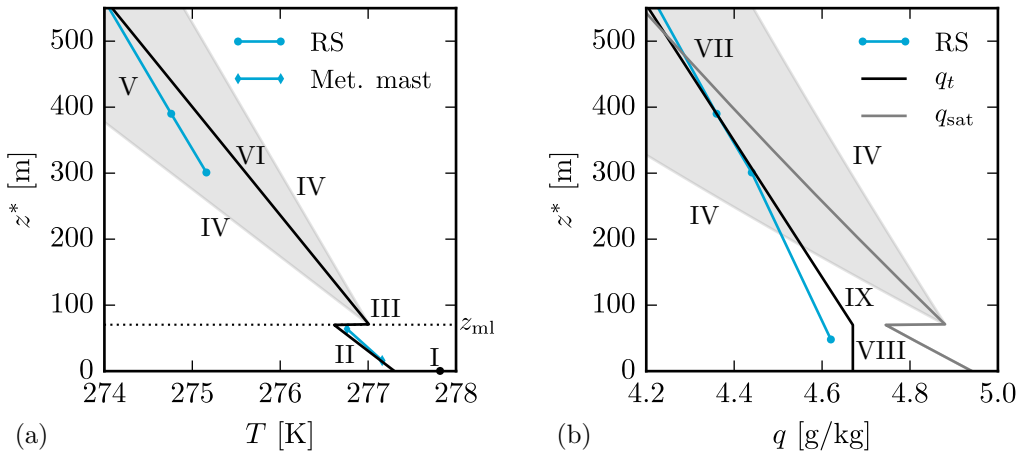

Figure 5.3: The black lines show best estimate vertical profiles of temperature (a) and total specific humidity (b) at Horns Rev at the time of the photograph. The shaded in area in (a) shows the range between the dry and moist adiabatic lapse rates. The grey line and shaded area in (b) indicate the q_{sat} profiles corresponding with the temperature profiles in (a). Furthermore, the blue dots indicate the radiosonde measurements collected over land 10 h before the observation of wake clouds. Finally, the Roman numerals refer to the appropriate sections in the text.

(I) Hasager et al. reported a satellite-based SST of about 278 K at Horns Rev, with an error around 0.7 K in cloud covered areas like the Horns Rev wind farm at the time of the photograph. Slightly lower SSTs were observed to the south/south-east of Horns Rev over which the air mass was advected towards the wind farm. The on-site met. mast measured a temperature of 277.8 K at 3 m depth. The photograph was taken on a cloud-covered, wintertime morning, which limits a possible error due to solar heating of the topmost water layer. Assuming a vertically well-mixed layer right below the sea surface, the temperature measurement at 3 m depth can thus be considered to be a good estimate of the SST. The SST is indicated by the black dot in figure 5.3a. Note that this dot indicates the temperature of the sea water, which is not the same as the temperature of the air just above the surface.

(II) The air mass at Horns Rev was exposed to a cooling over land the night before. Advection of this cold air over a relatively warm sea tends to lead to the formation of a (shallow) mixed layer at the surface. Up to 64 m, met. mast observations of the temperature are available. The measurements show that the temperature decreases approximately with the dry adiabatic lapse rate, $\Gamma_d = 9.8\,\text{K/km}$. This indeed indicates the presence of a layer that is well mixed in terms of the potential temperature. Further, met. mast data of the wind speed profile and local turbulence intensity confirm unstable conditions (at least) up to 64 m.

(III) A temperature inversion around hub height (70 m) confines vertical transport of moisture by convective turbulence to the extent of the mixed layer, extending from the surface to about 70 m. Throughout the rest of this work, we will refer to this layer as the surface

mixed layer (SML). If this temperature inversion would not be present, surface-driven convection would lead to saturated updrafts a few tens of meters above the height of the wake clouds, without the need for enhanced vertical transport by the wind turbines. However, a temperature jump increases q_{sat} right above the SML. Consequently, a too large temperature inversion would decrease the relative humidity above the SML, possibly up to a point where wind turbine-induced cloud formation can no longer occur. Unfortunately, met. mast observations are not available at this level and above, which leads to uncertainties in the exact height and strength of the temperature inversion.

(IV) Although the wind farm is sunlit at the time of the photograph, observations indicate the presence of stratocumulus clouds around Horns Rev. In a (non-decoupled) STBL, the potential temperature is typically well mixed in the sub-cloud layer. This would imply a temperature lapse rate approximately equal to Γ_d. In contrast, the radio-sounding taken at Schleswig the night before shows a lapse rate of about 4.4 K/km, close to the moist adiabatic lapse rate, up to 500 m above the surface. We can use this information to establish and upper and lower limit for the temperature profile, as indicated by the shaded area in figure 5.3a.

(V) Despite the effect of diabatic processes associated with a sheet of low clouds, like radiation and drizzle, the temperature profile measured at Schleswig is still thought to be reasonably representative for the temperature at Horns Rev sufficiently far above the SML. The blue dots in figure 5.3a show these measurements. The measurements fall within the range that was established at (IV).

(VI) The black line in figure 5.3a shows a possible temperature profile. The temperature is linearly interpolated between the temperature above the inversion and the Schleswig measurement at 571 m.

(VII) The vertical profile of the water vapor mixing ratio, r_v, at Schleswig is available. As $r_v \approx q_v$, we can plot these measurements in figure 5.3b. In the absence of a sink like drizzle, along with a positive humidity flux from the surface, this line sets a lower bound on the profile of the total specific humidity q_t, where $q_t = q_v + q_l$. Further, the profile of q_v intersects the profile of q_{sat}, calculated directly from the temperature profile of (VI), slightly below 500 m. As q_v is a lower bound for q_t, the intersection of q_v and q_{sat} gives an approximation of the cloud base height of the stratocumulus deck observed over Horns Rev. A cloud base height of about 500 m is rather close to the height of the strong temperature inversion (600 m) measured at Schleswig the night before. Further, as the temperature lapse rate above the SML directly sets the approximate cloud base height of the stratocumulus layer, this argument significantly refines the range of possible values of the temperature lapse rate.

(VIII) The radio-sounding at Schleswig shows a mixing ratio of about 4.6 g/kg at 48 m. With q_{sat} based on the met. mast temperatures, this corresponds to a rather low relative humidity in the SML. However, we have several reasons to believe that the specific humidity in the SML is higher than the measurement at Schleswig. First, evaporation of moisture from the sea surface, combined with convective mixing in the SML, gradually increases the moisture content in the SML. Secondly, q_v only sets a lower bound on the total specific humidity. As the radio-sounding shows a relative humidity of 100 % from 48 m to 571 m, some liquid water may have been present too. Finally, the photographs show a shallow layer of sea smoke above the sea surface, indicating the presence of saturated air. An upper bound on the specific humidity in the SML is, of course, set by q_{sat} and the fact that no clouds form in front of the wind farm. Due to turbulent fluctuations of q_t in the horizontal direction, the horizontal average specific humidity needs to be set slightly lower than the minimum of q_{sat} in the SML to prevent clouds from forming in moist, surface-driven thermals.

(IX) Above the SML, we assume a linear profile for q_t. We interpolate between the value at z_{ml} and the Schleswig profile at 390 m. In this case, the lifting condensation level is about 500 m which is close to the Schleswig measurements.

5.2.2. Setup of the simulation

Above we have tried to obtain best estimate vertical profiles of the temperature and humidity from observations and physical reasoning. Based on these profiles, we can establish a range of initial profiles for the LES, which will be discussed along with the results in the next section. Before the wind turbines are immersed in the flow, the simulation is run for two hours to allow spin-up of turbulence. During these two hours, the temperature and humidity profiles are continuously nudged towards the initial profiles. For details of this procedure and its implementation in DALES we refer to Heuff (2016). The aim is to have an accurate representation of the conditions during the photograph after the first two hours of simulation. The simulation is then continued with wind turbines to see if cloud formation occurs.

As the relevant physical processes that cause the formation of wake clouds occur from around hub height (70 m) up to several tens of meters above the maximum height of the wind turbines (110 m), we choose to only simulate the lower part of the sub-cloud layer up to 400 m.

Further, a geostrophic wind speed of 5 m/s was prescribed, resulting in a hub height wind velocity close to the reported values of about 4 to 4.5 m/s. The initial wind fields were set to the geostrophic values.

The lateral boundary conditions for the wind velocity, but also humidity and temperature, are again provided by a concurrent simulation without wind turbines (section 2.6). Consequently, any clouds formed by wind turbine-induced updrafts that leave the domain downstream of the wind turbines will not re-enter the domain.

As a surface boundary condition, we prescribe the roughness length and the surface temperature. A typical offshore roughness length of 2×10^{-4} m was set. To account for the increasing SST as the air mass is advected towards Horns Rev, the SST is linearly increased from 277.5 K to 277.8 K during the spin-up of the simulation.

The Horns Rev wind farm consists of 80 Vestas V80 2 MW wind turbines of which the implementation in DALES was already verified in section 2.4 and 3.2.3. In view of computational cost, only the first six turbines of a single row were simulated, on a horizontal domain of 4 km $\times$ 1 km. A resolution of 3.125 m was set in all directions to resolve a sufficient amount of the turbulence in the flow.

5.3. Simulation results

Although the vertical profile of temperature and humidity established in section 5.2.1 provide a starting point for the initial profiles of the LES, they still have a reasonable degree of uncertainty. In addition, as the air mass is advected from the land, the SST increases slightly. Hence, the time development of the SST also introduces an uncertainty. Accordingly, fine-tuning of the parameters in an empirical way is required to determine an atmospheric state which yields cloud formation only in the presence of wind turbines.

A range of experiments was set up, each with a slightly different initial temperature and/or humidity profile and time development of the SST. We have selected three particular experiments from this set to illustrate the challenges and difficulties in simulating the Horns Rev case. The first experiment is a reference (REF) experiment in which the reconstructed profile of temperature and humidity are represented as accurately as possible in the LES. The second experiment closely resembles the reference experiment but shows a stronger temperature inversion (STI) at the top of the SML. Finally, in the third experiment the temperature is set to decrease with the dry adiabatic (DA) lapse rate above the SML.

5.3.1. Experiment 1: reference (REF)

The first experiment was set up to approximate the best estimate profiles established in the previous section as close as possible after 2 h of simulation, as indicated by the blue line in

figure 5.4. The profiles show that on average the air mass is unsaturated at each height. Still, due to turbulence in the ambient flow, significant cloud formation is already observed in this simulation in the absence of wind turbines.

5.3.2. Experiment 2: stronger temperature inversion (STI)

To prevent regular cloud formation like in the reference experiment, a stronger temperature inversion at the top of the SML was set in the second experiment (black line in figure 5.4a). A higher temperature above the inversion helps to contain turbulence to the extent of the SML. Further, as q_{sat} is proportional to the temperature, the relative humidity is lower at equal q_t which also helps to avoid cloud formation in the absence of wind turbines. Compared to REF, q_{sat} above the SML is only about 0.1 g/kg higher. However, no cloud formation to any significant degree was observed in this experiment, even after immersing the wind turbines in the simulation.

The first two experiments clearly demonstrate the difficulty of simulating this case. If the ambient relative humidity is too high, clouds develop without the need for increased vertical mixing by wind turbines. In contrast, when the ambient relative humidity is too low, no clouds form at all.

5.3.3. Experiment 3: dry adiabatic (DA) lapse rate above SML

In the last experiment that will be described here, we allowed a larger deviation from the best estimate profiles to see if it was possible to simulate wind turbine-induced cloud formation at all. By setting a strong temperature lapse rate above the SML, close to Γ_d, the air parcels that are lifted by the updraft in the wake are warmed less by mixing with the environment and therefore maintain a higher relative humidity. Additionally, due to relatively strong negative buoyancy, air parcels cannot rise significantly above the SML without the aid of updrafts in the wind turbine wake.

A constant specific humidity was set up to 130 m, again to prevent a decrease of the relative humidity of the lifted air parcels due to mixing with the environment. The combination of a high specific humidity and a steep temperature lapse rate makes wake clouds more likely. However, using the humidity lapse rate of the first two experiments above the SML would lead to a cloud base height of the stratocumulus layer above the wind farm of 150 to 200 m, i.e. significantly lower as observed. To avoid stratocumulus from developing at this height, the relative humidity is limited to 98 % above 130 m. Accordingly, we arrive at a rather unrealistic humidity profile, as shown by the grey line in figure 5.4b. The temperature profile does still match the met. mast observations in the SML, but shows a larger than observed lapse rate above the SML.

At the cost of a lesser agreement with the observations, in this experiment liquid water is formed in increasing quantities behind the wind turbines during the first 10 minutes after the wind turbines are immersed in the simulation (figure 5.5). As mentioned before, the boundary conditions are provided by an identical simulation without wind turbines. Thus, all cloud formation can be attributed to the wind turbines as long as no clouds form in the precursor simulation.

At Horns Rev, the initial point of cloud formation was 50 to 100 m behind the wind turbines (Hasager et al., 2013). In the simulation, however, the first clouds form only about 1 km behind the first wind turbine. Also, figure 5.6 shows that the cloud base height of the wake clouds in the simulation is considerably higher compared to the observations. Where the cloud base height in the photograph is approximately at hub height, in the simulation it is located around the maximum height of the wind turbines, $\sim$ 40 m higher. This can be an indication that mixing between the relatively warm air above the SML, and the air parcels that are lifted in the wake, prevents saturation up to the height where the ambient air temperature is low enough to allow for condensation of water vapor. Finally, the wake clouds at Horns Rev seem to extend in the downstream direction almost continuously from the point of formation. In contrast, the simulated cloud field shows relatively small and isolated clouds.

Besides analysis of the LWP, a three-dimensional visualization of the liquid water specific

humidity field, q_l, was made. The values of q_l at every grid point were converted to a voxel data format that can be read by Blender, an open-source 3D graphics and animation software package. Three-dimensional models of the wind turbines were then added in Blender, along with a sea surface. The result is shown in figure 5.7, which confirms that the observed cloud field is quite different from the simulated cloud field.

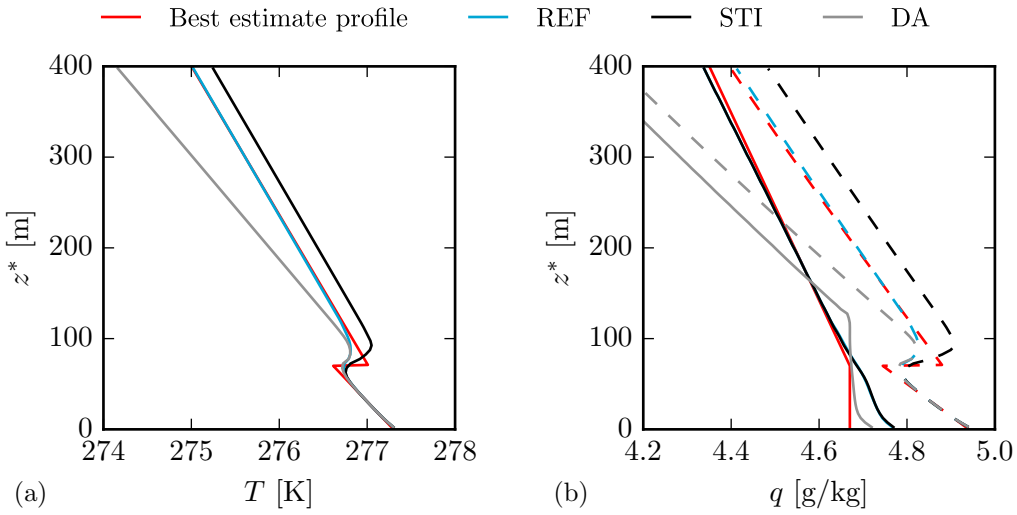

Figure 5.4: Vertical profiles of temperature (a) and total specific humidity (solid line) and saturation specific humidity (dashed line) (b) after two hours of simulation, for three experiments (REF, STI and DA) initialized with different temperature and humidity profiles. See the approriate sections in the text for details about the experiments.

5.4. Discussion and conclusions

Several (possible) explanations for the discrepancies between the observations and the simulations can be readily identified.

First, the representation of liquid water in DALES is of primary importance in this case. DALES diagnoses q_l in a certain grid box from the pressure, temperature and total specific humidity. It is assumed that no liquid water is present in an unsaturated grid box, while all moisture exceeding the saturation specific humidity exists in the form of liquid water:

$$q_l = \begin{cases} q_t - q_{\text{sat}}, & \text{if } q_t > q_{\text{sat}} \\ 0, & \text{otherwise} \end{cases} . \tag{5.4}$$

This 'all or nothing' representation of cloud water in DALES can affect the calculated values of q_l. If a cloud would only partly fill a grid box, on average the grid box can still be unsaturated. In this case, it appears as if no cloud is present at all. Since the necessary conditions for the cloud formation in the wake are very delicate, this may cause the model to underestimate cloud formation.

Additionally, inaccurate representation of the contribution of SFS mixing above the SML can prevent saturation of air parcels that are lifted in the wake. More specifically, when this contribution is overestimated, excessive entrainment of relatively warm and dry air from the environment into the lifted air parcels decreases the relative humidity. Accordingly, the air parcel may not become saturated and no liquid water is formed.

Furthermore, the wind turbine parameterization that was used does not resolve the flow around the rotor blades. Although the updraft in the wake is captured by the non-uniform actuator disk model (figure 3.5), e.g. vortices at the tip of the blades are not. Consequently, the turbulence structure of the near wake may not be very well represented in the LES. This may be part of the reason why clouds only form relatively far downstream of the wind turbines.

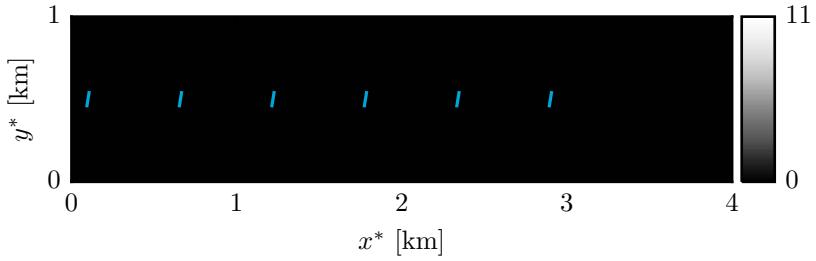

(a) $t = 1\,\text{min}$.

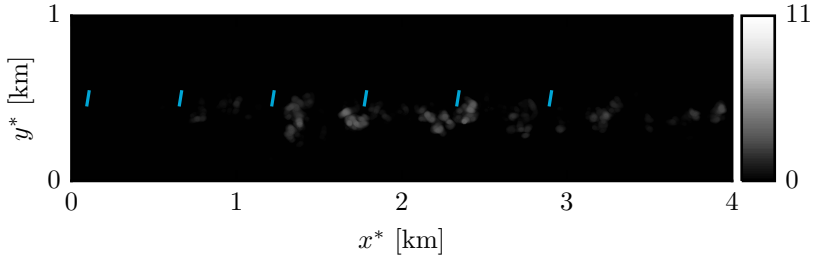

(b) $t = 5\,\text{min}$.

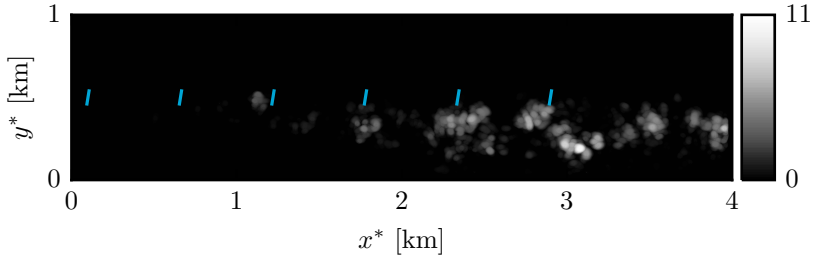

(c) $t = 10\,\text{min}$.

Figure 5.5: LWP $\left[\text{g/m}^2\right]$ as calculated by DALES at three different time instances. The times are taken from the moment when the wind turbine are immersed in the simulation, i.e. after the two hour spin-up. The blue lines represent the wind turbines. The average wind direction at hub height is about 280°, as also indicated by the rotor planes that have a slight offset with respect to the y^*-direction.

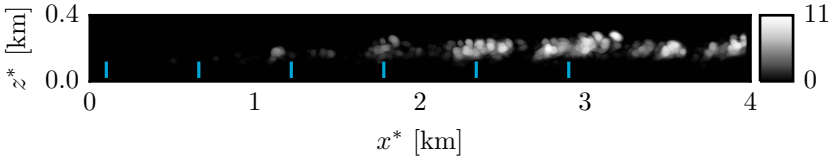

Figure 5.6: LWP $\left[\text{g/m}^2\right]$ in the y^*-direction at $t = 10\,\text{min}$. The blue lines again indicate the wind turbine rotors.

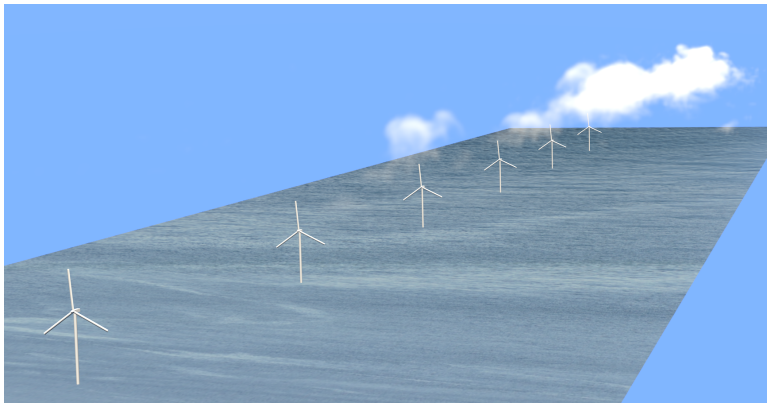

Figure 5.7: Three-dimensional visualization of the liquid water specific humidity field at $t = 10\,\text{min}$. The ocean image indicates the horizontal extent of the simulation domain.

Also, representation of the meteorological conditions may not be sufficiently accurate in the simulation. For example, Hasager et al. (2013) identify a layer of saturated air just above the sea surface ('sea smoke'). In the simulation we were not able to represent this phenomenon. A surplus of humidity at the surface is quickly mixed in the vertical direction by the convective turbulence in the SML. This will likely occur in any LES due to the unstable surface stratification.

To conclude, wind turbine-induced cloud formation was observed in the simulations, but the structure and distribution of the simulated clouds did not match the observed cloud field. Additionally, a considerable deviation from the best estimate temperature and humidity profile was required to have clouds form in the wake of wind turbines. However, we believe that our study into the meteorological conditions at Horns Rev at the time of the famous photograph is a valuable addition to the work of Hasager et al. (2013) in the understanding of this complex case, and that it provides a more specific starting point for future simulations.

6

Summary and outlook

6.1. Summary

The main objective of this work was to develop a large-eddy simulation-based wind farm power output modeling framework. Where such a model can potentially be used for a wide range of applications, including e.g. resource assessment and fatigue analysis, this report was primarily focused on the use of large-eddy simulation (LES) for wind power forecasting. To this end a wind turbine parameterization was implemented in the Dutch Atmospheric Large-Eddy Simulation (DALES) model. The wind turbine model was formulated in a general way, which allows application in a wide range of cases. Given the characteristics of the specific wind turbines, virtually any wind farm can be simulated by only providing the hub coordinates of each wind turbine.

Calculation of the wind turbine force components is performed fully parallel, where each wind turbine is distributed to a different processing unit. This does require the number of processing units to be at least equal to the number of wind turbines, a condition that is typically fulfilled by default for a high-resolution LES on a wind farm-sized domain.

The yaw angle of each individual wind turbine is dynamically controlled to maintain optimal alignment of the rotor to the local mean wind direction. Due to directional wind shear in the atmospheric boundary layer (ABL), parts of the rotor will often still exhibit a limited degree of yaw misalignment. Intentionally applying a yaw error to a wind turbine showed that the model is capable of correctly predicting the resulting power deficit.

Validation of the modeling framework was performed in several ways. First, the power production as calculated by our model was compared with the power curve of two utility-scale wind turbines. Although several improvements to the wind turbine model are still required, mainly with regard to the blade pitch and rotational speed control, the calculated power showed reasonable agreement with the power curve for both wind turbines. The simulated velocity deficits in the wake of a single wind turbine were also compared with LiDAR measurements that were obtained in three different field campaigns. The LES results show a good agreement with the measurements in both stable and convective conditions. Finally, a real world offshore wind farm, consisting of thirty 2 MW wind turbines, was simulated. The wake-related power deficit in the wind farm as calculated by DALES was found to be reasonably close to production data in neutral and convective conditions.

The first part of the report is primarily focused on the technical details of the model and its validation. Next, in chapter 4 and 5, the model was used to study two particular cases in more detail. As DALES is one of the few LES codes with the capability of representing clouds, we selected two cases in which clouds play a major role.

First, wake evolution and wind farm performance in the stratocumulus-topped boundary layer (STBL) was considered. As the STBL shows a marked diurnal cycle with regard to the turbulence structure, strong variations in wake extent and wind farm efficiency were expected. During the night, in the absence of solar radiation, long-wave radiative cooling from the cloud

top drives turbulence throughout the ABL and the wind velocity in the wake was found to recover significantly faster as compared to daytime. The associated reduction of the wake related power deficit led to a considerable increase in the wind farm efficiency. In an additional simulation with the same surface buoyancy flux, but without clouds, this effect was not observed. From this we can conclude that radiative processes in a stratocumulus cloud layer can have a significant impact on wind farm performance.

Moreover, in contrast to clear convective conditions, strong convective turbulence in the STBL only leads to a minor wind speed reduction due to turbulent drag. Consequently, a high wind farm efficiency is not counteracted by lower wind speeds, which led to a geostrophic wind farm efficiency about twice as high as in the clear case.

Finally, we made a comparison with the results of a diurnal variation study in a clear boundary layer (Abkar et al., 2015). This showed that the time evolution of the wind farm efficiency is exactly opposite. Where the efficiency peaks at midday in the the clear boundary layer, it has a minimum in the STBL. Similarly, the lowest efficiency is found during the night in clear conditions, but in case of stratocumulus it has a maximum at this time.

In the final case study we made an attempt to simulate wind turbine-induced cloud formation as observed at the Horns Rev offshore wind farm in February, 2008. Hasager et al. (2013) argued that cooling of air parcels in the updraft of the rotating wake leads to condensation of water vapor. Consequently, clouds can form that follow the structure of the upward turbulent motion in the wake. Based on sparse observational data and a careful consideration of atmospheric thermodynamics and boundary-layer dynamics, we reconstructed the most probable atmospheric state at Horns Rev that yields cloud formation only in the presence of wind turbines. A range of experiments were set up to simulate the formation of wake clouds with our model. A considerable deviation from the reconstructed temperature and humidity profile was, however, required to observe any wind turbine-induced cloud formation. Still, we believe that the study in this chapter provides a valuable addition to the work of Hasager et al. in the understanding of this complex case and a more specific starting point for future simulations.

6.2. Towards an operational wind power forecast model

Throughout the report several potential improvements of the model were briefly mentioned. In this section we will go into more detail on the developments necessary to make the model suitable for operational use. Two primary design characteristics were identified in section 2.1: general applicability and adequate performance in terms of accuracy and computation time.

As discussed in the summary, the model in its current form can in principle simulate any wind farm given the proper meteorological and wind turbine input data. Hence, we can focus on the second design requirement, the performance of the model. Although the current wind turbine parameterization can already quite accurately represent the power production and the velocity deficit in the wake, some improvements are still required.

To begin with, the dynamic control of the rotational speed and pitch angle of the blades are handled in a very artificial way. Presently, tabulated values of these two parameters are provided as input as a function of the local free-stream wind speed. Apart from the fact that this approach is rather unrealistic, the required data is often not available. Wu and Porté-Agel (2015) proposed to calculate the rotational speed for a certain wind turbine iteratively from the unique relation between torque and wind speed. This was done in a separate series of simulations, after which the resulting rotational speed was prescribed to the LES. Creech et al. (2015) calculate the angular acceleration of the rotor at each time step from the torque and moment of inertia of the blades. Given the acceleration, the rotational speed at the next time step is then obtained by numerical integration. This approach does require a model for the torque of the generator. The generator can, however, be modeled in a simple manner for wind speeds up to about 10 m/s. Creech et al. also implemented an active pitch control mechanism which is valid up to about the rated wind speed. Both modifications discussed above can be added to DALES in a quite straightforward manner.

Even though the non-uniform actuator disk approximation incorporates both axial and tangential forces, it does not resolve the rotating blades. Instead, the mean effect of the

rotating blades on the swept rotor area is considered. In contrast, in the actuator line model the wind turbine forces are distributed on lines that follow the rotating blades (Mikkelsen, 2003, Sørensen and Shen, 2002). Although Porté-Agel et al. (2011) showed that the non-uniform actuator disk and the actuator line model show very similar results, explicit representation of the rotating blades can improve near wake modeling. The actuator lines can in principle be distributed onto the computational grid in a similar way as was done for the actuator disk in this work.

Finally, additional extensions to the wind turbine parameterization can include rotor tilt (Aitken et al., 2014b, Creech et al., 2015) and a model to obtain the available electrical power from the extracted power.

Besides increasing the accuracy of the parameterization, important steps need to be made with regard to computational time. So far, the model is still slower than real time, i.e. simulation of the wind field for one second takes, depending on the computational configuration, at least two to three seconds of computation time. Further increasing the grid spacing reduces the computational cost but results in a less accurate representation of the wake structure (Wu and Porté-Agel, 2013). Fortunately, the emergence of a relatively new way of high-performance computing can resolve this issue.

In recent efforts, Schalkwijk et al. (2012, 2015, 2014) showed the enormous potential of using graphic processing units (GPUs) for LES instead of central processing units (CPUs). The sizable performance increase that would come with running our code on GPUs immediately makes it a viable option for wind power forecasting. However, the wind turbine code will have to be rewritten and modified to allow implementation in a GPU-LES framework.

In a typical LES run on GPUs, the number of processing units is much larger than in case of CPUs. Consequently, the number of processing units will be much larger than the number of wind turbines. Hence, the parallelization of the wind turbine code would also have to be modified to allow multiple processing units to perform the calculations for a single wind turbine.

Sufficient speedup can potentially also be achieved by only running parts of the current model on GPUs. Employing a special compiler, based on the OpenACC standard, makes it possible to run the code partly on GPUs with minimal modifications. This way, significant acceleration of the code can be achieved (Wienke et al., 2012). Exploring the possibilities of this hybrid CPU-GPU computation has recently been started in our group.

Computation time can additionally be reduced by changing the way the turbulent inflow boundary conditions are obtained. The most direct improvement would be to follow Stevens et al. (2014) and perform the precursor simulation parallel to the wind turbine simulation. This way, the power of additional processing units will be exploited in a better way than by further reducing the number of grid points per processing unit where increasingly more time is consumed by communication processes. This also touches on the general need for performing a study into the optimal number of grid points per processing unit.

The possibility of nesting a fine-scale LES with wind turbines into a coarser LES was briefly mentioned in section 2.7. Depending on the atmospheric conditions, the computational cost of the precursor simulation can be significantly reduced this way. Mirocha et al. (2014) and Aitken et al. (2014b) already successfully implemented this concept. One can also think of locally refining the grid resolution around the wind turbines, as was done by e.g. Churchfield et al. (2012b) and Creech et al. (2015). In addition, actively adapting the grid resolution during the simulation (Popinet, 2003) to the prevailing stability conditions can prove useful in the simulation of diurnal variations (van Hooft et al., in preparation). However, a major revision of the code would be necessary, making the nesting approach more promising on the short term.

Aside from potentially reducing the computational cost of the precursor simulation, coupling with a coarser model could have an additional benefit. A lower resolution model can, of course, cover a larger domain. Coupling of the wind turbine model to a large-scale simulation, e.g. a turbulence-resolving mesoscale weather forecast (Schalkwijk et al., 2014), can potentially provide realistic time-varying boundary conditions to run an operational wind power forecast.

Moreover, a two-way coupling between the high-resolution LES and the large-scale weather model can be considered. This way, the significant effect of wind farms on the wind speed in the ABL (Baidya Roy et al., 2004) can be included without having to rely on wind farm parameterizations that e.g. only increase the local roughness length (Keith et al., 2004). As wind farm wakes are still observed many kilometers downstream (Christiansen and Hasager, 2005, 2006, Li and Lehner, 2013), and wind farms become larger and more numerous, large-scale mutual interaction between neighboring wind farms cannot be neglected.

For calculation of the surface boundary conditions in a LES, generally the roughness length needs to be prescribed. As the roughness of the surface has an impact on the production of turbulence, wake evolution is affected by the magnitude of the roughness length (Wu and Porté-Agel, 2012). Offshore, where most large-scale wind farms are located, the roughness length depends on the height of the waves, which are again influenced by the wind near the surface. Typically, the roughness length is parameterized by Charnock's relation, an empirical relation between the roughness length and the friction velocity. This does, however, require specification of a proportionality constant, the Charnock parameter, which is actually far from constant and hypothesized to depend on the surface wave spectrum (Fairall et al., 1996). Instead, a (two-way) coupling between the LES model and an ocean wave model can be established to deliver a realistic prediction of the local roughness length and thus provide a more realistic surface boundary condition.

6.3. Other applications

So far we have focused on the use of our model for wind power forecasting. The modeling framework does, however, have various additional applications.

To start with, LES can potentially become a valuable tool to improve and refine statistical forecast models. In the current model a precursor simulation is employed to provide the boundary conditions. The atmospheric conditions (wind velocity, stability) in the precursor simulation can thus be directly correlated with the wind farm power in the simulation with wind turbines. Now, all atmospheric conditions in the relevant wind speed, wind direction and stability regimes can be simulated and stored in a database along with the corresponding wind power (fluctuations). This computationally expensive procedure can be done offline and is only required once for a particular wind farm. Then, the operational forecast can be reduced to correlating the predicted atmospheric conditions to the wind power in the database. Although an accurate weather forecast is still necessary, this approach prevents from having to simulate the entire wind farm in the operational phase, where only a (very) limited time frame is available. Additionally, statistical models can be 'trained' and validated with this extensive LES-generated data set that connects atmospheric conditions to wind farm power production. Likewise, providing a fine-scale LES weather forecast to statistical models that relate local meteorological data to the output of a specific wind farm might increase their predicting capabilities (Ellis et al., 2015).

Correlation of the wind farm power to atmospheric conditions can also be employed in the resource assessment phase. Given the layout and the large-scale meteorological conditions of the site, a precise wind resource assessment can be made that can include several effects that are currently not well accounted for. For example stability conditions, orography and complex terrain (Uchida and Ohya, 2003) and the built environment (Pourquie et al., 2009) can be included in a LES-based resource assessment.

Furthermore, LES can be used to fine-tune the layout of a wind farm (Meyers and Meneveau, 2012) according to the site conditions. Likewise, it might be an ideal tool to study optimal control of the individual wind turbines to maximize the total wind farm output (Goit and Meyers, 2014). One can think of down-regulating upwind wind turbines by adjusting the blade pitch angle or even forcing a slight yaw misalignment (Wagenaar et al., 2012). This way, the velocity deficit in the wake can be reduced, or the wake can be diverted to prevent partial intersection with a downstream rotor. Specifically in neutral or stable conditions, when the wake extends over a long distance, this could increase the total power of the wind farm.

Wind turbine fatigue analysis is another field of research that still heavily leans on param-

eterizations of turbulence and wind shear, often without the inclusion of stability effects in the design requirements (Sathe et al., 2013). LES-generated wind fields can not only include site-specific information on the turbulence intensity, but also on the vertical wind velocity profile, which is of major importance in case of, e.g., the occurrence of low-level jets. The strong (directional) wind shear associated with their occurrence can have a major impact on blade loads (Sisterson and Frenzen, 1978).

Low-level jets, at least over land, are typically associated with stable conditions. Stable conditions require special attention for other reasons besides fatigue. For example, the directional wind shear may ask for more refined yaw control. As noted in section 2.5, the yaw angle for optimal energy extraction may not coincide with the hub height wind direction. Further study of this phenomenon with LES may help the development of front-looking, nacelle-mounted LiDAR systems that can potentially detected such situations (Mikkelsen et al., 2013).

Where most of this work is focused on applications in wind power engineering, the wind turbine model and the results presented in this work can also be an important motivation for studies from the viewpoint of the atmospheric sciences. As DALES is first and foremost a tool for study of the atmosphere, we think it is appropriate to conclude with a discussion of the relevance of this work to the conventional applications of DALES.

Using LES for further study of the effect of large wind farms on the vertical profiles of wind velocity, temperature, humidity and the turbulent fluxes, can provide essential information for the improvement of wind farm parameterizations in large-scale weather models. As it has been established that wind farms can have a considerable effect on local meteorology (Baidya Roy et al., 2004, Fitch et al., 2013), their increasing number makes proper representation in weather forecast models necessary.

As confirmed in chapter 3 and 4, wind farm power is determined by the complex interplay between wind speed, wind direction and wake extent. All three are strongly dependent on turbulence, more specifically on the vertical transport of momentum in the ABL. As of now, its effect on the most relevant quantity, the wind speed, in, for example, the STBL is not very well understood. Most notably, the wind speed in the STBL was found to increase to supergeostrophic levels in the afternoon. As prediction of the occurrence of such a situation is highly relevant for wind energy applications, but also for weather forecasts in general, further research into this topic is recommended.

Correct prediction of stratocumulus itself is also vital to incorporate the effects found in chapter 4 in a wind power forecast. Still, conventional weather models often have issues with proper representation of these relatively thin and low clouds. Furthermore, their strong radiative properties also have a huge impact on the forecast of solar power.

Likewise, the stable boundary layer is another subject of ongoing research that has sizable implications for wind energy applications. While particularly difficult to model, accurate representation of the wind velocity profile and turbulence in stable conditions is essential for wind power forecasts, resource assessment, control and fatigue.

A

DALES

A.1. Governing equations

The prognostic variables of DALES are the velocity components, u_i^*, liquid water potential temperature, θ_l, total specific humidity, q_t, and the sub-filter scale turbulence kinetic energy (SFS TKE), e. After application of the LES filter, the anelastic approximation is employed to solve the equations of motion (Böing, 2014):

$$\frac{\partial \rho_0 \widetilde{u_j^*}}{\partial x_j^*} = 0 \tag{A.1}$$

$$\frac{\partial \widetilde{u_i^*}}{\partial t} = -\frac{1}{\rho_0}\frac{\partial \rho_0 \widetilde{u_i^*}\widetilde{u_j^*}}{\partial x_j^*} - \frac{\partial \pi}{\partial x_i^*} - \frac{1}{\rho_0}\frac{\partial \rho_0 \tau_{ij}}{\partial x_j^*} + g\delta_{i3}\frac{\widetilde{\theta_v} - \theta_{v,E}}{\theta_{v,E}} + f^{\mathrm{cor}}\epsilon_{ij3}\left(\widetilde{u_j^*} - U_j^{\mathrm{geo}}\right) \tag{A.2}$$

$$\frac{\partial \widetilde{\chi}}{\partial t} = -\frac{1}{\rho_0}\frac{\partial \rho_0 \widetilde{u_i^*}\widetilde{\chi}}{\partial x_j^*} - \frac{1}{\rho_0}\frac{\partial \rho_0 R_{u_j^*,\chi}}{\partial x_j^*} + S_\chi, \tag{A.3}$$

where the tilde represents spatial filtering. The scalar equations are written in terms of a general scalar variable, χ, where $\chi \in \{\theta_l, q_t\}$. The time-independent base-state density, ρ_0, is based on the international standard atmosphere with a surface temperature correction. The modified pressure is given by $\pi = \widetilde{\delta p}/\rho_E + \frac{2}{3}e$, where δp is the pressure fluctuation with respect to the environmental hydrostatic state, indicated by a subscript E. Like the base state, the environmental hydrostatic state varies only in the vertical direction, but is a function of time and in general a closer approximation to the horizontally averaged state of the atmosphere.

Several LES studies of wind turbine dynamics did not include buoyancy effects (Calaf et al., 2010, Creech et al., 2015, Jimenez et al., 2007, Nilsson et al., 2015), which are, however, necessary to capture stability effects. Often the Boussinesq approximation in terms of the potential temperature, valid in the lowest part of a dry atmosphere, is therefore used (Allaerts and Meyers, 2015, Churchfield et al., 2012a, Wu and Porté-Agel, 2011). DALES employs the more general anelastic approximation and, in order to incorporate the effect of moist, the potential temperature is replaced by the virtual potential temperature, θ_v.

The large-scale pressure gradient that drives the flow is written in terms of the geostrophic wind, U^{geo}, which is provided as input to the simulation. Further, f^{cor} is the Coriolis parameter and ϵ_{ijk} is the Levi-Civita symbol.

The SFS fluxes are modeled through an eddy viscosity (K_m) and eddy diffusivity (K_h):

$$\tau_{ij} = -K_m\left(\frac{\partial \widetilde{u_i^*}}{\partial x_j^*} + \frac{\partial \widetilde{u_j^*}}{\partial x_i^*}\right) \tag{A.4}$$

$$R_{u_j^*,\chi} = -K_h\frac{\partial \widetilde{\chi}}{\partial x_j^*}. \tag{A.5}$$

By default, closure of the equations for SFS turbulent fluxes is achieved by modeling the eddy viscosity/diffusivity as a function of the SFS TKE:

$$K_m = c_m \lambda \sqrt{e} \tag{A.6}$$

$$K_h = c_h \lambda \sqrt{e}. \tag{A.7}$$

The coefficients c_m and c_h are constants and λ is a length scale related to the grid spacing and stability of the flow. A prognostic equation is implemented for the SFS TKE. See Heus et al. (2010) for a full discussion on the SFS model.

A.2. Contribution of the SFS model

In a LES, the TKE in the resolved scales should be much larger than the SFS TKE to keep the error associated with the SFS parameterization to a minimum. In case of strong velocity gradients, e.g. around a wind turbine, we can expect to have a relatively large SFS contribution. To quantify this effect we will perform a brief study into the relative contribution of the SFS model in a typical simulation.

The largest contribution of the SFS model is expected in stable conditions, when no large-scale convective motions reside in the resolved scales. Hence, we once more consider the SBL case of Aitken et al. (2014b), discussed before in section 3.2.1. The resolved TKE is shown in figure A.1, along with the SFS TKE in figure A.2. Figure A.1a and A.1b are equivalent to figure 3.7a and 3.7b but repeated here to facilitate comparison to the SFS TKE. Note the difference in the color scale between figure A.1 and A.2 which is necessary to properly visualize the SFS TKE distribution. The relative contribution of the SFS TKE to the total TKE, i.e. $e/\left(\mathrm{TKE} + e\right)$, is plotted in figure A.3.

As usual in a LES, the highest amount of SFS TKE is found at the surface. In the near wake the SFS TKE and resolved TKE are distributed similarly, with high levels around the shear layers between high and low wind velocity. Excluding the surface, the relative contribution of the SFS TKE to the total TKE peaks at about 40 % right behind the wind turbine. In the near wake, turbulence that can be resolved by the LES is still developing. After about $2D$, the resolved TKE increases significantly and the relative contribution of the SFS drops to the ambient level.

A more detailed study into the contribution of the SFS model in different stability conditions and grid configurations is a current research objective. Depending on the results of this study, implementation of a different SFS parameterization might be considered. Besides the SFS TKE model, the closely related Smagorinsky SFS model is also included in DALES. This model is often used in wind turbine-LES frameworks (KULeuven code of Calaf et al., 2010, Churchfield et al., 2012b, Jimenez et al., 2007, Mirocha et al., 2014) and its performance in wind turbine simulations with DALES could be compared straightforwardly with the SFS TKE model.

A tuning-free Lagrangian scale-dependent dynamic model, as used by Porté-Agel et al. (2011) and in the JHU-LES code of Calaf et al. (2010), can, at the cost of slightly increased computation time, potentially lead to better results in certain conditions. Still, this is an eddy viscosity SFS model. In the future, further improvements might be expected from different kinds of SFS models (Mehta et al., 2014).

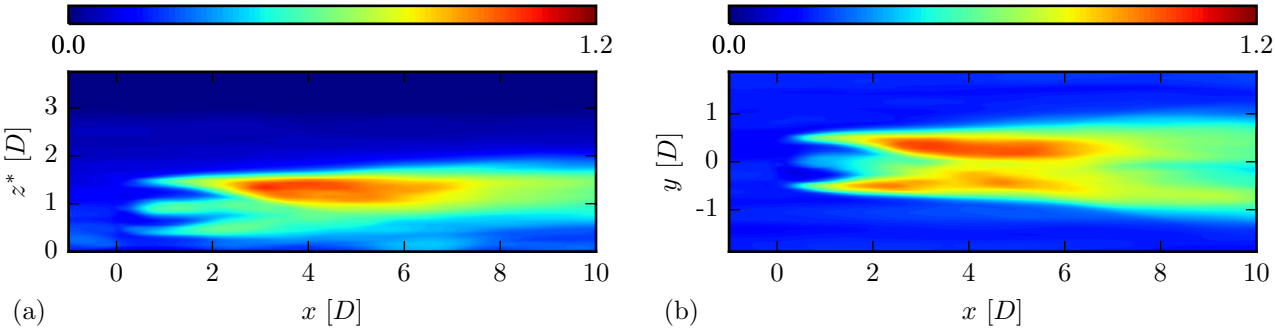

Figure A.1: 10 min-average resolved TKE [m^2/s^2], in a vertical (a) and horizontal (b) plane.

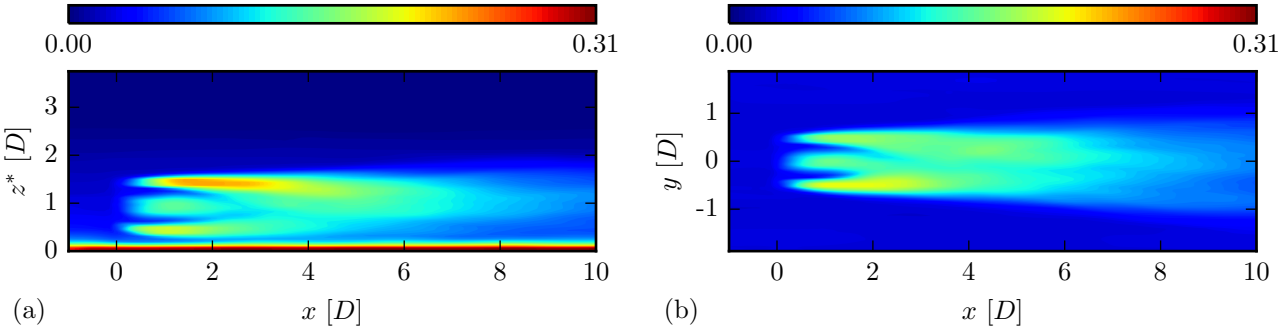

Figure A.2: 10 min-average SFS TKE [m^2/s^2], in a vertical (a) and horizontal (b) plane.

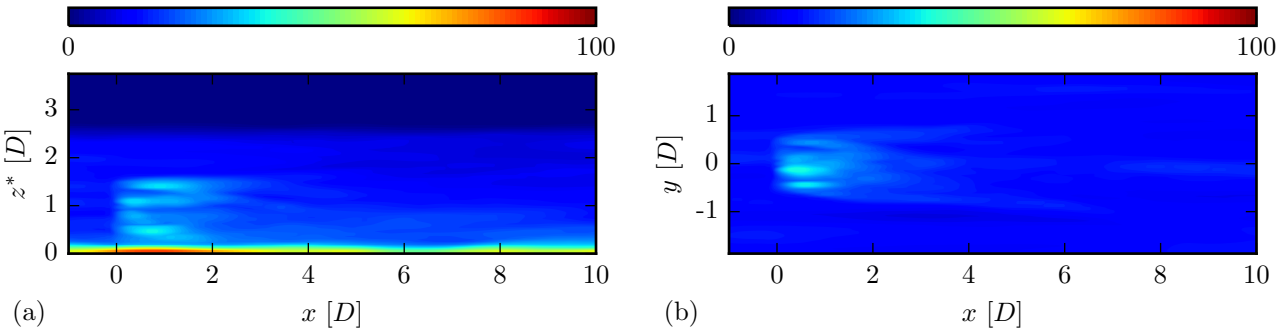

Figure A.3: SFS TKE relative to the total TKE [%], in a vertical (a) and horizontal (b) plane.

B

Details of the wind turbine implementation

B.1. Smoothing and suppression of 2dx-waves

The rotor geometrical footprint in equation (2.17) contains a Gaussian convolution filter of the form

$$G(\mathbf{x}) = \left(\frac{6}{\pi\epsilon^2}\right)^{3/2} \exp\left(\frac{-6\|\mathbf{x}\|^2}{\epsilon^2}\right). \tag{B.1}$$

An important consideration is the value of the filter width, ϵ, in (B.1). A relatively small value of ϵ does represent the wind turbine more realistically, i.e. the wind turbine is smoothed out to a lesser extent. However, in case of insufficient smoothing, the strong velocity gradients right before and at the edges of the rotor disk can lead to numerical errors in the form of 2dx-waves (Lu and Porté-Agel, 2011).

In any case, the filter width should be grid size dependent. Since the grid is in general not equidistant, we expand (B.1):

$$G(\mathbf{x}) = \sqrt{\frac{6}{\pi\epsilon_1^2}}\sqrt{\frac{6}{\pi\epsilon_2^2}}\sqrt{\frac{6}{\pi\epsilon_3^2}} \exp\left(\frac{-6x^2}{\epsilon_1^2}\right) \exp\left(\frac{-6y^2}{\epsilon_2^2}\right) \exp\left(\frac{-6z^2}{\epsilon_3^2}\right), \tag{B.2}$$

where ϵ_i $(i = 1, 2, 3)$ is the filter width vector. Meyers and Meneveau (2010) proposed to scale the filter width with the respective grid spacing in each direction as

$$\epsilon_i = 1.5\Delta x_i^*. \tag{B.3}$$

Van Heerde (2015) considered spatial smoothing of the wind turbine forces in a modified version of DALES in more detail. Axial smoothing, in contrast to radial smoothing, was found to significantly increase the quality of the flow fields. The amount of smoothing proposed by Van Heerde more or less corresponds to the value used by Meyers and Meneveau. Based on this the filter width as defined in (B.3) was used in all simulations.

Finally, the numerical advection scheme that is used also has a significant impact on the formation of 2dx-waves. In some of the initial simulations, with a relatively simple 2^{nd} order central differencing scheme, 2dx-waves were observed in front of the wind turbine were the velocity gradients are high. After switching to a 5^{th} order upwind scheme, the default in DALES, 2dx-waves were not observed anymore.

B.2. Numerical computation of the geometrical footprint

The rotor geometrical footprint is given by equation (2.17), which we repeat here for convenience:

$$\mathcal{R}(\mathbf{x}) = \iiint G(\mathbf{x} - \mathbf{x}'')\delta(x'')H\left(R - r''\right) \mathrm{d}^3\mathbf{x}''. \tag{B.4}$$

Like Meyers and Meneveau (2010), we evaluate the integral in (B.4) on a very fine grid around each grid point in the wind turbine subdomain (section 2.7). The integral needs to be recalculated every time the yaw orientation changes. Some careful thought about efficient evaluation of this integral is therefore necessary to minimize computation time.

Fortunately, by virtue of the translation and rotation operation, we only need to integrate over the y'', z''-plane at $x'' = 0$. Furthermore, the Gaussian filter $G(\mathbf{x} - \mathbf{x}'')$ drops to zero rapidly when $\|\mathbf{x} - \mathbf{x}''\| \gg \epsilon$. Instead of integrating over the whole y'', z''-plane, the integration domain can thus be restricted to a small area around $\mathbf{x}$. The results of evaluation of the integrals on several different domains of increasing size showed that it is sufficient to take the integration domain as:

$$\begin{aligned} y'' &\in [y - 3\epsilon_2, y + 3\epsilon_2] \\ z'' &\in [z - 3\epsilon_3, z + 3\epsilon_3]. \end{aligned} \tag{B.5}$$

Still, we like to make the calculation of the integrals we do need to evaluate as efficient as possible. Relatively primitive numerical integration rules like the trapezoidal rule are simple to implement and converge as least as fast as N^{-2} (where N is the number of intervals) for functions with a continuous second derivative (Davis and Rabinowitz, 2007). A somewhat more sophisticated approach is application of Simpson's rule which is very frequently used in obtaining approximate integrals. Simpson's rule converges with rapidity N^{-4} at the worst for functions with a continuous fourth derivative. Taking the above in consideration, along with the fact that Simpson's rule is still fairly straightforward to implement, we choose to use Simpson's rule for numerical integration.

The Simpson's rule can be extended to two dimensions to give an approximation of the definite integral of some two-dimensional function $f(x, y)$,

$$I = \int_{a_y}^{b_y} \int_{a_x}^{b_x} f(x, y) \mathrm{d}x \mathrm{d}y, \tag{B.6}$$

on an integration domain $x \in [a_x, b_x]$ and $y \in [a_y, b_y]$. Now, consider an x, y-grid of $N \times N$ values, with N an odd integer, where the spacing h is determined by N and the integration bounds:

$$h_x = \frac{b_x - a_x}{N - 1} \tag{B.7}$$

$$h_y = \frac{b_y - a_y}{N - 1}. \tag{B.8}$$

Furthermore, we define a $N \times N$ matrix F_{ij} which contains the values of $f(x, y)$ at every grid point. The Simpson coefficient matrix S_{ij}, also of size $N \times N$, has the following values

$$\begin{aligned} S_{ij} &= (2, 8, 4, 8, \ldots, 8, 4, 8, 2)\,, \text{ for } i \text{ odd}, i \neq 1, N \\ S_{ij} &= (1, 4, 2, 4, \ldots, 4, 2, 4, 1)\,, \text{ for } i = 1, N \\ S_{ij} &= (4, 16, 4, \ldots, 4, 16, 4)\,, \text{ for } i \text{ even}. \end{aligned}$$

Then, I can be approximated by

$$I \approx \left(\frac{h_x h_y}{9}\right) \sum_{i=1}^{N} \sum_{j=1}^{N} S_{ij} F_{ij}. \tag{B.9}$$

The number of intervals, N, was set to 20. For this value the integral approximation was sufficiently accurate.

B.3. Averaging of wind velocity

The non-uniform actuator disk model essentially considers the azimuthally averaged effect of the rotating blades on the flow. Moreover, due to its inertia, a real rotor is only to a

limited degree sensitive to short time-scale force fluctuations. Future implementation of an actuator line model and more realistic control and (mechanical) response of the wind turbine can improve on this (section 6.2). For now, we will include a time averaging of the local wind velocity components to account for these effects.

Time averaging is performed by application of a one-sided exponential time filter. This method can be implement numerically in a straightforward way:

$$\langle u_i^* \rangle_t = a u_{i\,t}^* + (1-a)\langle u_i^* \rangle_{t-1}, \tag{B.10}$$

where $u_{i\,t}^*$ is the LES velocity at time step t. Further, $\langle u_i^* \rangle_t$ is the value of the time-averaged wind velocity at the current time step t, and the subscript $t-1$ indicates its value at the previous time step. The weighting factor, a, is defined as

$$a = 1 - e^{-\Delta t/T}, \tag{B.11}$$

with T an appropriate smoothing time scale.

A typical rotational speed of a wind turbine is around 10 to 20 RPM, which implies a rotation time scale of 3 to 6 s. Therefore, we set the smoothing time scale at 5 s.

C

Wind angle controller

The accumulated power of a wind farm is a function of the wind direction due to wake effects. The wind direction is, in general, again a function of height and time. Of several wind farms the power deficit in the wind farm has been established from production data for certain wind directions (see e.g. Alblas, 2012, Barthelmie et al., 2013, 2010, Hansen et al., 2012, Méchali et al., 2006). For validation of the model against this kind of data, it is necessary to study the performance of a wind farm for a given hub height wind direction during a prolonged period of time. In DALES, the flow is driven by a geostrophic wind. Obtaining the desired hub height wind angle directly through the geostrophic wind velocity components can be rather difficult, if not impossible when a simulation does not reach a steady state. Sescu and Meneveau (2014) therefore proposed to use a wind angle controller which dynamically controls the wind direction at hub height. For example Abkar et al. (2015) and Allaerts and Meyers (2015) also used a wind controller of this type in their LES study of wind farms.

Sescu and Meneveau gradually adjust the geostrophic wind direction by adding an additional source term, in the form of a Coriolis force, to the momentum equation:

$$\left[\frac{\partial u_i^*}{\partial t}\right]^{\text{wind angle control}} = -\epsilon_{ijk}\omega_j^{\text{eff}} u_k^*. \tag{C.1}$$

The expression for the effective angular velocity, $\omega_i^{\text{eff}} = \left(0, 0, \omega_3^{\text{eff}}\right)$, differs in the formulations of Sescu and Meneveau and Allaerts and Meyers.

Sescu and Meneveau set the angular velocity to $\omega_3^{\text{eff}} = a\omega$, where ω is an arbitrary angular speed which is set with respect to the relevant physical rates of rotation. The parameter a controls when the wind angle controller is active. If the angle between the mean wind direction at hub height, $\overline{\phi}(z^{*\text{hub}})$, and the desired direction exceeds a certain threshold, a is set from zero to one until the desired wind direction is achieved. The mean wind direction is calculated from the horizontal (domain) average wind velocity: $\overline{\phi} = \arctan\left(\overline{v^*}/\overline{u^*}\right)$.

Allaerts and Meyers, however, consider the change in the mean wind direction at every time step:

$$\omega = \frac{\overline{\phi}^t(z^{*\text{hub}}) - \overline{\phi}^{t-1}(z^{*\text{hub}})}{\Delta t}, \tag{C.2}$$

where t indicates the current time step. In order to filter rapid turbulent fluctuations, a one-sided exponential time filter with time constant τ_1 is applied to ω. Finally, after adding a factor to prevent steady state errors, Allaerts and Meyers arrive at the following expression for ω^{eff}:

$$\omega_3^{\text{eff}} = \langle\omega\rangle + \tau_2\left(\overline{\phi}(z^{*\text{hub}}) - \phi_{\text{desired}}\right). \tag{C.3}$$

The parameters of the controller were set to $\tau_1 = 3.3\,\text{min}$ and $\tau_2 = 2\,\text{h}^{-1}$.

Our implementation of a wind controller as described above did not give satisfactory results in all cases. As an alternative to controlling the wind direction, we therefore choose to rotate

the wind farm to achieve proper alignment with the prevailing hub height wind direction. Creech et al. (2015) used a similar approach to achieve different wind directions relative to the wind farm. The coordinates of the hub of the wind turbines, $x_i^{*\mathrm{hub}}$, become a function of time and can be written as

$$x_i^{*\mathrm{hub},t} = Q_{ij}^t \left(x_j^{*\mathrm{hub},0} - x_j^{*\mathcal{O}} \right) + x_i^{*\mathcal{O}}, \tag{C.4}$$

where $x_i^{*\mathrm{hub},0}$ are the initial hub coordinates. The angle over which Q_{ij} rotates the hub coordinates is obtained by applying a one-sided exponential time filter to the horizontal average hub height wind angle, $\overline{\phi}(z^{*\mathrm{hub}})$. The time constant of the filter is chosen with respect to the time scale of the mean wind direction change. The center of rotation, $x_i^{*\mathcal{O}}$, is set by considering the layout of the wind farm and the domain. By default the wind farm is rotated around the center of the domain.

The necessary rotation during the simulation, and hence the required horizontal domain size, is kept to a minimum by prescribing a geostrophic wind based on the mean hub height wind direction in a reference simulation without wind turbines.

D

DALESwindfarm user guide

D.1. Input data

The input required to run DALES with the wind turbine extension consists of a range of settings in the default `namoptions` input file and four additional input files.

The settings in `namoptions` are divided into three separate namelists: `windturbine`, `nudgeboundary` and `windcontroller`. All settings and their default values are given in tables D.1, D.2 and D.3.

The first additional file, `windfarmdata.inp.expnr`, with `expnr` the experiment number, contains the coordinates of the hub of the wind turbine(s), the rotor radius, characteristics of the nacelle and tower and the cut-in/cut-out wind speed. This file consists of a single unimportant header line, followed by the parameters of each wind turbine on a single line with columns in the order as given in table D.4.

The other three files contain the detailed wind turbine characteristics. The input parameters are distributed over three different files, according to their independent variable, see table D.5. Examples of these three input files for the Vestas V80 2 MW wind turbine are given in appendix E.

D.2. Output and monitoring

The wind turbine-related output is written to several different files. Further, every wind turbine writes to a separate file according to their ID number (`turid`). The `windturbinemonitor.turid.expnr` is a general file for monitoring the wind turbines, the other files give time

Table D.1: Settings related to the wind turbine extension that are contained in the `windturbine` namelist of the `namoptions` file.

Parameter	Description	Units	Default setting
`lwindturbine`	Enable wind turbine	[-]	`.false.`
`ldiagn`	Write diagnostics, primarily for debugging	[-]	`.false.`
`ltiploss`	Enable tip loss correction	[-]	`.false.`
`ntur`	Number of turbines	[-]	1
`Tyaw`	Yaw time scale	[s]	60
`Tsettur`	Enable wind turbine after spin-up	[s]	0
`TVdavg`	Time constant of wind velocity smoothing, equation (B.11)	[s]	5
`Tchktur`	Write to `windturbinemonitor`	[s]	60
`Tturdata`	Write to `windturbinedata`	[s]	60
`smthcoefax`	Axial smoothing factor, equation (B.3)	[-]	1.5
`smthcoefrad`	Radial smoothing factor, equation (B.3)	[-]	1.5

Table D.2: Settings related to the wind turbine extension that are contained in the `nudgeboundary` namelist of the `namoptions` file.

Parameter	Description	Units	Default setting
`lnudgeboundary`	Enable prescribed boundaries	[-]	`.false.`
`lstatref`	Write statistics of reference simulation	[-]	`.false.`
`nudgedepthgr`	Number of grid points in boundary	[-]	10

Table D.3: Settings related to the wind turbine extension that are contained in the `windcontroller` namelist of the `namoptions` file.

Parameter	Description	Units	Default setting
`lwindcontrol1`	Enable wind controller as in Sescu and Meneveau (2014)	[-]	`.false.`
`lwindcontrol2`	Enable wind controller as in Allaerts and Meyers (2015)	[-]	`.false.`
`lwindcontrol3`	Enable alignment of wind farm to mean wind direction	[-]	`.false.`
`omega_control`	Angular speed of wind controller	[rad/s]	1×10^{-6}
`phi_desired`	Desired wind angle	[deg]	0
`phi_threshold`	Threshold angle of wind controller	[deg]	0.2
`Tsetcontrol`	Enable wind controller after spin-up	[s]	0

Table D.4: Input parameters contained in the `windfarmdata.inp.expnr` input file.

Parameter	Units
ID	[-]
$x^{*\mathrm{hub}}$	[m]
$y^{*\mathrm{hub}}$	[m]
$z^{*\mathrm{hub}}$	[m]
R	[m]
Nacelle radius	[m]
Tower radius (top)	[m]
Tower radius (base)	[m]
C_D^{nac}	[-]
C_D^{tower}	[-]
Cut-in wind speed	[m/s]
Cut-out wind speed	[m/s]

Table D.5: Overview of the wind turbine parameters that are required as input to the model.

Parameter	Units	As function of	Units	File
Ω	[RPM]	U_∞	[m/s]	`pitchrotdata.inp.expnr`
$\beta_{p,0}$	[deg]	U_∞	[m/s]	
c	[m]	r	[m]	`chordtwistdata.inp.expnr`
β_T	[deg]	r	[m]	
C_L	[-]	α	[deg]	`liftdragdata.inp.expnr`
C_D	[-]	α	[deg]	

series of important quantities like the extracted power and the yaw angle. An overview of the output files is given in table D.6.

The number of wind turbine-related output files will equal the number of processing units. To keep the code fully parallel, this is the case even when the number of wind turbines is lower than the available number of processing units.

Table D.6: Overview of the four output files that contain data related to the wind turbine calculation. Every wind turbine writes to a different file, according to the ID number provided in `windfarmdata.inp.expnr`.

Filename	Contents
`windturbinemonitor.turid.expnr`	Location of turbine, rotor-average wind velocity and wind turbine forces, extracted power. Additionally a message is written to this file when the yaw orientation changes.
`windturbinedata.turid.expnr`	Time from start of simulation, local free-stream wind speed, extracted power.
`winddir.turid.expnr`	Time from start of simulation, yaw angle of the wind turbine, wind control angle.
`windturbinediag.turid.expnr`	Detailed diagnostics of wind turbine force calculation at every time step (only if `ldiagn` is enabled).

D.3. Practical use and recommendations

In this section some considerations with regard to the use and performance of the wind turbine model in DALES will be discussed. In general, first a case is set up based on observations and simulations without wind turbines on a coarse grid. Once the initial profiles, large-scale tendencies and surface boundary conditions have been established, a high-resolution (10 to 20 m) spin-up simulation can be performed. This spin-up simulation can optionally be performed on a relatively small domain size. The developed fields can then, by virtue of their periodic boundary conditions, be stitched together to cover the wind farm-sized domain, given that the fields are randomized at startup. Only in this final wind farm simulation it is necessary to prescribe the boundaries. Performing a spin-up can thus save a considerable amount of computational resources.

In order to obtain correct results, it is essential to know the limitations of the model. As discussed before, the model is sensitive to the wind turbine characteristics that are provided as input. The characteristics are usually deduced in an indirect way or estimated and may only be valid for a certain wind speed (range). Comparisons with the power curve of the manufacturer should always be made to ensure DALES responds correctly to the input data.

Using the optional wind angle controller might also lead to unexpected and faulty results in some cases. Test runs should always be performed with and without controlling the wind angle to study its effect on the vertical profiles of wind speed and turbulence. In all cases it is of course recommend to prescribe the geostrophic wind components such that the resulting hub height wind direction is close to the desired value.

Since the wind turbines have a fixed location in space, the Galilean transformation in DALES should be disabled (i.e. setting `cu` and `cv` to zero in the `namoptions` file).

Finally, it is not recommend to use the 2$^{\text{nd}}$ order advection scheme. Severe numerical errors, in the form of 2dx-waves, were observed in the vicinity of the wind turbine in this case.

E

Wind turbine characteristics

E.1. Vestas V80

Table E.1: Blade pitch angle and rotational speed of the rotor as a function of wind speed, contained in the `pitchrotdata.inp.expnr` input file.

U_∞ [m/s]	$\beta_{p,0}$ [deg]	Ω [RPM]
5	1.179	12.500
6	0.109	13.240
7	-0.636	14.580
8	-1.000	16.225
9	-1.316	17.400
10	-1.388	18.000
11	-0.161	18.000
12	2.776	18.000
13	6.214	18.000
14	9.325	18.000
15	11.639	18.000
16	13.678	18.000
17	15.612	18.000
18	17.450	18.000
19	18.859	18.000
20	19.159	18.000

Table E.2: Tabulated values of the lift and drag coefficients as a function of the angle of attack, contained in the `liftdragdata.inp.expnr` input file.

α [deg]	C_L [-]	C_D [-]
-5	-0.170	0.017
-4	-0.099	0.017
-3	0.010	0.016
-2	0.123	0.016
-1	0.232	0.016
0	0.336	0.017
1	0.440	0.017
2	0.546	0.017
3	0.655	0.016
4	0.768	0.016
5	0.864	0.017
6	0.956	0.018
7	1.034	0.019
8	1.112	0.021
9	1.176	0.023
10	1.237	0.026
11	1.275	0.029
12	1.299	0.033
13	1.315	0.038
14	1.309	0.044
15	1.295	0.051
16	1.264	0.075
17	1.224	0.124
18	1.176	0.149
19	1.117	0.171
20	1.068	0.190

Table E.3: The chord length and twist angle are a function of the radius and contained in the `chordtwistdata.inp.expnr` input file.

r [m]	c [m]	β_T [deg]
0	2.406	18.793
1	2.406	18.793
2	2.406	18.793
3	2.406	18.793
4	2.873	17.572
5	3.235	16.391
6	3.415	15.267
7	3.526	14.203
8	3.614	13.141
9	3.595	12.048
10	3.531	10.979
11	3.462	10.085
12	3.363	9.222
13	3.255	8.437
14	3.126	7.663
15	2.995	6.972
16	2.859	6.281
17	2.721	5.638
18	2.562	4.996
19	2.423	4.429
20	2.310	3.922
21	2.194	3.426
22	2.075	2.960
23	1.956	2.493
24	1.851	2.171
25	1.750	1.883
26	1.662	1.602
27	1.584	1.341
28	1.506	1.079
29	1.444	0.852
30	1.385	0.666
31	1.325	0.481
32	1.262	0.328
33	1.198	0.276
34	1.121	0.224
35	1.011	0.158
36	0.900	0.085
37	0.762	0.012
38	0.597	0.002
39	0.317	0.002
40	0.028	0.001

Bibliography

Abkar, M., and F. Porté-Agel, 2015: Influence of atmospheric stability on wind-turbine wakes: A large-eddy simulation study. *Phys. Fluids*, **27 (3)**, 035 104.

Abkar, M., A. Sharifi, and F. Porté-Agel, 2015: Large-eddy simulation of the diurnal variation of wake flows in a finite-size wind farm. *Journal of Physics: Conference Series*, IOP Publishing, Vol. 625, 012031.

Ackerman, A. S., M. P. Kirkpatrick, D. E. Stevens, and O. B. Toon, 2004: The impact of humidity above stratiform clouds on indirect aerosol climate forcing. *Nature*, **432 (7020)**, 1014–1017.

Ainslie, J. F., 1988: Calculating the flowfield in the wake of wind turbines. *J. Wind Eng. Ind. Aerodyn.*, **27 (1)**, 213–224.

Aitken, M. L., R. M. Banta, Y. L. Pichugina, and J. K. Lundquist, 2014a: Quantifying wind turbine wake characteristics from scanning remote sensor data. *J. Atmos. Oceanic Technol.*, **31 (4)**, 765–787.

Aitken, M. L., B. Kosović, J. D. Mirocha, and J. K. Lundquist, 2014b: Large eddy simulation of wind turbine wake dynamics in the stable boundary layer using the weather research and forecasting model. *J. Renewable Sustainable Energy*, **6 (3)**, 033 137.

Alblas, L., 2012: Power output of offshore wind farms in relation to atmospheric stability. M.S. thesis, Delft University of Technology.

Allaerts, D., and J. Meyers, 2015: Large eddy simulation of a large wind-turbine array in a conventionally neutral atmospheric boundary layer. *Phys. Fluids*, **27 (6)**, 065 108.

Baidya Roy, S., S. Pacala, and R. Walko, 2004: Can large wind farms affect local meteorology? *J. Geophys. Res.*, **109 (D19)**.

Barthelmie, R. J., K. S. Hansen, and S. C. Pryor, 2013: Meteorological controls on wind turbine wakes. *Proc. of the IEEE*, **101 (4)**, 1010–1019.

Barthelmie, R. J., and Coauthors, 2010: Quantifying the impact of wind turbine wakes on power output at offshore wind farms. *J. Atmos. Oceanic Technol.*, **27 (8)**, 1302–1317.

Bastankhah, M., and F. Porté-Agel, 2014: A new analytical model for wind-turbine wakes. *Renew. Energy*, **70**, 116–123.

Beare, R. J., and Coauthors, 2006: An intercomparison of large-eddy simulations of the stable boundary layer. *Bound.-Layer Meteorol.*, **118 (2)**, 247–272.

Böing, S., 2014: The interaction between deep convective clouds and their environment. Ph.D. thesis, Delft University of Technology.

Burton, T., D. Sharpe, N. Jenkins, and E. Bossanyi, 2001: *Wind energy handbook*. John Wiley & Sons.

Calaf, M., C. Meneveau, and J. Meyers, 2010: Large eddy simulation study of fully developed wind-turbine array boundary layers. *Phys. Fluids*, **22 (1)**, 015 110.

Christiansen, M. B., and C. B. Hasager, 2005: Wake effects of large offshore wind farms identified from satellite sar. *Remote Sens. Environ.*, **98 (2)**, 251–268.

Christiansen, M. B., and C. B. Hasager, 2006: Using airborne and satellite sar for wake mapping offshore. *Wind Energy*, **9 (5)**, 437–455.

Churchfield, M. J., S. Lee, J. Michalakes, and P. J. Moriarty, 2012a: A numerical study of the effects of atmospheric and wake turbulence on wind turbine dynamics. *J. Turbul.*, **(13)**.

Churchfield, M. J., S. Lee, P. J. Moriarty, L. A. Martinez, S. Leonardi, G. Vijayakumar, and J. G. Brasseur, 2012b: A large-eddy simulation of wind-plant aerodynamics. *AIAA paper*, **537**.

Costa, A., A. Crespo, J. Navarro, G. Lizcano, H. Madsen, and E. Feitosa, 2008: A review on the young history of the wind power short-term prediction. *Renewable Sustainable Energy Rev.*, **12 (6)**, 1725–1744.

Creech, A., W.-G. Früh, and A. E. Maguire, 2015: Simulations of an offshore wind farm using large-eddy simulation and a torque-controlled actuator disc model. *Surv. Geophys.*, **36 (3)**, 427–481.

Crespo, A., J. Hernandez, and S. Frandsen, 1999: Survey of modelling methods for wind turbine wakes and wind farms. *Wind Energy*, **2 (1)**, 1–24.

Davis, P. J., and P. Rabinowitz, 2007: *Methods of numerical integration*. Courier Corporation.

de Roode, S. R., P. G. Duynkerke, and H. J. Jonker, 2004: Large-eddy simulation: How large is large enough? *J. Atmos. Sci.*, **61 (4)**, 403–421.

de Roode, S. R., and A. Los, 2008: The effect of temperature and humidity fluctuations on the liquid water path of non-precipitating closed-cell stratocumulus clouds. *Quart. J. Roy. Meteor. Soc.*, **134 (631)**, 403–416.

de Roode, S. R., and Coauthors, 2016: Large eddy simulations of euclipse/gass lagrangian stratocumulus to cumulus transitions: Mean state, turbulence, and decoupling. *J. Atmos. Sci.*, **(2016)**.

Devis, A., N. P. Lipzig, and M. Demuzere, 2013: A new statistical approach to downscale wind speed distributions at a site in northern europe. *J. Geophys. Res.*, **118 (5)**, 2272–2283.

Driedonks, A., and P. Duynkerke, 1989: Current problems in the stratocumulus-topped atmospheric boundary layer. *Bound.-Layer Meteorol.*, **46 (3)**, 275–303.

Dunn, B., H. Kamath, and J.-M. Tarascon, 2011: Electrical energy storage for the grid: a battery of choices. *Science*, **334 (6058)**, 928–935.

Duynkerke, P., and Coauthors, 1999: Intercomparison of three- and one-dimensional model simulations and aircraft observations of stratocumulus. *Bound.-Layer Meteorol.*, **92 (3)**, 453–487.

Duynkerke, P. G., and Coauthors, 2004: Observations and numerical simulations of the diurnal cycle of the eurocs stratocumulus case. *Quart. J. Roy. Meteor. Soc.*, **130 (604)**, 3269–3296.

Ellis, N., R. Davy, and A. Troccoli, 2015: Predicting wind power variability events using different statistical methods driven by regional atmospheric model output. *Wind Energy*, **18 (9)**, 1611–1628.

Emeis, S., 2010: Meteorological explanation of wake clouds at horns rev wind farm. *Dewi Magazin*, **(37)**, 52–55.

Energinet.dk, 2014: Annual report 2014: Ready energy - now and into the future.

Fairall, C., A. Grachev, A. Bedard, and R. Nishiyama, 1996: Wind, wave, stress, and surface roughness relationships from turbulence measurements made on r/p flip in the scope experiment. Tech. rep., NOAA Tech. Memo. ERL ETL-268.

Fitch, A. C., J. K. Lundquist, and J. B. Olson, 2013: Mesoscale influences of wind farms throughout a diurnal cycle. *Mon. Weather Rev.*, **141 (7)**, 2173–2198.

Garratt, J. R., 1994: Review: the atmospheric boundary layer. *Earth Sci. Rev.*, **37 (1-2)**, 89–134.

Giebel, G., R. Brownsword, G. Kariniotakis, M. Denhard, and C. Draxl, 2011: The state-of-the-art in short-term prediction of wind power: A literature overview. Tech. rep., ANEMOS.

Gill, S., B. Stephen, and S. Galloway, 2012: Wind turbine condition assessment through power curve copula modeling. *IEEE Trans Sustainable Energy*, **3 (1)**, 94–101.

Goit, J., and J. Meyers, 2014: Optimal control of wind farm power extraction in large eddy simulations. *AIAA SciTech 32nd ASME Wind Energy Symposium, American Institute of Aeronautics and Astronautics, National Harbour, USA*, 1–11.

González-Longatt, F., P. Wall, and V. Terzija, 2012: Wake effect in wind farm performance: Steady-state and dynamic behavior. *Renew. Energy*, **39 (1)**, 329–338.

Hansen, K. S., R. J. Barthelmie, L. E. Jensen, and A. Sommer, 2012: The impact of turbulence intensity and atmospheric stability on power deficits due to wind turbine wakes at horns rev wind farm. *Wind Energy*, **15 (1)**, 183–196.

Hasager, C. B., L. Rasmussen, A. Peña, L. E. Jensen, and P.-E. Réthoré, 2013: Wind farm wake: The horns rev photo case. *Energies*, **6 (2)**, 696–716.

Heuff, F., 2016: Stratocumulus predictions with a large-eddy simulation model. M.S. thesis, Delft University of Technology.

Heus, T., and Coauthors, 2010: Formulation of the dutch atmospheric large-eddy simulation (dales) and overview of its applications. *Geosci. Model Dev.*, **3 (2)**, 415–444.

Iungo, G. V., and F. Porté-Agel, 2014: Volumetric lidar scanning of wind turbine wakes under convective and neutral atmospheric stability regimes. *J. Atmos. Oceanic Technol.*, **31 (10)**, 2035–2048.

Ivanell, S. A., 2009: Numerical computations of wind turbine wakes. Ph.D. thesis, Gotland University.

Jimenez, A., A. Crespo, E. Migoya, and J. Garcia, 2007: Advances in large-eddy simulation of a wind turbine wake. *Journal of Physics: Conference Series*, IOP Publishing, Vol. 75, 012041.

Jimenez, A., A. Crespo, E. Migoya, and J. Garcia, 2008: Large-eddy simulation of spectral coherence in a wind turbine wake. *Environ. Res. Lett.*, **3 (1)**, 015 004.

Jonkman, J. M., S. Butterfield, W. Musial, and G. Scott, 2009: Definition of a 5-mw reference wind turbine for offshore system development. Tech. rep., National Renewable Energy Laboratory Golden, CO.

Käsler, Y., S. Rahm, R. Simmet, and M. Kühn, 2010: Wake measurements of a multi-mw wind turbine with coherent long-range pulsed doppler wind lidar. *J. Atmos. Oceanic Technol.*, **27 (9)**, 1529–1532.

Keith, D. W., J. F. DeCarolis, D. C. Denkenberger, D. H. Lenschow, S. L. Malyshev, S. Pacala, and P. J. Rasch, 2004: The influence of large-scale wind power on global climate. *Proc. Natl. Acad. Sci. U.S.A.*, **101 (46)**, 16 115–16 120.

Kempton, W., and J. Tomić, 2005: Vehicle-to-grid power implementation: From stabilizing the grid to supporting large-scale renewable energy. *J. Power Sources*, **144 (1)**, 280–294.

Larsen, G. C., H. A. Madsen, K. Thomsen, and T. J. Larsen, 2008: Wake meandering: a pragmatic approach. *Wind Energy*, **11 (4)**, 377–395.

Laursen, J., P. Enevoldsen, and S. Hjort, 2007: 3d cfd rotor computations of a multi-megawatt hawt rotor. *Proceedings of the European Wind Energy Conference, Milan, Italy*, Vol. 610.

Leloudas, G., 2006: Optimization of wind turbines with respect to noise. M.S. thesis, Technical University of Denmark.

Li, X., and S. Lehner, 2013: Observation of terrasar-x for studies on offshore wind turbine wake in near and far fields. *IEEE J-STARS*, **6 (3)**, 1757–1768.

Lu, H., and F. Porté-Agel, 2011: Large-eddy simulation of a very large wind farm in a stable atmospheric boundary layer. *Phys. Fluids*, **23 (6)**, 065 101.

Lu, H., and F. Porté-Agel, 2015: On the impact of wind farms on a convective atmospheric boundary layer. *Bound.-Layer Meteorol.*, **157 (1)**, 81–96.

Machefaux, E., G. C. Larsen, T. Koblitz, N. Troldborg, M. C. Kelly, A. Chougule, K. S. Hansen, and J. S. Rodrigo, 2015: An experimental and numerical study of the atmospheric stability impact on wind turbine wakes. *Wind Energy*.

Madsen, H. A., N. N. SOrensen, and S. Schreck, 2003: Yaw aerodynamics analyzed with three codes in comparison with experiment. *ASME 2003 Wind Energy Symposium*, American Society of Mechanical Engineers, 94–103.

Magnusson, M., 1999: Near-wake behaviour of wind turbines. *J. Wind Eng. Ind. Aerodyn.*, **80 (1)**, 147–167.

Manwell, J. F., J. G. McGowan, and A. L. Rogers, 2010: *Wind energy explained: theory, design and application*. John Wiley & Sons.

Méchali, M., R. Barthelmie, S. Frandsen, L. Jensen, and P.-E. Réthoré, 2006: Wake effects at horns rev and their influence on energy production. *Proceedings of the European Wind Energy Conference and Exhibition*.

Mehta, D., A. Van Zuijlen, B. Koren, J. Holierhoek, and H. Bijl, 2014: Large eddy simulation of wind farm aerodynamics: A review. *J. Wind Eng. Ind. Aerodyn.*, **133**, 1–17.

Meyers, J., 2016: personal communication.

Meyers, J., and C. Meneveau, 2010: Large eddy simulations of large wind-turbine arrays in the atmospheric boundary layer. *AIAA Paper*, **827**, 2010.

Meyers, J., and C. Meneveau, 2012: Optimal turbine spacing in fully developed wind farm boundary layers. *Wind Energy*, **15 (2)**, 305–317.

Mikkelsen, R., 2003: Actuator disc methods applied to wind turbines. Ph.D. thesis, Technical University of Denmark.

Mikkelsen, T., and Coauthors, 2013: A spinner-integrated wind lidar for enhanced wind turbine control. *Wind Energy*, **16 (4)**, 625–643.

Mirocha, J., B. Kosovic, M. Aitken, and J. Lundquist, 2014: Implementation of a generalized actuator disk wind turbine model into the weather research and forecasting model for large-eddy simulation applications. *J. Renewable Sustainable Energy*, **6 (1)**, 013 104.

Mirocha, J. D., D. A. Rajewski, N. Marjanovic, J. K. Lundquist, B. Kosović, C. Draxl, and M. J. Churchfield, 2015: Investigating wind turbine impacts on near-wake flow using profiling lidar data and large-eddy simulations with an actuator disk model. *J. Renewable Sustainable Energy*, **7 (4)**, 043 143.

Moeng, C., and P. Sullivan, 2002: Large eddy simulation. *Encyclopedia of Atmospheric Sciences*, 1140–1150.

Munters, W., C. Meneveau, and J. Meyers, 2015: Turbulent inflow precursor method with time-varying direction for large-eddy simulations and applications to wind farms. *Bound.-Layer Meteorol.*, 1–24.

Murray, F. W., 1967: On the computation of saturation vapor pressure. *J. Appl. Meteorol.*, **6 (1)**, 203–204.

Nilsson, K., S. Ivanell, K. S. Hansen, R. Mikkelsen, J. N. Sørensen, S.-P. Breton, and D. Henningson, 2015: Large-eddy simulations of the lillgrund wind farm. *Wind Energy*, **18 (3)**, 449–467.

Popinet, S., 2003: Gerris: a tree-based adaptive solver for the incompressible euler equations in complex geometries. *J. Comput. Phys.*, **190 (2)**, 572–600.

Porté-Agel, F., H. Lu, and Y.-T. Wu, 2014: Interaction between large wind farms and the atmospheric boundary layer. *Procedia IUTAM*, **10**, 307–318.

Porté-Agel, F., Y.-T. Wu, H. Lu, and R. J. Conzemius, 2011: Large-eddy simulation of atmospheric boundary layer flow through wind turbines and wind farms. *J. Wind Eng. Ind. Aerodyn.*, **99 (4)**, 154–168.

Pourquie, M., W. Breugem, and B. J. Boersma, 2009: Some issues related to the use of immersed boundary methods to represent square obstacles. *Int. J. Multiscale Comput. Eng.*, **7 (6)**.

Roshko, A., 1961: Experiments on the flow past a circular cylinder at very high reynolds number. *J. Fluid Mech.*, **10 (03)**, 345–356.

Sanderse, B., 2009: Aerodynamics of wind turbine wakes. Tech. Rep. E-09-016, ECN.

Sanderse, B., v. d. S. Pijl, and B. Koren, 2011: Review of computational fluid dynamics for wind turbine wake aerodynamics. *Wind Energy*, **14 (7)**, 799–819.

Sathe, A., J. Mann, T. Barlas, W. Bierbooms, and G. Bussel, 2013: Influence of atmospheric stability on wind turbine loads. *Wind Energy*, **16 (7)**, 1013–1032.

Schalkwijk, J., E. J. Griffith, F. H. Post, and H. J. Jonker, 2012: High-performance simulations of turbulent clouds on a desktop pc: Exploiting the gpu. *Bull. Am. Meteorol. Soc.*

Schalkwijk, J., H. J. Jonker, A. P. Siebesma, and F. C. Bosveld, 2015: A year-long large-eddy simulation of the weather over cabauw: An overview. *Mon. Weather Rev.*, **143 (3)**, 828–844.

Schalkwijk, J., H. J. Jonker, A. P. Siebesma, and E. van Meijgaard, 2014: Weather forecasting using gpu-based large-eddy simulations. *Bull. Amer. Meteor. Soc.*

Sescu, A., and C. Meneveau, 2014: A control algorithm for statistically stationary large-eddy simulations of thermally stratified boundary layers. *Quart. J. Roy. Meteor. Soc.*, **140 (683)**, 2017–2022.

Siebesma, A. P., and Coauthors, 2003: A large eddy simulation intercomparison study of shallow cumulus convection. *J. Atmos. Sci.*, **60 (10)**, 1201–1219.

Sisterson, D. L., and P. Frenzen, 1978: Nocturnal boundary-layer wind maxima and the problem of wind power assessment. *Environ. Sci. Technol.*, **12 (2)**, 218–221.

Sørensen, J. N., and W. Z. Shen, 2002: Numerical modeling of wind turbine wakes. *J. Fluids Eng.*, **124 (2)**, 393–399.

Stevens, B., and Coauthors, 2005: Evaluation of large-eddy simulations via observations of nocturnal marine stratocumulus. *Mon. Weather Rev.*, **133 (6)**, 1443–1462.

Stevens, R., 2012: *Ned. Tijdschr. Natuurkd.*, **(9)**, 356.

Stevens, R. J., J. Graham, and C. Meneveau, 2014: A concurrent precursor inflow method for large eddy simulations and applications to finite length wind farms. *Renew. Energy*, **68**, 46–50.

Storm, B., J. Dudhia, S. Basu, A. Swift, and I. Giammanco, 2009: Evaluation of the weather research and forecasting model on forecasting low-level jets: Implications for wind energy. *Wind Energy*, **12 (1)**, 81–90.

Stull, R. B., 1988: *An introduction to boundary layer meteorology*, Vol. 13. Springer Science & Business Media.

Sullivan, P. P., C.-H. Moeng, B. Stevens, D. H. Lenschow, and S. D. Mayor, 1998: Structure of the entrainment zone capping the convective atmospheric boundary layer. *J. Atmos. Sci.*, **55 (19)**, 3042–3064.

Uchida, T., and Y. Ohya, 2003: Large-eddy simulation of turbulent airflow over complex terrain. *J. Wind Eng. Ind. Aerodyn.*, **91 (1)**, 219–229.

Van der Dussen, J., S. De Roode, and A. Siebesma, 2014: Factors controlling rapid stratocumulus cloud thinning. *J. Atmos. Sci.*, **71 (2)**, 655–664.

Van Heerde, S., 2015: Investigating the performance of wind farms with alternating tower heights. M.S. thesis, Delft University of Technology.

van Hooft, J., S. Popinet, S. van der Linden, C. van Heerwaarden, and B. J. van de Wiel, in preparation: An adaptive grid method for atmospheric boundary layer flows.

van Lipzig, N. P. M., 1999: The surface mass balance of the antarctic ice sheet: a study with a regional atmospheric model. Ph.D. thesis, University of Utrecht.

Van Zanten, M. C., and Coauthors, 2011: Controls on precipitation and cloudiness in simulations of trade-wind cumulus as observed during rico. *J. Adv. Model. Earth Syst.*, **3 (2)**.

Vermeer, L., J. N. Sørensen, and A. Crespo, 2003: Wind turbine wake aerodynamics. *Prog. Aerosp. Sci.*, **39 (6)**, 467–510.

Wagenaar, J., L. Machielse, and J. Schepers, 2012: Controlling wind in ecn's scaled wind farm. *Proc. Europe Premier Wind Energy Event*, 685–694.

Wagner, R., I. Antoniou, S. M. Pedersen, M. S. Courtney, and H. E. Jørgensen, 2009: The influence of the wind speed profile on wind turbine performance measurements. *Wind Energy*, **12 (4)**, 348–362.

Wienke, S., P. Springer, C. Terboven, and D. an Mey, 2012: Openacc-first experiences with real-world applications. *Euro-Par 2012 Parallel Processing*, Springer, 859–870.

Wood, R., 2012: Stratocumulus clouds. *Mon. Weather Rev.*, **140 (8)**, 2373–2423.

Wu, Y.-T., and F. Porté-Agel, 2011: Large-eddy simulation of wind-turbine wakes: evaluation of turbine parametrisations. *Bound.-Layer Meteorol.*, **138 (3)**, 345–366.

Wu, Y.-T., and F. Porté-Agel, 2012: Atmospheric turbulence effects on wind-turbine wakes: An les study. *Energies*, **5 (12)**, 5340–5362.

Wu, Y.-T., and F. Porté-Agel, 2013: Simulation of turbulent flow inside and above wind farms: Model validation and layout effects. *Bound.-Layer Meteorol.*, **146 (2)**, 181–205.

Wu, Y.-T., and F. Porté-Agel, 2015: Modeling turbine wakes and power losses within a wind farm using les: An application to the horns rev offshore wind farm. *Renew. Energy*, **75**, 945–955.

Xie, L., Y. Gu, X. Zhu, and M. G. Genton, 2014: Short-term spatio-temporal wind power forecast in robust look-ahead power system dispatch. *IEEE Transactions on Smart Grid*, **5 (1)**, 511–520.

Zhu, X., and M. G. Genton, 2012: Short-term wind speed forecasting for power system operations. *Int. Stat. Rev.*, **80 (1)**, 2–23.